Characterization of Cavitation Instabilities in Rocket Engine Turbopump Inducers

by

Vincent Wang

B.S., Johns Hopkins University (2014)

Submitted to the Department of Aeronautics and Astronautics
in partial fulfillment of the requirements for the degree of

Master of Science in Aeronautics and Astronautics

at the

MASSACHUSETTS INSTITUTE OF TECHNOLOGY

September 2016

© Massachusetts Institute of Technology 2016. All rights reserved.

Author .....
Department of Aeronautics and Astronautics
August 18, 2016

Certified by .....
Zoltán S. Spakovszky
Professor of Aeronautics and Astronautics
Thesis Supervisor

Accepted by .....
Paulo C. Lozano
Associate Professor of Aeronautics and Astronautics
Chair, Graduate Program Committee

Characterization of Cavitation Instabilities in Rocket Engine Turbopump Inducers

by

Vincent Wang

Submitted to the Department of Aeronautics and Astronautics
on August 18, 2016, in partial fulfillment of the requirements for the degree of
Master of Science in Aeronautics and Astronautics

Abstract

Characterized by super-synchronous rotation of cavities around the periphery of rocket engine turbopump inducers, rotating cavitation is the primary cavitation instability considered in this thesis. A recently developed hypothesis for rotating cavitation onset is assessed through novel experimental analysis and a previously developed body force modeling approach using the MIT inducer, representative of the design of the Space Shuttle main engine low-pressure oxidizer pump inducer.

A previously developed temporal and spatial Fourier decomposition, known as Traveling Wave Energy (TWE) analysis, of experimental unsteady inlet pressure measurements of the cavitating MIT inducer is demonstrated. TWE analysis offers several advantages over the current experimental analysis methods, resolving frequency, spatial mode shapes, and rotation direction of cavitation phenomena. Cut-on/cut-off behavior between rotating cavitation and alternate blade cavitation is observed, supporting the hypothesis that alternate blade cavitation is a necessary precursor to rotating cavitation onset.

TWE is adapted for use on high speed borescope video data taken in the same experimental campaign. The frequency content extracted is qualitatively correlated with the results from the pressure data, establishing TWE as a viable tool for quantitative analysis of optical data. The video TWE results indicate that cavitation instability signatures are uniform in the radial direction, suggesting that a pressure transducer array can be established as the primary detection method for rotating cavitation and thereby simplifying test setups.

A body force based modeling approach typically used for aero-engine compressor stability prediction is assessed for use in predicting rotating cavitation. A previously developed inducer-specific body force model formulation is validated in a representative compressor geometry, capturing global performance across the characteristic within 7%. However, the model exhibits convergence issues when applied to the inducer, hypothesized to be due to sensitivity in the inducer's loss characteristics. The investigation suggests the low flow coefficient design of the inducer drives the loss sensitivity and is the root cause behind the model's convergence issues. The results indicate the body force model is valid for the higher flow coefficient designs and lower stagger angles typically found in aero-engine compressors and fans. Suggestions for desensitizing the model for the inducer as well as further diagnostics defining the limiting geometry case for body force modeling are made.

Thesis Supervisor: Zoltán S. Spakovszky
Title: Professor of Aeronautics and Astronautics

Acknowledgments

First and foremost, I would like to thank my advisor, Professor Zoltán Spakovszky. His guidance, knowledge, and passion will stay with me throughout my professional career and I am extremely grateful for his mentorship throughout my time at MIT. I will also always remember our trips out to Aerospace Corporation. For the record, Professor, I still 100% believe if things went south in that parking lot, we could have taken him.

This research was funded by NASA Marshall Space Flight Center. I would like to express my gratitude to Andy Mulder for his technical guidance. This project was also supported by the Aerospace Corporation. I am tremendously grateful to David Jackson, Jay Schwille, and Juliett Davitian for their diligence and expertise throughout our experimental campaign.

I would like to thank Dr. Claudio Lettieri for his support throughout the project. His knowledge was indispensable and his enthusiasm made him a joy to work with. Thank you also to Professor Chris Brennen for his invaluable advice and experience with inducers and two-phase flows.

To my labmates, Derek, Andrew, Georgi, Andras, and Jinwook, our technical conversations and (very) occasional off-topic ventures kept my time at the Gas Turbine Lab lively. May you all continue to spit hot fire. Special thanks to Andras for teaching me about the ins and outs of Linux and networking, and both Andras and Jinwook for taking over network administrator responsibilities while I had fun writing this thesis. Yvana, you have the distinction of being the only non-GTL MIT friend I'm acknowledging – I hope you're happy.

I could not have succeeded in my education without my friends outside of MIT. Allan, Liz C., Liz H., Ally, Jarick, and Barry, you guys were amazing running partners and even better friends. Lilian and Danny, your endless companionship and support through the ups and downs of my time here means more to me than you'll ever k-now. Back home, Daniel, John, Alexis, Chris, and Katie, you've always been there for me and I could not have done this without you guys.

Finally, thank you to my parents and my sister, Kim. Your encouragement of my curiosity and questions since day one made this all possible. I could not have made it to where I am now without your love and support.

Contents

1 Introduction **23**

1.1 Background and Motivation 23

1.1.1 Cavitation Instabilities in Inducers 24

1.1.2 Recent Findings on the Mechanism of Rotating Cavitation Onset 26

1.2 Problem Statement and Previous Work 30

1.2.1 Experimental Characterization of Cavitation Instabilities . . . 31

1.2.2 Modeling of Cavitation Instabilities 32

1.3 Research Goals and Objectives 34

1.4 Thesis Contributions 34

1.5 Organization of Thesis 36

2 Experimental Assessment of MIT Inducer Performance and Cavitation Behavior **37**

2.1 Experimental Setup 38

2.2 MIT Inducer Geometry 41

2.3 MIT Inducer Steady Performance 42

2.3.1 Wetted Performance 43

2.3.2 Steady Cavitating Performance 43

2.4 Dynamic Behavior of Four Bladed Inducers 45

2.5 Traveling Wave Energy Analysis 47

2.6 Traveling Wave Energy Analysis of Unsteady Pressure Data 50

2.7 Traveling Wave Energy Analysis of High Speed Video Data 51

2.7.1 Frontal-View Video Experimental Setup 54

2.7.2 Frontal-View Traveling Wave Energy Analysis 56
2.7.3 Fourier Analysis of Frontal-View Cavitating Inducer Video . . 59
2.7.4 Characterization of Dynamic Cavitation Behavior Regimes Using Video TWE 62
2.8 Summary and Conclusions 64

3 A Review of Body Force Models for Turbomachinery Applications 67
3.1 Body Force Modeling of Turbomachinery 67
3.2 Model Overview and Assumptions 70
3.3 Blade Force Average Force Extraction 71
3.3.1 Force Extraction Process Validation 75
3.4 Previous Blade Passage Models 77
3.4.1 Blade Passage Model by Peters 81
3.4.2 Look-Up Table Approach 87
3.5 Summary 91

4 Inducer Blade Passage Model 93
4.1 Blade Passage Model by Sorensen 93
4.1.1 Normal Force Model 94
4.1.2 Parallel Force Model 96
4.1.3 Binormal Force Model 96
4.1.4 Blade Metal Blockage Model 97
4.1.5 Analytical Representation of Empirical Terms 98
4.1.6 Model Convergence Issues 99
4.2 Low Speed Axial Compressor Model Validation Case 102
4.2.1 Low Speed Axial Compressor Geometry 102
4.2.2 Aerodynamic Blockage Correction 104
4.2.3 Application of Aerodynamic Blockage to Axial Compressor Rotor Case 107
4.3 Body Force Modeling Challenges for Inducer Geometries 114
4.3.1 MIT Inducer vs. LSAC: Performance and Geometry Comparison 114

4.3.2 Radial Flow Redistribution Effects on Incidence Trends 119
4.3.3 Implication of Stagnation Pressure Loss Sensitivity with Incidence 119
4.4 Major Findings 125

5 Conclusions **129**
5.1 Summary 129
5.2 Recommendations for Future Work 131
5.2.1 Experimental Characterization of Cavitation Instabilities . . . 131
5.2.2 Inducer-Specific Body Force Model 132

List of Figures

1-1 Cavitation instability regimes in the LE-7 inducer [7]. 25

1-2 Onset of alternate blade cavitation in a four bladed inducer [10]. . . . 26

1-3 Attached cavity size growth, left to right, showing the formation of alternate blade cavitation due to the reduction in incidence caused when the flow turning at the rear of a cavity interacts with the leading edge of the adjacent blade for cavities larger than 65% of pitch [15]. . 27

1-4 Mechanism of rotating cavitation onset and propagation. Diagrams depict evolution in time and decreasing inlet pressure from top to bottom. Red regions in frontal-view represent tip vortex cavity. Adapted from [10]. 29

1-5 Tangential tip vortex trajectory wrapping around the leading edge of the adjacent blade [10]. 30

2-1 Aerospace Corporation's inducer cavitation test facility. 39

2-2 Axial and circumferential locations of dynamic pressure transducers. Direction of flow left to right in the in axial view, pressure tap locations marked with orange lines. Nonuniform circumferential spacing to minimize spatial aliasing [courtesy Aerospace Corporation]. 41

2-3 MIT inducer geometry. 42

2-4 Wetted performance of the MIT inducer. For experimental data, error bars are within size of symbol. 44

2-5 Steady cavitating performance of the MIT inducer. 46

2-6 Spectrogram of one dynamic pressure transducer at $\phi = 0.083$ showing alternate blade cavitation, rotating cavitation, and surge signatures. . 47

2-7 Power spectral density of one dynamic pressure transducer at $\phi = 0.083$ and $\sigma = 0.045$ showing a rotating cavitation signature at 1.5N. 48

2-8 Sketch of spatial harmonic modes for $n = 1, 2, 3$ for one instant in time – the sum of all spatial modes yields the pressure signal. 50

2-9 First harmonic TWE spectrogram for σ = 0.045-0.035, showing rotating cavitation signatures: forward rotating at 1.5N and backwards rotating at 2.5N. 52

2-10 Second harmonic TWE spectrogram for σ = 0.045-0.035, showing alternate blade cavitation signatures. 53

2-11 Cut-on/cut-off behavior between rotating cavitation and alternate blade cavitation, consistent with the rotating cavitation onset hypothesis described in Section 1.1.2. 53

2-12 Experimental setup for frontal-view borescope videos. Note that the actual lighting setup is not depicted – LEDs were distributed evenly around the optical section. 55

2-13 Custom borescope manufactured by Cortek Endoscopy. 55

2-14 Data reduction for video TWE. 57

2-15 Validation test case for video TWE showing 4N activity in the fourth spatial harmonic due to cavitating tip vortices. 58

2-16 Side-view and frontal-view video frames showing alternate blade cavitation at $\phi = 0.082$ [12]. 59

2-17 Side-view and frontal-view video frames showing rotating cavitation at $\phi = 0.082$ [12]. 60

2-18 TWE results for video of rotating cavitation, showing 1.6N signatures in the first spatial harmonic and low activity in the second spatial harmonic, corresponding with Figure 2-9. 60

2-19 TWE results for video of alternate blade cavitation, showing low activity in the first spatial harmonic and strong activity at 2N in the second spatial harmonic, corresponding with Figure 2-10. 61
2-20 TWE results for transient ramp test video, consistent with unsteady pressure measurements (Figure 2-11). 61
2-21 Rotating cavitation video analysis following Cervone's quantitative method [24], showing 1.6N activity, but lacking spatial mode detection. 63
2-22 FFT of ramp test video – compare with Figure 2-20, note the lack of activity seen in FFT. 64
2-23 Qualitative agreement between pressure and video TWE analysis. Discrepancies likely caused by uncertainty in cavitation number measurement. 65

3-1 Conceptual steps in body force modeling. 68
3-2 Body force modeling infinite blades assumption – "smeared out" representation of blade row [36]. 71
3-3 Natural coordinate system [37]. 73
3-4 Body force extraction grid for the MIT inducer. 75
3-5 MIT inducer RANS and body force characteristics, indicating good agreement while reflecting the body force model's difficulty in capturing the backflow region at lower flow coefficients. 77
3-6 Comparison of RANS and body force calculations for a range of flow coefficients. Extracted forces capture the bulk flow field with primary discrepancies in axial extent of backflow. Axial velocity contours nondimensionalized by tip velocity. 78
3-7 Streamwise axial velocity distributions throughout the MIT inducer blade domains. Primary discrepancy near backflow region at the leading edge tip. Axial velocity nondimensionalized by tip velocity. 79
3-8 Blade passage model by Peters [36]. 82

3-9 Peters model inherent stability – deviation component of normal force turns the flow towards local blade metal angle [36]. 83
3-10 Comparable magnitudes of total force for fan and inducer body force cases. Force contours nondimensionalized by inlet dynamic pressure. . 85
3-11 Normal force coefficients for inducer case are two orders of magnitude higher than fan case, resulting in model sensitivity. 86
3-12 Normal force components for the inducer are two orders of magnitude higher than the force itself as a consequence of the normal force coefficients (Figure 3-11). 86
3-13 Desensitization of normal force terms by introducing gains. 87
3-14 Look-up table sketch for single (x, r) point. 88
3-15 Double-valued (non-monotonic with flow coefficient) look-up table regions in the inducer, marked in red. 89
3-16 Monotonic normal force distribution as a function of relative velocity at midspan and 25% chord. 89
3-17 Multivalued normal force distribution as a function of relative velocity at the leading edge hub. 90
3-18 Narrow range of relative flow angle at midspan leading edge indicative of narrow range of incidence angles along inducer characteristic. . . . 91

4-1 Circumferential blade gap and blade pitch, defining passage free area ratio, B, adapted from [37]. 98
4-2 Analytical representation of an empirical term for a single (x, r) grid point. 99
4-3 Formation of spurious recirculation regions in inducer body force model for $\phi = 0.07$. Contours of axial velocity nondimensionalized by tip speed. 100
4-4 Development of spurious recirculation region only within full model region (outlined in red) for diagnostic test case at $\phi = 0.07$. Contours of axial velocity nondimensionalized by tip speed. 101
4-5 Low speed axial compressor geometry used for validation test case. . 103

4-6 Offset of velocities in midspan full model region in body force model at design point, $\phi = 0.385$, suggesting blockage model does not capture aerodynamic blockage. 105

4-7 Largest difference between pitchwise-averaged RANS and body force model relative velocities are near the endwalls, where boundary layer effects cause aerodynamic blockage. 107

4-8 LSAC RANS and body force characteristics. 108

4-9 LSAC full model (with blockage correction) results compared with pitchwise-averaged RANS at design point, $\phi = 0.385$. 109

4-10 Streamwise axial velocity distributions throughout the LSAC blade domain at design point, $\phi = 0.385$. Offset of the body force calculations from RANS is a consequence of the blockage correction. Velocity is nondimensionalized by tip speed. 110

4-11 LSAC suction side limiting streamlines indicating substantial separation at $\phi = 0.300$. 111

4-12 The body force model is able to capture the separated flow field at near stall conditions, $\phi = 0.300$. Contours of axial velocity nondimensionalized by tip speed. 111

4-13 Streamwise axial velocity distributions throughout the LSAC blade domain at stalled conditions, $\phi = 0.300$. 112

4-14 Blockage correction reduces difference (in percent) of calculated forces from pitchwise-averaged RANS extracted forces, but inducer model still experiences convergence issues. 113

4-15 Comparison of MIT inducer and LSAC characteristics. 115

4-16 Comparison of MIT inducer and LSAC loss as a function of flow coefficient, suggesting the inducer follows expected trends. 116

4-17 Comparison of loss buckets at different spanwise locations of the MIT inducer and LSAC. 117

4-18 Changes in nondimensional inlet midspan velocity triangle for the same change in flow coefficient. The change is markedly smaller for the inducer due to the highly tangential flow. c denotes absolute velocity. 118

4-19 High stagger angles cause narrow loss buckets due to nearly tangential flow imposed in inducer blade domain. The same absolute change in flow coefficient causes a much smaller change in incidence for the inducer than the compressor. 118

4-20 Sketch of tip vortex trajectories (in red) and associated radial flow redistribution for varying flow coefficients. 120

4-21 Side-view video data of tip vortex trajectories as indicated by their cavitation behavior at $\sigma = 0.1$ reflecting Figure 4-20 [12]. 121

4-22 Pitchwise-averaged contours of axial velocity, nondimensionalized by tip speed, showing separation at the hub at lower flow coefficients. . . 121

4-23 Comparison of empirical term characteristics at different spanwise locations of the MIT inducer and LSAC. 122

4-24 Large deviation gradients due to separation in the blade passage, resulting in force sensitivity. At 37% chord, separation is present only for lower flow coefficients, while downstream at 50% chord, separation becomes more severe, as seen in Figure 4-25. 123

4-25 Blade-to-blade view of the MIT inducer at 25% span – contours of relative velocity magnitude are nondimensionalized by tip speed. Separation along the blade increases as flow coefficient is reduced. Horizontal white artifacts in each passage are due to the calculations being single-passage; the passage is repeated for the blade-to-blade view postprocessing. 124

4-26 The deviation angle gradient captures tendency of the flow to deviate from local blade metal angle – the deviation angle gradients are higher in the presence of separation. 125

4-27 Ranges of deviation angle gradients across characteristic for each grid point. 126

List of Tables

1.1 Characteristics of cavitation instabilities observed in the LE-7 inducer [7]. 25

2.1 MIT inducer design data. 42

4.1 Low speed axial compressor rotor design data. 104

4.2 Comparison of inducer against LSAC geometry. 116

Nomenclature

Acronyms

ABC	alternate blade cavitation
BF	body force
CFD	computational fluid dynamics
DO	dissolved oxygen
ESA	European Space Agency
FFT	fast Fourier transform
HOT	higher order terms
IGV	inlet guide vane
JAXA	Japan Aerospace Exploration Agency
LE	leading edge
LPOP	low-pressure oxidizer pump
LSAC	low speed axial compressor
MIT	Massachusetts Institute of Technology
NASA	National Aeronautics and Space Administration
RANS	Reynolds-averaged Navier-Stokes
RC	rotating cavitation
SSME	Space Shuttle main engine
SST	shear-stress transport
TE	trailing edge
TWE	Traveling Wave Energy

Roman Symbols

B	passage free area ratio
c	blade chord
c_p	pressure coefficient
f	force
h	staggered blade spacing
h	enthalpy
h_t	stagnation enthalpy
Im	imaginary
j	imaginary unit
K_l	parallel force coefficient
K_n	normal force coefficient
K_{off}	offset constant
K_r	radial force coefficient
M	Mach number
N	synchronous frequency
N_B	number of blades
p	pressure
p_t	stagnation pressure
r	radius
r_{tip}	tip radius
Re	real
s	entropy
S_m	mass source term
t	time
T	temperature
u,c	absolute velocity
u_{tip}	tip speed
w	relative velocity

Greek Symbols

β	relative flow angle
δ,δ_β	deviation angle
δp_n	n-th harmonic spatial Fourier coefficient
δ_φ	pitch angle deviation
θ	angular position
κ	blade metal angle
λ	blade lean angle
ρ	density
σ	cavitation number
σ	solidity
ϕ	flow coefficient
ϕ_l	local flow coefficient
φ	pitch angle
φ_{GP}	geometric gas path angle
ψ	head coefficient
ω	loss coefficient
Ω	shaft speed

Subscripts

1	inlet/leading edge value
2	outlet/trailing edge value
δ	deviation component
η	passage-aligned component
h	binormal component
l	parallel component
m	meridional component
n	normal component
∇p	blade loading component
r	radial component
rel	in the relative frame
θ	circumferential component
x	axial component
ξ	cross-passage component

Superscripts

$\bar{}$	pitchwise-averaged quantity

Chapter 1

Introduction

1.1 Background and Motivation

Liquid-propellant rockets require high power density turbopumps to deliver pressurized propellant for combustion while reducing overall system weight. To prevent cavitation in the main turbopump, inducers are often used upstream to provide an initial pressure rise. Consequently, inducers are subject to cavitation under normal operating conditions and must be designed to account for both hydrodynamic and mechanical considerations – inducers must not only provide the required head rise under detrimental cavitating conditions, but must also withstand the stresses imparted by cavitation.

Due to an insufficient characterization of the governing physical mechanisms, combined with limitations in predictive capability, unsteady cavitation phenomena are particularly difficult to identify early in turbopump development. Cavitation instabilities can cause severe vibrations within the turbopump, causing fluctuations in engine thrust and possibly total mechanical failure. Cavitation behavior in inducers have caused issues during numerous rocket development programs, including JAXA's LE-7 [1], NASA's Space Shuttle main engine (SSME) RS-25 [2], ESA's Vulcain [3], and NASA's Fastrac [4]. Moreover, cavitation problems are generally discovered in the later stages of development through experimental testing. In the notable case of the LE-7, during the eighth mission of the H-II rocket, the hydrogen inducer suffered

from vibration caused by rotating cavitation, eventually resulting in fatigue failure and complete loss of mission [5].

The design and testing of turbopumps represent a substantial component of rocket development programs and can consist of up to 50% of program costs [6]. There is therefore a critical need for a better characterization of unsteady cavitation phenomena – despite extensive research, the physical mechanisms of cavitation instabilities are not fully understood and there is currently no established methodology for predicting the onset of cavitation instabilities during the design phase. The identification of the mechanisms governing cavitation instabilities enables the definition of first principles based design guidelines for inducers to suppress cavitation instabilities, and the resulting improvement of design increases the affordability, reliability, and performance of turbopumps. Currently under development, NASA's Space Launch System will use SSME-derived RS-25D/E engines for its core stage and, in particular, directly benefits from advancements in turbopump design.

1.1.1 Cavitation Instabilities in Inducers

The presence of cavitation instabilities in inducers is dependent on the inducer geometry itself and the operating conditions. Many distinct cavitation instabilities have been observed, some of which are outlined in Figure 1-1 and the corresponding Table 1.1.

The cavitation instabilities of most interest are cavitation surge and rotating cavitation. Cavitation surge is characterized by violent one dimensional oscillations in the pressure and flow rate for the entire system, generating vibration and reducing performance [8]. Cavitation surge is similar to surge seen in aero-engine compressors – the cavitation bubbles themselves provide the necessary compliance [9]. Rotating cavitation is characterized by super-synchronous rotation of cavities around the periphery of the inducer, unlike rotating stall, which propagates slower than shaft speed [8]. Rotating cavitation can cause asymmetric vibration in the pump, degrading performance and ultimately causing damage to the turbopump, and is the primary instability of concern for this work.

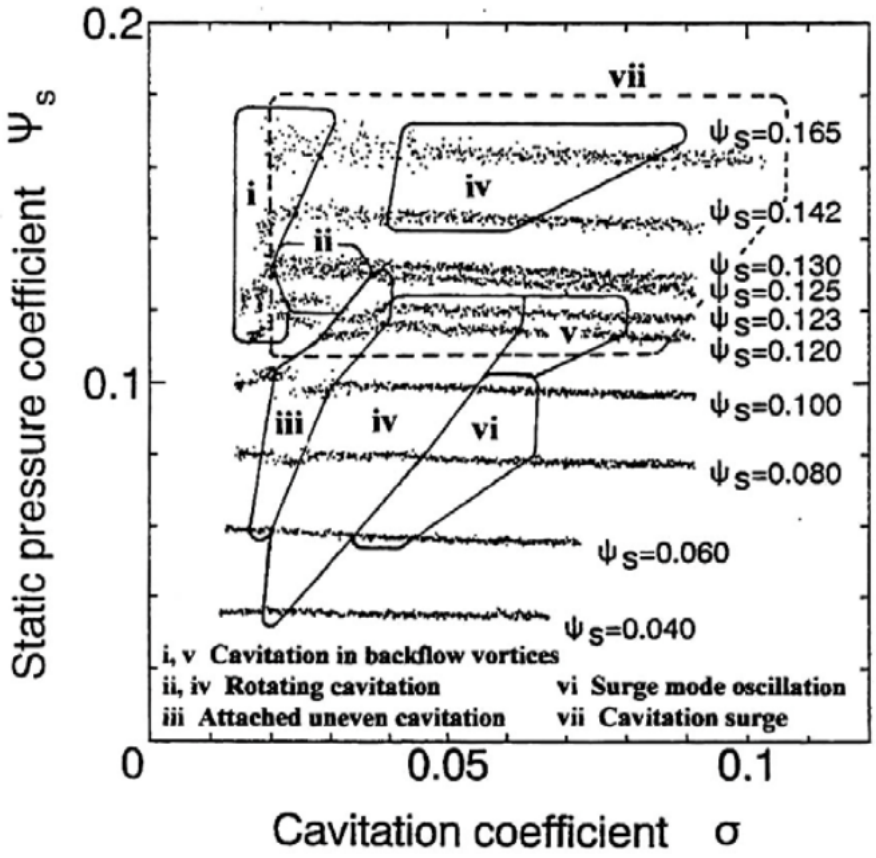


Figure 1-1: Cavitation instability regimes in the LE-7 inducer [7].

Table 1.1: Characteristics of cavitation instabilities observed in the LE-7 inducer [7].

		Number of cells, n	Rotational velocity ratio, $f/(nf_N)$
i	Cavitation in backflow vortices	5	0.16
ii	Rotating cavitation	1	0.9
iii	Attached uneven cavitation	1	1.0
iv	Rotating cavitation	1	$1.1 - 1.3$
v	Cavitation in backflow vortices	5	0.21
vi	Surge mode oscillation	0	18 Hz/(3300 − 5000 RPM) (proportional to RPM)
vii	Cavitation surge	0	$8 - 19$ Hz/4000 RPM (proportional to RPM)

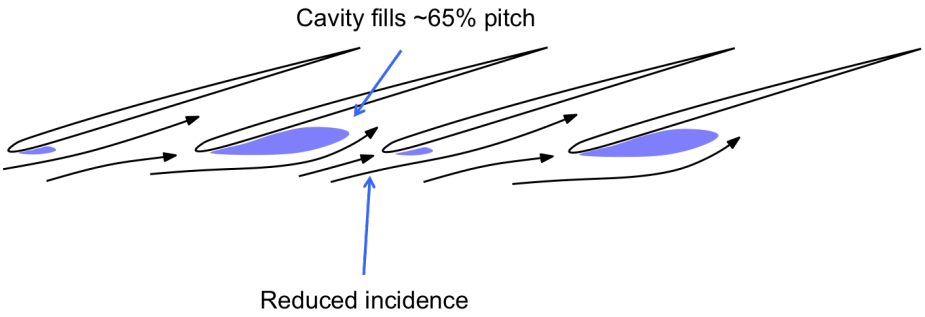


Figure 1-2: Onset of alternate blade cavitation in a four bladed inducer [10].

1.1.2 Recent Findings on the Mechanism of Rotating Cavitation Onset

Recently, Lettieri et al. [10–12] hypothesized the mechanism of the formation and propagation of rotating cavitation, proposing the fundamental mechanism behind its onset and identifying the critical inducer design parameters.

Previous work studying the mechanism of rotating cavitation indicated that under certain conditions, cavities are synchronous and attached to the inducer blades. In the case of a four bladed inducer, the cavities can occur on alternate blades and is termed alternate blade cavitation (called attached uneven cavitation in Figure 1-1 and Table 1.1, or asymmetric cavitation – in an inducer with an uneven number of blades, the cavities are attached to one or two blades) [13]. For a four bladed inducer, alternate blade cavitation is quasi-stable with relatively little vibration. It was also observed that at the rear of the cavities, the flow turns toward the suction side of the blade [14]. At operating conditions where blade cavities reach approximately 65% of the blade pitch, this flow turning interacts with the neighboring blade, causing a reduction in incidence angle and an associated decrease in cavity length on the affected blade, thereby causing alternate blade cavitation [14, 15]. Alternate blade cavitation is sketched in Figure 1-2, while velocities in a cascade under different cavity sizes is shown in Figure 1-3, illustrating the flow turning at the rear of cavities and its effect on the incidence of the adjacent blade. Notably, it was shown that alternate blade cavitation is a precursor to rotating cavitation [16, 17].

A parallel may be drawn between the effect of attached blade cavitation blockage

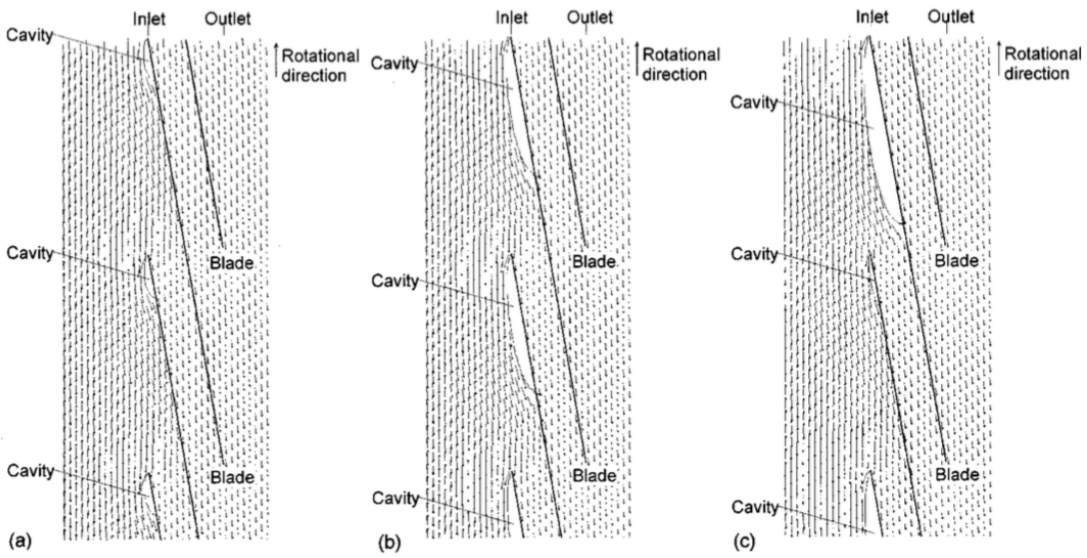


Figure 1-3: Attached cavity size growth, left to right, showing the formation of alternate blade cavitation due to the reduction in incidence caused when the flow turning at the rear of a cavity interacts with the leading edge of the adjacent blade for cavities larger than 65% of pitch [15].

and blockage from separation in a stall cell in gas turbine compressors. As the cavity grows, the neighboring blade increases in incidence due to blockage effects tangentially diverting the incoming flow, the same mechanism that increases incidence for the adjacent blade in the presence of a stall cell [18]. However, as noted above in the description of alternate blade cavitation inception and seen in Figure 1-3, separation and cavity behavior differ due to the critical cavity length. Once the cavity size reaches 65%, the flow turning at the rear of the cavity, known as cavitation break-off, instead reduces the incidence of the adjacent blade. It is important to note this distinction when considering the mechanism behind rotating cavitation onset.

Previous work also indicated the importance of tip vortex trajectory and incidence on rotating cavitation inception. It was noted that at operating conditions where rotating cavitation was seen, the tip vortex of one blade interacts with the leading edge of adjacent blades [19]. Additionally, rotating cavitation was shown to be the perceived motion generated by the growth and collapse of individual cavities on the blades [14, 20, 21]. The rotating behavior of the blade cavities was seen to be linked to the change in incidence angle caused by cavity collapse, manifesting as forward-

rotating cavitation as seen in the absolute frame [13]. A correlation was also shown between the onset of rotating cavitation and the ratio between the inlet static pressure and incidence angle [9].

However, the onset of rotating cavitation was still not fully characterized. The cause of alternate blade cavitation breakdown and the mechanism that dictates the propagation rate and direction of rotating cavitation were unclear. Moreover, the inducer design parameters that govern rotating cavitation inception were unknown.

Lettieri et al. [10] hypothesizes that rotating cavitation onset stems from the breakdown of alternative blade cavitation in operating conditions where the tip vortex trajectory is nearly tangential and interacts with the adjacent blade. A schematic of the mechanism is shown in Figure 1-4.

Generated by the pressure difference between a blade's suction side and pressure side pushing flow upstream of the inducer leading edge, the trajectory of the tip vortex is determined by the incidence. At higher incidence angles, the blades are more loaded and the tip vortex is pushed upstream. At lower incidence angles, the tip gap flow is decreased and the tip vortex is directed into the blade passage. For rotating cavitation inception, the tip vortex trajectory is tangential, as shown in Figure 1-5. The vortex lines wrap around the leading edge of the adjacent blade, forming a region of low pressure and therefore causing cavitation in the region, shown at time instant t_1 in Figure 1-4. From alternate blade cavitation, the cavity could occur at either non-cavitating blade – manufacturing tolerances and/or asymmetric tip clearances determines the specific blade.

The presence of the tip cavity increases blockage and therefore incidence for the affected blade (blade 2 in Figure 1-4). The higher incidence causes the cavity on blade 2 to grow due to higher overspeed and lower associated pressure. The blade 2 cavity grows in the passage, and, as noted previously, incidence increases for blade 3; the cavity on blade 3 grows as a result at t_2). At t_3, rotating cavitation has formed. Once the cavity on blade 3 reaches approximately 65%, there is a reduction in incidence for blade 4 at t_4 which causes the attached cavity to collapse and consequently allows the tip cavity to reform on the neighboring blade, blade 1 from $t_5 - t_6$. The tip cavity

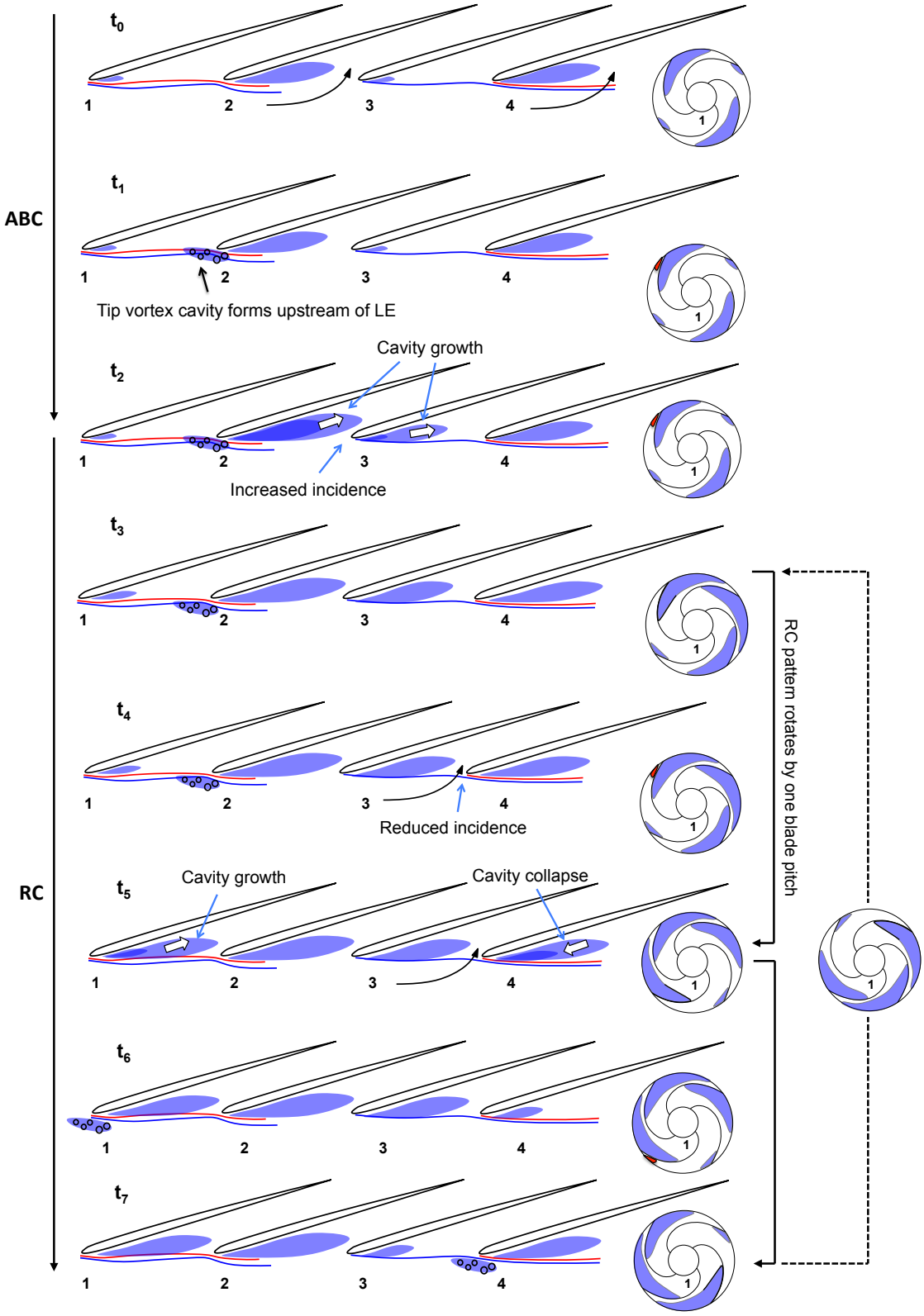


Figure 1-4: Mechanism of rotating cavitation onset and propagation. Diagrams depict evolution in time and decreasing inlet pressure from top to bottom. Red regions in frontal-view represent tip vortex cavity. Adapted from [10].

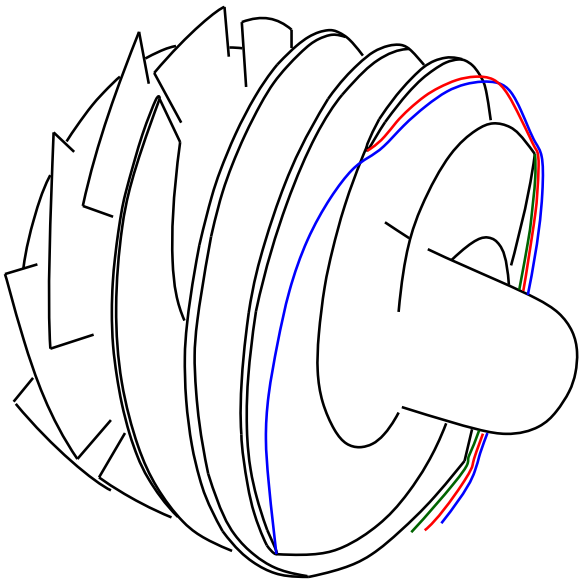


Figure 1-5: Tangential tip vortex trajectory wrapping around the leading edge of the adjacent blade [10].

propagates in the direction of rotation, causing the periodic growth and collapse of cavities, which yields the super-synchronous rotation observed as rotating cavitation.

The relevant inducer design parameters are therefore identified as leading edge blade metal angle, tip radius, tip gap size, leading edge backsweep angle, and the rotational speed.

Lettieri et al. [10–12] investigate this hypothesis using single- and two-phase simulations, experimental inlet pressure measurements, and high speed video. The research in this thesis was conducted concurrently and proposes two methods of verifying the hypothesized mechanism, namely with an experimental tool and a reduced order model.

1.2 Problem Statement and Previous Work

While previous work has revealed substantial insight into unsteady cavitation behavior, as seen in Section 1.1.2, advancements in aero-engine turbomachinery assessment methods offer the potential for clarification as well as new learning about cavitation instability mechanisms if adapted to inducer geometries.

1.2.1 Experimental Characterization of Cavitation Instabilities

Experimental methods for investigation of cavitation instabilities are limited in their ability to definitively determine key characteristics, such as rotation direction or individual spatial harmonic content. The Traveling Wave Energy (TWE) methodology, previously developed for rotating stall detection in compressors, is proposed to address these challenges.

Generally, cavitation instabilities are experimentally investigated through spectral analysis of unsteady static pressure data [14, 20, 22] and/or high speed video of the cavitating inducer, either side-view or frontal-view [21]. A more extensive discussion of experimental methods in the context of cavitation instabilities in inducers can be found in [7, 23] and [21] for pressure and optical measurements, respectively. Several challenges arise from the conventional methods.

For experimentally obtained pressure data, it is difficult to discern the direction and modes of propagation of the cavities. Tsujimoto [14] utilized cross-correlation and phase analysis methods to infer propagation direction, and later, a similar method, termed Hannover plotting, was used by Zoladz [4]. Hannover diagrams examine the phase relations between pressure transducers to determine inter-sensor phase. The inter-sensor phase is plotted against transducer spacing and a best-fit line is approximated to the data – the slope of the line indicates the direction of rotation. However, results from Hannover diagrams may be ambiguous due to the necessity of defining a reference signal for calculating phase.

In the case of high speed video, Cervone [24] used image processing algorithms to obtain unsteady tip cavity length data from frontal-view videos, successfully using Fourier analysis to correlate instability frequencies obtained from optical data against frequencies from pressure data. However, the image processing techniques used cause loss of spatial information from the optical measurements. The optical measurements (side-view and frontal-view cameras) are also complicated and costly to setup when compared to high speed pressure transducers. High speed videos have primarily been

used as a visual aid and very little quantitative data has been extracted from optical data in the context of cavitating inducers.

TWE analysis addresses the above limitations of current experimental methods, allowing the determination of frequency, spatial mode shapes, and rotation direction. Conventional spectral analysis does not reveal spatial harmonic content, while, for $2n$ sensors (e.g. a circumferential pressure transducer array), TWE can resolve up to n spatial harmonics. TWE is also advantageous over Hannover analysis due to its explicit definition of rotation direction.

After suitable data reduction, high speed video frame pixels can be treated as a continuum of sensors, enabling TWE analysis to be used for optical measurements. TWE analysis of frontal-view high speed video therefore allows the investigation of the radial characteristics of cavitation instabilities. It is hypothesized that cavitation behavior is dominated by circumferential wave patterns with negligible radial variation and that pressure transducers can therefore be established as the primary method, thereby negating the need for high speed video and simplifying experimental setups.

1.2.2 Modeling of Cavitation Instabilities

Rotating cavitation modeling generally relies on experimental data for key parameters, restricting its use in the inducer design phase. An adaptation of the so-called body force methodology is proposed as a tool for both design studies as well as defining a preferred inducer geometry and/or casing treatment.

The first reduced-order models of cavitation instabilities in the context of inducers were formulated by Brennen [25], who used linearized one-dimensional transfer matrices requiring the computation of two key parameters, termed the cavitation compliance and the cavitation mass gain factor, to predict the stability of the pumping system. Tsujimoto [26] expanded Brennen's model using a two-dimensional actuator disk method to address rotating cavitation. Tsujimoto concluded that rotating stall and rotating cavitation were two distinct phenomena and found the propagation speed of rotating cavitation estimated by the model in fair agreement with experi-

ment. Brennen, Kamijo, and Tsujimoto [9] defined a unified model to account for four instabilities in inducers – surge, rotating stall, cavitation surge, and rotating cavitation. Surge and cavitation surge were assumed to be one-dimensional while rotating stall and rotating cavitation were treated as two-dimensional. The unified model confirmed the existence of a backward rotating mode for rotating cavitation along with the forward rotating mode. Watanabe [27] proposed a three-dimensional model with assumptions made for the cavitation compliance and cavitation mass gain factor. Rotating cavitation was shown to be largely unaffected by three-dimensional effects, but Watanabe noted that more fidelity in the parameter assumptions was needed. Despite advancement in these efforts (e.g. [28–30]), most methods rely on experimental data, rendering them generally unusable during the inducer design process, and those formulated without empirical parameters are not very accurate [31].

The continued increase of computational capability combined with improvements in two-phase CFD methods has led to applications of high fidelity calculations to turbopump inducers. Simulations have been successful in capturing some aspects of rotating cavitation. Iga [32] used a flat-plate three-bladed cascade to simulate rotating cavitation and cavitation surge, finding indications of a link between cavitation sheet break-off and rotating cavitation propagation. Spectral analysis of Hosangadi's unsteady Reynolds-averaged Navier-Stokes calculations of the SSME low pressure fuel pump [33] showed similar spectra as experimental data. From his simulations, Hosangadi also noted the importance of cavity interaction with the neighboring blade for rotating cavitation onset. However, high fidelity simulations are computationally costly and accurate two-phase numerical methods are still in the early stages of development – practical computational models of inducers are still many years away [31].

Body force modeling has been used for a wide range of aeronautics-related problems, including compressor stability prediction [34], multiple-pure-tone fan noise assessment in serpentine inlet ducts [35], and the investigation of fan/inlet coupling in short turbofan nacelle inlets [36]. A successful body force model applied to inducers allows the capture of cavitation instabilities at reduced computational cost,

resulting in a capability to guide the design of inducers that suppress rotating cavitation instabilities. As part of the research effort described in the present work, an inducer-specific body force model was developed by Sorensen [37]. The model experienced convergence issues, manifesting as spurious recirculation regions. Based on diagnostic tests described in the present work, it is hypothesized that the issues are a consequence of the unique inducer geometry, namely the low flow coefficient design and associated high stagger angles, and the related sensitivities of stagnation pressure loss to changes in incidence.

1.3 Research Goals and Objectives

The overall objective of this research is the characterization of cavitation instabilities, primarily rotating cavitation. The work described in this thesis aims to assess the hypothesis of the onset and propagation of rotating cavitation through experimental analysis and a modeling approach. The primary goals are therefore to:

- Experimentally characterize cavity dynamic behavior using an adaptation of the Traveling Wave Energy analysis to inducer unsteady pressure measurements.
- Assess the feasibility of Traveling Wave Energy analysis for frontal-view video of cavitating inducers. Corroborate outcomes with pressure measurement results to determine if a pressure transducer array can be established as the primary detection method for cavitation behavior, thereby reducing experimental costs.
- Assess the limitations of the applicability of body force modeling by investigating convergence issues in the inducer-specific body force model and determining its root cause. Determine impact of inducer geometry on model sensitivity.

1.4 Thesis Contributions

The key accomplishments of this work can be summarized as follows:

- The successful demonstration of TWE for analysis of cavitation instabilities addresses several limitations in the current experimental methods. TWE is demonstrated to be able to resolve frequency, spatial mode shapes, and rotation direction of cavitation instabilities from inlet pressure measurements of cavitating inducers, and is therefore advantageous over the standard spectral analysis and Hannover diagrams, which cannot discern spatial harmonic content and ambiguously defines rotation direction, respectively.

- TWE analysis of unsteady inlet pressure measurements led to the identification of distinct cut-off/cut-on behavior for alternate blade cavitation and rotating cavitation, experimentally confirming the link between the two phenomena as hypothesized.

- TWE analysis was successfully adapted to interrogate frequency content and spatial mode shapes of frontal-view optical measurements of a cavitating inducer, yielding a new tool for the characterization of cavitation instabilities. Cavitation instability signatures, namely rotating cavitation and alternate blade cavitation, are extracted from high speed video data, qualitatively correlating with results from unsteady pressure data. Video TWE is demonstrated to extract frequency and spatial harmonic content from both steady and transient operating conditions, yielding more information that current quantitative analysis of high speed video of inducers.

- A video TWE parametric study revealed less than 2% radial variation of instability signatures, indicating rotating cavitation and alternate blade cavitation are governed by circumferential wave patterns. This suggests that pressure measurements can be established as the primary detection method for cavitation behavior over high speed video, thereby simplifying experimental setups.

- The inducer-specific body force model formulation by Sorensen was discovered to be unable to capture aerodynamic blockage. Once corrected, the inducer-specific body force model formulation is demonstrated to be valid and robust

using a low speed axial compressor diagnostic test case. The body force model is able to capture off-design performance even in near stall conditions.

- Diagnostic tests indicated the low flow coefficient design of the inducer and the associated high blade stagger angles as the limiting factor in body force modeling applicability. The nearly tangential flow seen in the inducer blade domain gives rise to sensitivity of stagnation pressure loss to incidence angle. This, combined with flow separation throughout most of the inducer's operating range manifests as model sensitivity, causing spurious recirculation regions and convergence issues. The results therefore suggest that the blade passage model by Sorensen is a viable body force modeling approach for conventional aero-engine turbomachines, such as fans and compressors, typified by their higher flow coefficient designs and lower stagger angle geometries, or inducer designs with little flow separation. Desensitization is needed for application of the body force model to the inducer geometry investigated in the present work (e.g. a force limiter).

1.5 Organization of Thesis

The remainder of this thesis is outlined as follows: Chapter 2 details the experimental campaign undertaken at Aerospace Corporation's cavitating inducer test facility. Analysis of unsteady pressure measurements and high speed video data using both conventional methods as well as the Traveling Wave Energy methodology are presented. Chapters 3 and 4 focus on the modeling aspect of this research. Chapter 3 describes the body force model, the force extraction procedure, and attempts to adapt previous body force models to the inducer. Chapter 4 introduces the inducer-specific approach to body force modeling and presents the diagnostics undertaken to identify the root cause for its convergence issues. Chapter 5 summarizes the research presented and provides recommendations for future work.

Chapter 2

Experimental Assessment of MIT Inducer Performance and Cavitation Behavior

A representative inducer geometry, termed the MIT inducer, was designed with the intent to replicate the steady and dynamic behavior of the Space Shuttle main engine (SSME) low-pressure oxidizer pump (LPOP). The MIT inducer was the subject of a series of three separate test entries conducted at the Aerospace Corporation's inducer cavitation test facility, each targeting a different measurement technique. High speed inlet pressure measurements, side-view video, and frontal-view video with a borescope were taken of the cavitating inducer.

The data was analyzed using the Traveling Wave Energy methodology, yielding the temporal evolution of both the frequency content and mode shapes, the results of which were used to experimentally characterize the dynamic cavitation behavior of the MIT inducer. The hypothesized link between alternate blade cavitation and rotating cavitation was confirmed and the frontal-view data suggested both cavitation phenomena are governed by circumferential wave patterns.

2.1 Experimental Setup

The Aerospace Corporation's test facility in El Segundo, California was designed to provide a flexible testbed for the rapid and low-cost investigation and characterization of dynamic cavitation phenomena in rocket engine turbopumps. A summary of its capabilities is presented here; an in depth discussion is given in [38].

The facility is able to precisely control the operating conditions of the test article by setting the flow coefficient and cavitation number. The flow coefficient, ϕ, is a nondimensional measure of incidence, given by

$$\phi = \frac{u_1}{r_{tip}\Omega} \tag{2.1}$$

where u_1 is the inlet flow axial velocity, r_{tip} is the tip radius, and Ω is the inducer rotational speed. Cavitation number (or Euler number), σ, nondimensionally represents the inlet pressure,

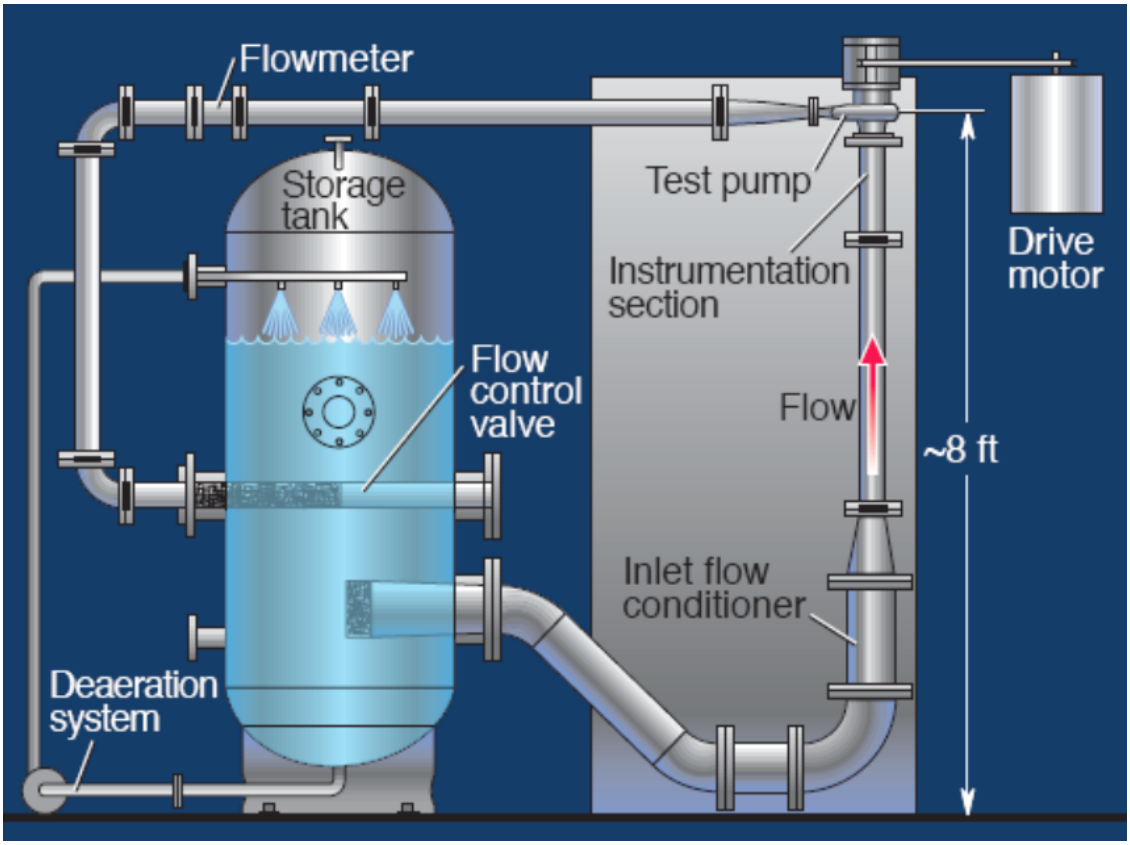
$$\sigma = \frac{p_1 - p_{vapor}}{\frac{1}{2}\rho\left(r_{tip}\Omega\right)^2} \tag{2.2}$$

where p_1 is the static pressure at the inducer inlet plane, p_{vapor} is the fluid vapor pressure at inducer inlet conditions, and ρ is the fluid density. Both numbers determine the performance of the inducer, represented nondimensionally by head coefficient, ψ,

$$\psi_{tt} = \frac{p_{t_2} - p_{t_1}}{\rho\left(r_{tip}\Omega\right)^2} \tag{2.3}$$

where p_t is the total pressure, taken at the inducer inlet and outlet. The facility is also able to set thermal conditions to investigate its impact on cavitation behavior – more details can be seen in [39,40]. The control of these parameters allows the facility to achieve dynamic similarity with flight operating conditions using scaled models.

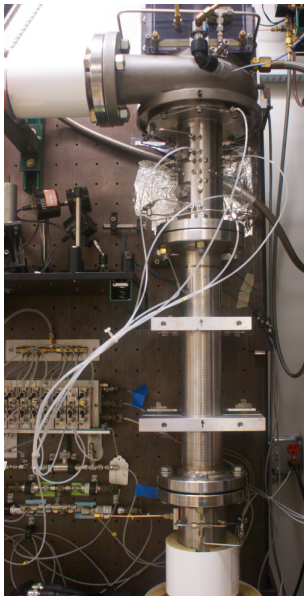
Pictures and a schematic of the closed-loop facility is shown in Figure 2-1. From the storage tank, water, the working fluid, enters the piping system through a honeycomb inlet before passing through an inlet flow conditioner into the 76 millimeter diameter vertical pipe containing the instrumentation section and test article. The



(a) Schematic of facility [38]



(b) Picture of facility



(c) Close-up of instrumented test section for pressure transducers

Figure 2-1: Aerospace Corporation's inducer cavitation test facility.

inlet flow conditioner and the 0.72 meter (9.5 diameters) of inlet piping ensures a uniform inlet velocity field into the test pump. After exiting the test pump, a volute returns the flow to horizontal and the water passes through the flowmeter and a boost pump (not shown) before returning to the reservoir tank through a flow control valve.

The operating conditions in the facility are carefully monitored and controlled. The porous media flow control valve sets the flow coefficient, while system pressure (and consequently cavitation number) is controlled through the ullage volume pressure at the top of the storage tank. Cavitation phenomena are also known to be sensitive to impurities in the fluid, which serve as nucleation sites [8]. The facility is able to purge dissolved gases from the system by introducing helium bubbles into the bottom of the storage tank, allowing dissolved gases in the water to diffuse into the bubbles and exit the water into the tank ullage. A dissolved oxygen meter monitors the dissolved gas level in the system, referred to as DO. In addition, other contaminants are filtered out of the water using a 1-micron bag filter. Before all tests, the working fluid was circulated through the filter as well as deaerated to the desired DO level.

The facility accommodates a variety of test inducers up to 76 millimeters in diameter at speeds up to 5000 RPM. The inducer is mounted vertically to eliminate the hydrostatic pressure gradient present in horizontal configurations, removing potential uncertainty stemming from its effect on cavitation number. The main drive shaft of the test inducer is designed to easily accept a variety of inducer geometries using an interface shaft that couples to the main shaft.

Setting operating conditions and measurement acquisition are both interfaced through LabVIEW and a 32-channel, high-speed, simultaneous sampling data acquisition system. Performance pressure data is measured using Druck pressure transducers, sampled at 1 hertz. The flowrate is measured with a Foxboro electromagnetic flowmeter. Pump rotational speed and rotor position are measured using a BEI optical shaft encoder.

The instrumentation section is interchangeable between a pipe section drilled with pressure taps for dynamic pressure transducers and an optical access section made from acrylic. For the high speed pressure measurements, ten measurement planes of

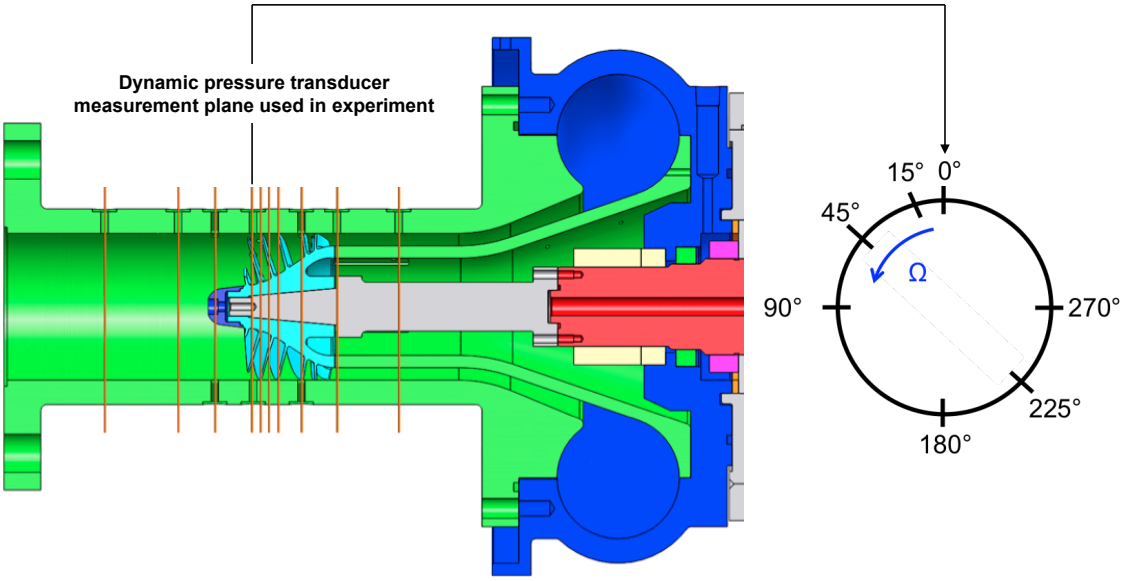


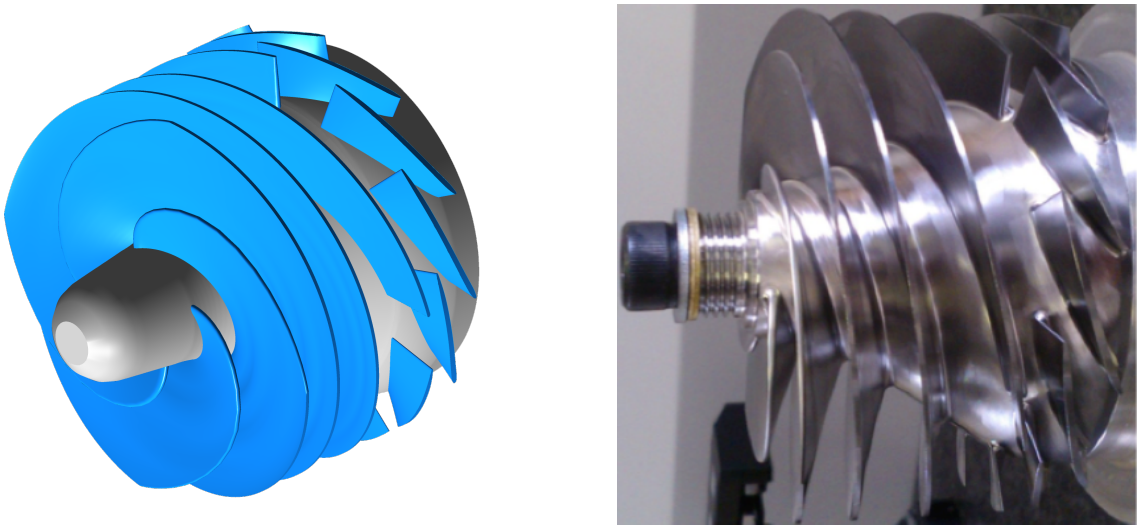
Figure 2-2: Axial and circumferential locations of dynamic pressure transducers. Direction of flow left to right in the in axial view, pressure tap locations marked with orange lines. Nonuniform circumferential spacing to minimize spatial aliasing [courtesy Aerospace Corporation].

pressure taps are drilled into the instrumentation section, extending ten diameters upstream and one diameter downstream of the test article. In this research, an array of seven Entran miniature pressure transducers was used at the inducer tip plane, sampling at 25 kilohertz. Circumferential and axial locations are shown in Figure 2-2. The pressure transducers were arranged nonuniformly to minimize spatial aliasing and improve spatial harmonic resolution.

2.2 MIT Inducer Geometry

A summary of the geometry of the MIT inducer is presented here. A more comprehensive discussion of the MIT inducer design is given in [10].

The MIT inducer was designed based on open source data of the low-pressure oxidizer pump (LPOP) of the Space Shuttle main engine (SSME) and captures both its steady and dynamic behavior. The MIT inducer geometry exhibits many of the same characteristics as modern inducers, namely high blade stagger angles, forward canted blades, a backswept leading edge, and gas path area contraction. The inducer



(a) Computational model (b) Test hardware (without nose cone)

Figure 2-3: MIT inducer geometry.

Table 2.1: MIT inducer design data.

	Inducer	Kicker
Design flow coefficient	0.07	
Design total-to-total head coefficient	0.35	
Number of rotor blades	4	12
Inlet hub-to-tip ratio	0.29	0.74
Outlet hub-to-tip ratio	0.72	0.83
Inlet blade angle at tip	82.7°	81°
Outlet blade angle at tip	74°	60°
Leading edge backsweep	120°	0°
Inlet tip gap relative to span	0.01	0.027

is followed by a set of tandem blades, also called the "kicker", whose purpose is to further increase head rise. An outline of the MIT inducer geometry is given in Table 2.1.

2.3 MIT Inducer Steady Performance

Both the steady wetted and cavitating performance of the MIT inducer was compared across the three test entries along with steady CFD to ensure repeatability and consistency.

2.3.1 Wetted Performance

The steady CFD simulations were single-passage RANS calculations run using ANSYS CFX and its k-ω shear stress transport (SST) turbulence model. The MIT inducer mesh is approximately 2 million elements, created using ANSYS Turbogrid. The inlet was placed 10 diameters upstream of the inducer leading edge with a total pressure boundary condition while the outlet was placed 5 diameters downstream of the kicker trailing edge with a mass flow boundary condition, which sets the flow coefficient. No-slip wall boundary conditions were used for the blades, hub, and shroud.

Experimental and computational wetted performance of the MIT inducer is shown in Figure 2-4. During the experiments, the storage tank was vented to atmosphere to ensure fully wetted conditions. Performance data was taken at each flow coefficient, allowing steady state conditions to be established for each point. Both directions of the flow coefficient range were traversed to check for hysteresis and transducer zero drift. The slopes of the characteristics are in good agreement between the computations and experiments. A maximum of 15% difference is seen between the computational and experimental head coefficients, and a maximum of 10% difference is seen between the three experiments.

2.3.2 Steady Cavitating Performance

Inducer cavitating performance is typically characterized through a head fall-off curve, or "knee curve", where head rise is plotted against cavitation number. Lower cavitation numbers represent more cavitation, which eventually restricts flow through the inducer and degrades performance.

The RANS simulations were computed using the same setup as described in Section 2.3.1 with the ANSYS CFX two-phase model enabled. The CFX cavitation model is based on the Rayleigh-Plesset model to determine vapor bubble formation and growth. Details of the two-phase model used can be found in [11].

Comparison of experimental and computational head fall-off curves at $\phi = 0.082$ is seen in Figure 2-5a. For each experimental knee curve, cavitation number was set

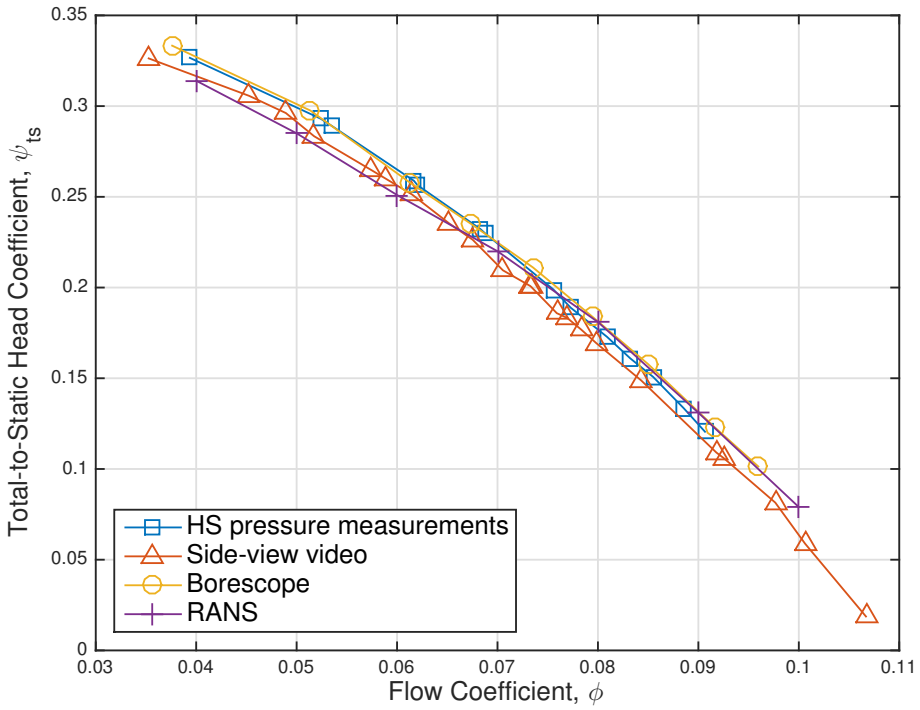


Figure 2-4: Wetted performance of the MIT inducer. For experimental data, error bars are within size of symbol.

using the ullage pressure. Performance data was taken at each desired cavitation number, also allowing steady state conditions to be established for each point as well as spanning both directions of the cavitation number range. While repeatability was again demonstrated between experiments, there is a significant difference between the calculation and experiments. The large discrepancies are likely due to the role of alternate blade cavitation and rotating cavitation in decreasing vapor bubble blockage relative to that predicted by the RANS calculations – the operating conditions spanned in the head fall-off curve are affected by cavitation instabilities (inducer dynamic behavior and cavitation instability regimes will be discussed in depth in Section 2.4). Single-passage steady RANS is unable to model the coupling between blade passages that produces the cavitation instability behavior, leading to incorrect prediction of head rise. The large discrepancies attest to the need for a model that is able to predict cavitation instabilities and their effects on inducer performance. At lower flow coefficients where cavitation instabilities are less prevalent [13], the com-

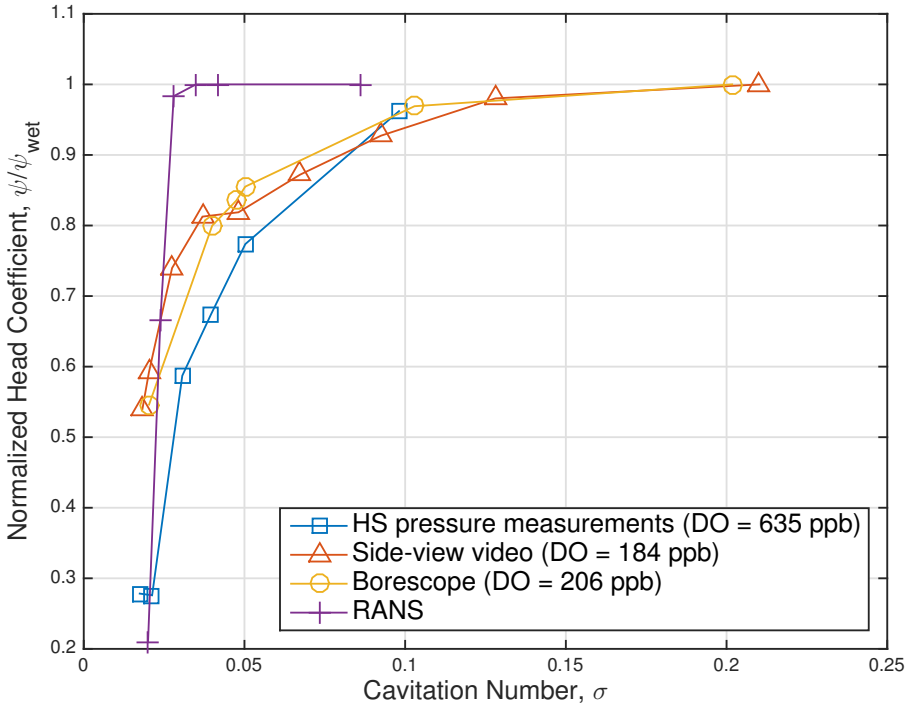
putations are in much closer agreement with the experimental performance as seen in Figure 2-5b; differences are less than 2%.

2.4 Dynamic Behavior of Four Bladed Inducers

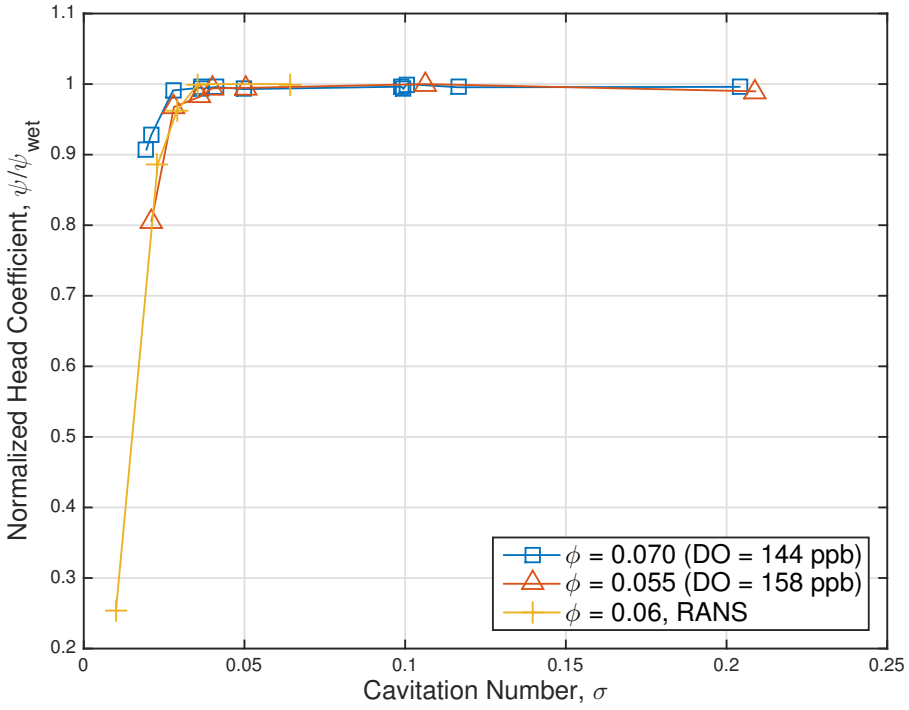
As described in Section 1.2.1, inducer dynamic behavior is typically characterized through spectral analysis of unsteady pressure data. Using the high speed pressure transducer setup described in Figure 2-2, data was taken during a cavitation ramp test for selected flow coefficients. The tank ullage pressure was slowly lowered or raised, changing the cavitation number across the desired range. The inducer was set to 4000 RPM with the boost pump off.

From the hypothesis described in Section 1.1.2 and knowledge that rotating cavitation occurs at conditions near design (i.e. nominal operation) [4], a series of ramp tests were carried out at flow coefficients around design to find the operating conditions where rotating cavitation and the associated alternate blade cavitation occur in the MIT inducer. Rotating cavitation is characterized by rotational velocities approximately between 1.1 and 1.3 times shaft speed [7] while alternate blade cavitation for a four bladed inducer propagates at 2 times shaft speed [15].

Rotating cavitation and alternate blade cavitation signatures were seen at flow coefficients around $\phi = 0.083$. The spectrogram for one pressure transducer during a ramp test is seen in Figure 2-6. Alternate blade cavitation signatures are seen at $\sigma = 0.055$-0.048, then a cut-off of alternate blade cavitation and a cut-on of rotating cavitation at $\sigma = 0.048$-0.042. Rotating cavitation signatures are first seen at 1.6 times shaft speed, which decreases with cavitation number. Rotating cavitation ends and alternate blade cavitation begins again from $\sigma = 0.042$-0.038. The spectra at lower cavitation numbers, approximately lower than $\sigma = 0.025$, is dominated by cavitation surge signatures. The accompanying power spectral density at $\sigma = 0.045$ is seen in Figure 2-7. However, while rotating cavitation and alternate blade cavitation signatures can be inferred from the spectrogram, the spatial harmonic content and direction of rotation cannot be easily discerned from current experimental analysis,



(a) $\phi = 0.082$. For experimental data, error bars are within size of symbol.



(b) Lower flow coefficients. For experimental data, error bars are within size of symbol.

Figure 2-5: Steady cavitating performance of the MIT inducer.

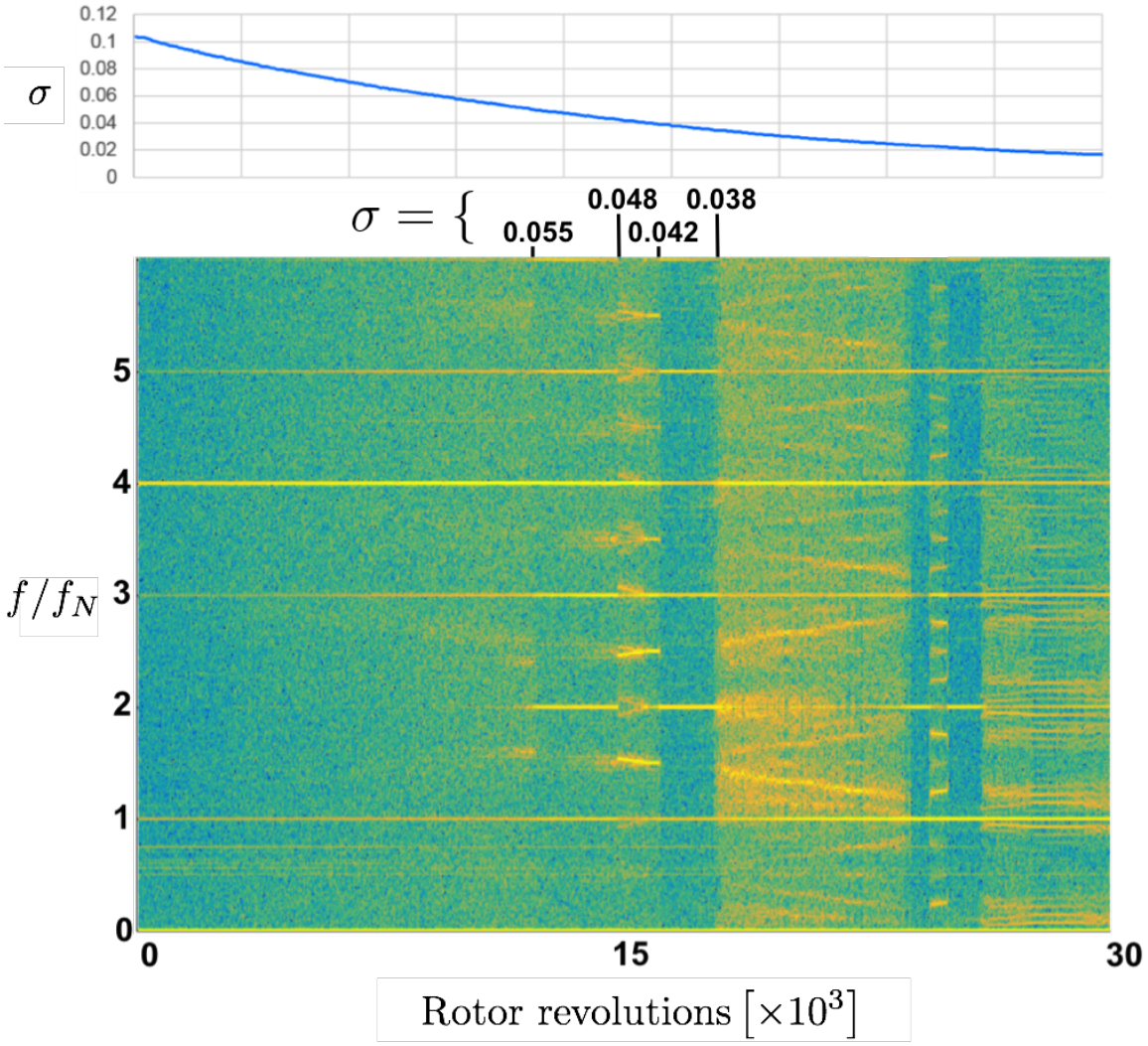


Figure 2-6: Spectrogram of one dynamic pressure transducer at $\phi = 0.083$ showing alternate blade cavitation, rotating cavitation, and surge signatures.

as noted in Section 1.2.1. The Traveling Wave Energy methodology is proposed to address these challenges.

2.5 Traveling Wave Energy Analysis

Typically used for detection of rotating stall and surge instabilities in aero-engine compressors [41–43], the objective of TWE is to determine the direction of rotation and the spatial harmonic content of small-amplitude flow perturbations. TWE is the spectral analysis of spatial Fourier coefficients of unsteady data. The difference in pos-

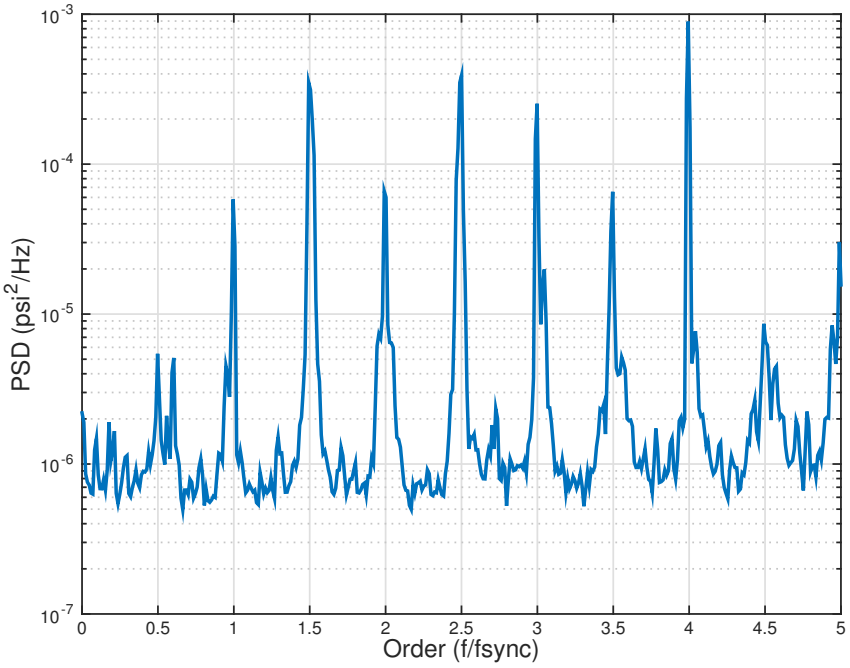


Figure 2-7: Power spectral density of one dynamic pressure transducer at $\phi = 0.083$ and $\sigma = 0.045$ showing a rotating cavitation signature at 1.5N.

itive and negative spectra for a traveling wave, captured in the peaks and valleys of the TWE spectrogram, represent forward and backward rotation of respective spatial harmonic waves [41]. Use of TWE for unsteady pressure data is therefore advantageous over Hannover diagrams due to the explicit definition of rotation direction. In the present work, TWE is applied for the first time to pressure data taken at the leading edge of a cavitating inducer and clarifies the behavior of detected cavitation instabilities.

Rotating cavitation is of long length scale (radius scale) wavelength and occurs in a periodic domain, allowing the measured pressure oscillations to be represented by the sum of spatial harmonic modes, n,

$$p(t,\theta) = \mathrm{Re}\left(\sum_{n=0}^{\infty} \delta p_n(t) \cdot e^{jn\theta}\right) \tag{2.4}$$

where $\delta p_n(t)$ is the n-th harmonic spatial Fourier coefficient. A sketch is seen in Figure 2-8 for $n = 1, 2, 3$ – the sum of all spatial modes yields the pressure signal

at instant t. The 0-th spatial Fourier coefficient is real – non-0-th spatial Fourier coefficients can be written in terms of their real and imaginary parts,

$$\delta p_n(t) = \delta p_{n\text{-Re}}(t) - j \cdot \delta p_{n\text{-Im}}(t). \tag{2.5}$$

Therefore, for m discrete pressure transducers at angular locations θ_j ($j = 1, 2, \ldots, m$), the spatial Fourier coefficients at each instant t can be obtained using a psuedo-inverse discrete Fourier transform by solving

$$\mathbf{p}(\theta, t) = \mathbf{F} \cdot \delta\mathbf{p}(t) \tag{2.6}$$

$$\begin{bmatrix} p(\theta_1, t) \\ p(\theta_2, t) \\ \vdots \\ p(\theta_m, t) \end{bmatrix} = \begin{bmatrix} 1 & \cos\theta_1 & \sin\theta_1 & \cos 2\theta_1 & \sin 2\theta_1 & \cdots & \cos n\theta_1 & \sin n\theta_1 \\ 1 & \cos\theta_2 & \sin\theta_2 & \cos 2\theta_2 & \sin 2\theta_2 & \cdots & \cos n\theta_2 & \sin n\theta_2 \\ \vdots & \vdots & \vdots & \vdots & \vdots & \ddots & \vdots & \vdots \\ 1 & \cos\theta_m & \sin\theta_m & \cos 2\theta_m & \sin 2\theta_m & \cdots & \cos n\theta_m & \sin n\theta_m \end{bmatrix} \begin{bmatrix} \delta p_0(t) \\ \delta p_{1\text{-Re}}(t) \\ \delta p_{1\text{-Im}}(t) \\ \delta p_{2\text{-Re}}(t) \\ \delta p_{2\text{-Im}}(t) \\ \vdots \\ \delta p_{n\text{-Re}}(t) \\ \delta p_{n\text{-Im}}(t) \end{bmatrix} \tag{2.7}$$

through a least squares fit,

$$\delta\mathbf{p}(t) = \left(\mathbf{F}^{\mathrm{T}}\mathbf{F}\right)^{-1} \mathbf{F}^{\mathrm{T}}\mathbf{p}(\theta, t). \tag{2.8}$$

To calculate the n-th spatial Fourier coefficient, m must be greater than $2n$.

Once $\delta\mathbf{p}(t)$ is computed, spectral analysis for the time-varying spatial Fourier coefficients for each spatial harmonic can be conducted. Since the negative and positive frequency spectra differ for a traveling wave (i.e. a standing wave is the sum of a left and a right traveling wave), the spectrum of the TWE can be defined as the difference between the positive and negative frequency spectra. Therefore, peaks and valleys in the TWE spectrogram indicate forward and backward travel of spatial harmonic

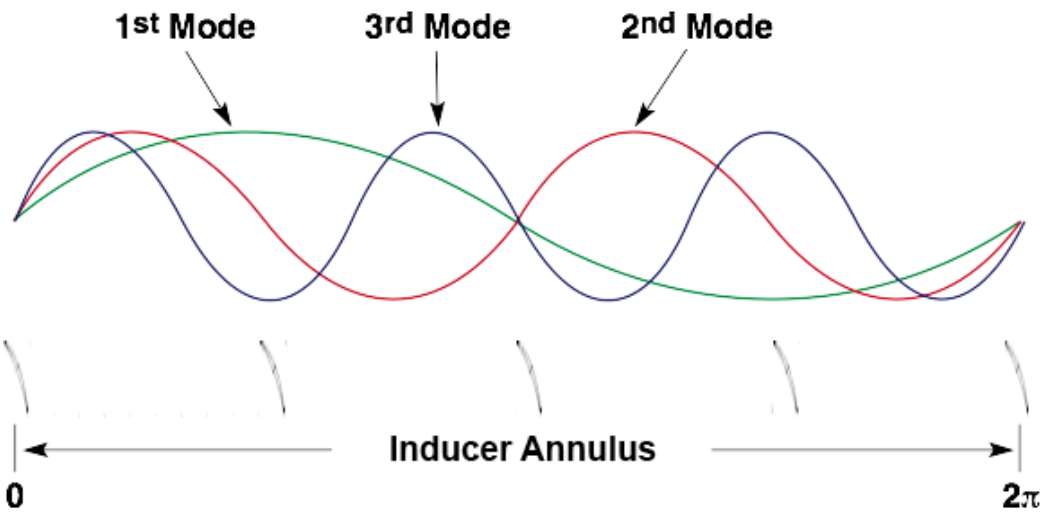


Figure 2-8: Sketch of spatial harmonic modes for $n = 1, 2, 3$ for one instant in time – the sum of all spatial modes yields the pressure signal.

waves, explicitly defining direction of rotation.

Traveling wave energy analysis allows the determination of frequency, spatial mode shape, and direction of rotation of natural oscillatory modes. The key advantages of TWE are its extraction of spatial mode shape and direction of rotation; no spatial mode information is able to be deduced from standard spectral analysis of cavitating inducer data (as demonstrated in Figures 2-6 and 2-7, and the rotation direction obtained from Hannover analysis is ambiguous due to the requirement to assume a reference direction.

2.6 Traveling Wave Energy Analysis of Unsteady Pressure Data

TWE analysis was conducted on the pressure data taken during the ramp test described in Section 2.4. The analysis yields rotating cavitation signatures in the first spatial harmonic and alternate blade cavitation signatures in the second spatial harmonic, aligning with expected mode shapes of both cavitation instabilities.

Figure 2-9 shows the first spatial harmonic TWE spectrogram for $\sigma = 0.045$-0.035. Forward rotating cavitation signatures are seen at 1.5 times rotor frequency, while,

notably, a backward rotating signature is seen at 2.5N. A backward traveling component to rotating cavitation was predicted by Tsujimoto in [26], with comments made towards the difficulty in its experimental detection in [14]. For the same time window (and therefore cavitation numbers), the second spatial harmonic TWE is seen in Figure 2-10, showing 2N alternate blade cavitation activity.

The frequencies seen using TWE correspond with the signatures seen in Figures 2-6 and 2-7. The spatial mode shapes correlate with the number of cavities – for alternate blade cavitation in a four bladed inducer, there are two cavities attached to alternate blades that rotate synchronously, while for rotating cavitation, there is one larger cavity that spans approximately three passages, rotating faster than shaft speed. Moreover, the comparison of Figures 2-9 and 2-10, seen in Figure 2-11, shows a clear cut-on/cut-off behavior between rotating cavitation and alternate blade cavitation. This strongly supports the hypothesized rotating cavitation onset mechanism described in Section 1.1.2.

2.7 Traveling Wave Energy Analysis of High Speed Video Data

As described in Sections 2.5 and 2.6, the input for TWE analysis is typically unsteady data from a number of pressure transducers and the number of sensors in use is directly related to the number of spatial harmonics that can be resolved through TWE analysis. This thesis proposes an adaptation of TWE to video data. Each pixel in a video frame can be treated as a sensor; in the case of black and white video, each pixel tracks grayscale intensity in 8-bit integers (i.e. 0 to 255), akin to pressure transducers that track electrical signals. After suitable data reduction, TWE is used to quantitatively assess and corroborate cavitation behavior as seen in frontal-view optical measurements against pressure measurements. The results indicate cavitation behavior is dominated by circumferential wave patterns, suggesting that pressure transducers can be established as the primary detection of cavitation behavior and

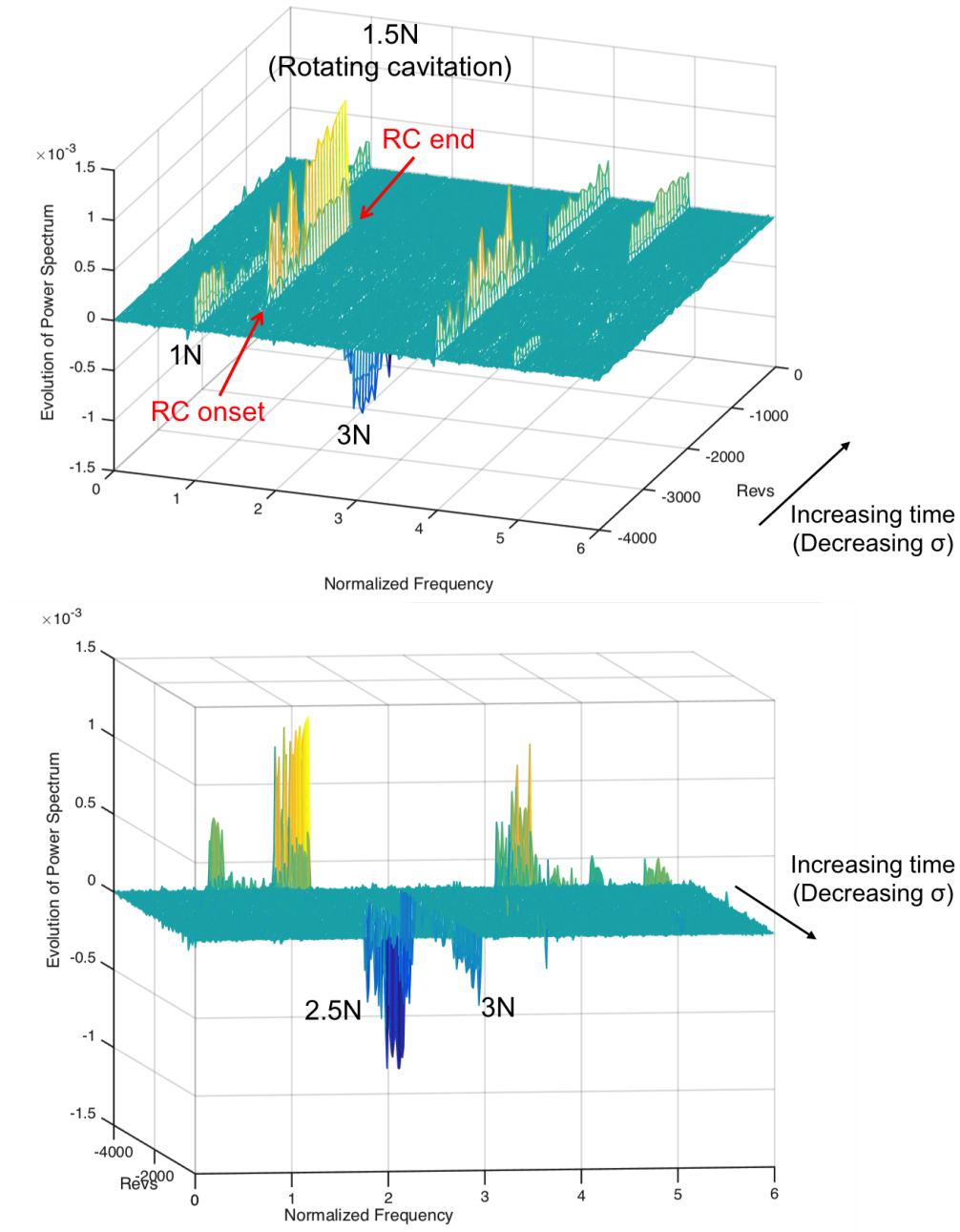


Figure 2-9: First harmonic TWE spectrogram for $\sigma = 0.045$-0.035, showing rotating cavitation signatures: forward rotating at 1.5N and backwards rotating at 2.5N.

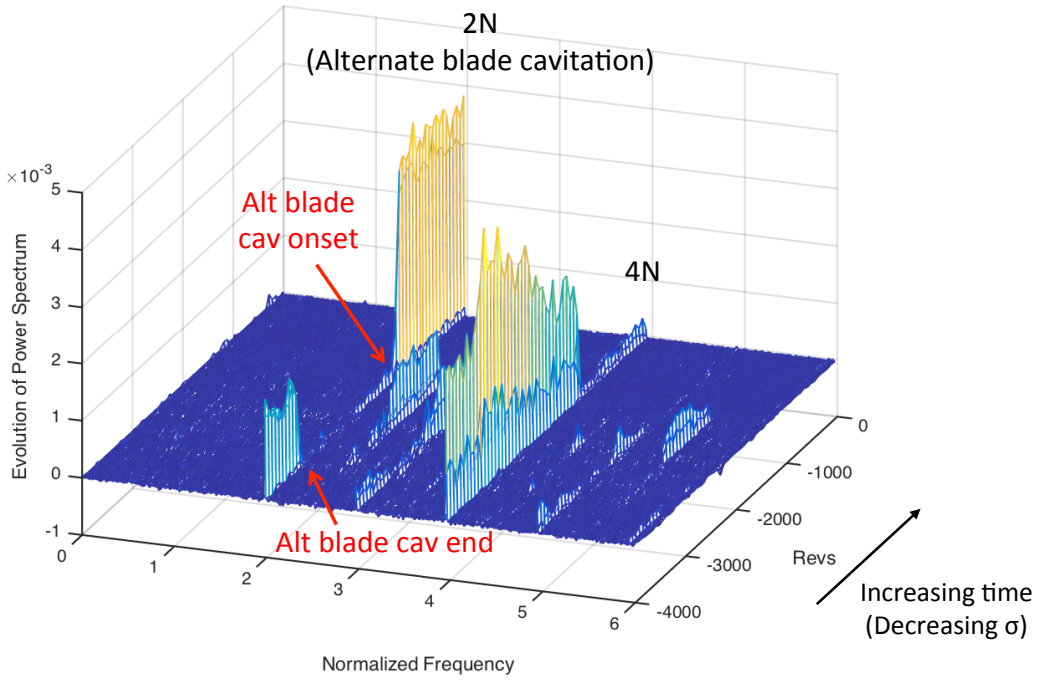


Figure 2-10: Second harmonic TWE spectrogram for $\sigma = 0.045$-0.035, showing alternate blade cavitation signatures.

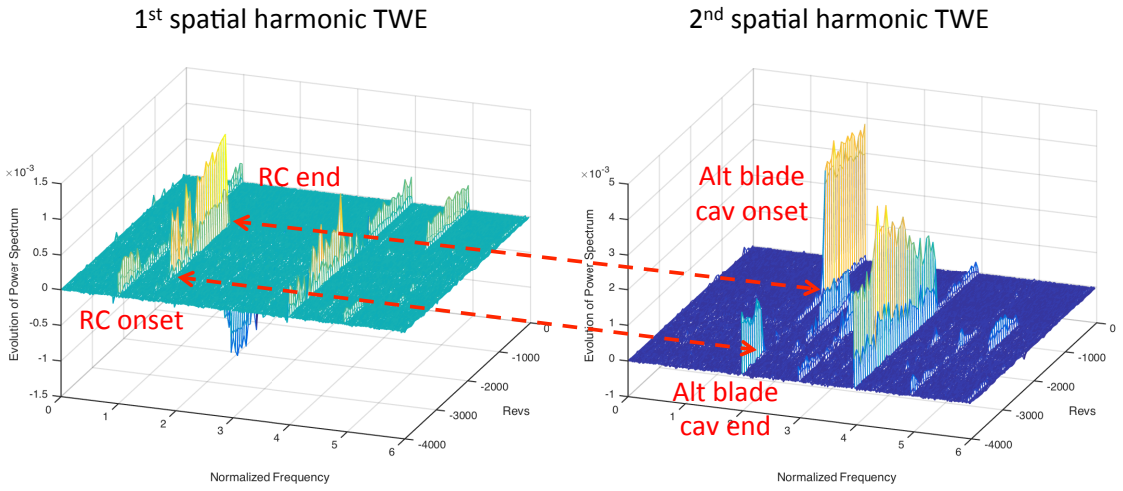


Figure 2-11: Cut-on/cut-off behavior between rotating cavitation and alternate blade cavitation, consistent with the rotating cavitation onset hypothesis described in Section 1.1.2.

thereby considerably simplifying experimental setups.

Two test entries with high speed video were conducted using the optical access capabilities of Aerospace Corporation's facility. One test entry focused on side-view video and the other recorded frontal-view videos using a borescope. The side-view videos were primarily used to experimentally investigate tip vortex trajectory – videos of tip vortex trajectories at different flow coefficients were compared against single-phase simulations, verifying the presence of tangential tip vortices at $\phi = 0.082$, where rotating cavitation is present; details can be found in [12]. The data from the second video test entry, frontal-view borescope videos, was used for TWE.

2.7.1 Frontal-View Video Experimental Setup

The experimental setup for the frontal-view videos is seen in Figure 2-12. The camera used was a Photron FASTCAM Mini AX200, affixed to a custom borescope manufactured by Cortek Endoscopy using a C-mount-to-DIN-eyepiece coupler that enabled a 90° direction of view for the camera. The borescope was positioned approximately twenty borescope diameters upstream of the inducer. The primary illumination element, seen on the right in Figure 2-12, was a twenty-four-element LED array from Visual Instrumentation, diffused through two layers of paper to reduce glare. Six three-element LED spotlights from Visual Instrumentation were also distributed around the optical section to provide even lighting.

The custom borescope is shown in Figure 2-13, along with a diagram depicting the included light source. For use in the Aerospace Corporation facility, the borescope was sealed internally such that no air could enter the facility from the borescope. The field of view out of the borescope was 64°, selected to be large enough such that no part of the inducer would be clipped by the borescope. Notably, the borescope accepts an external light source via the light post affixed near the eyepiece, directing the light in the same direction as the view.

A precise combination of lighting, camera aperture, camera shutter speed, and borescope configuration were required to produce acceptable video of the cavitating inducer. Sealant was applied to interfaces between the borescope, camera, and test

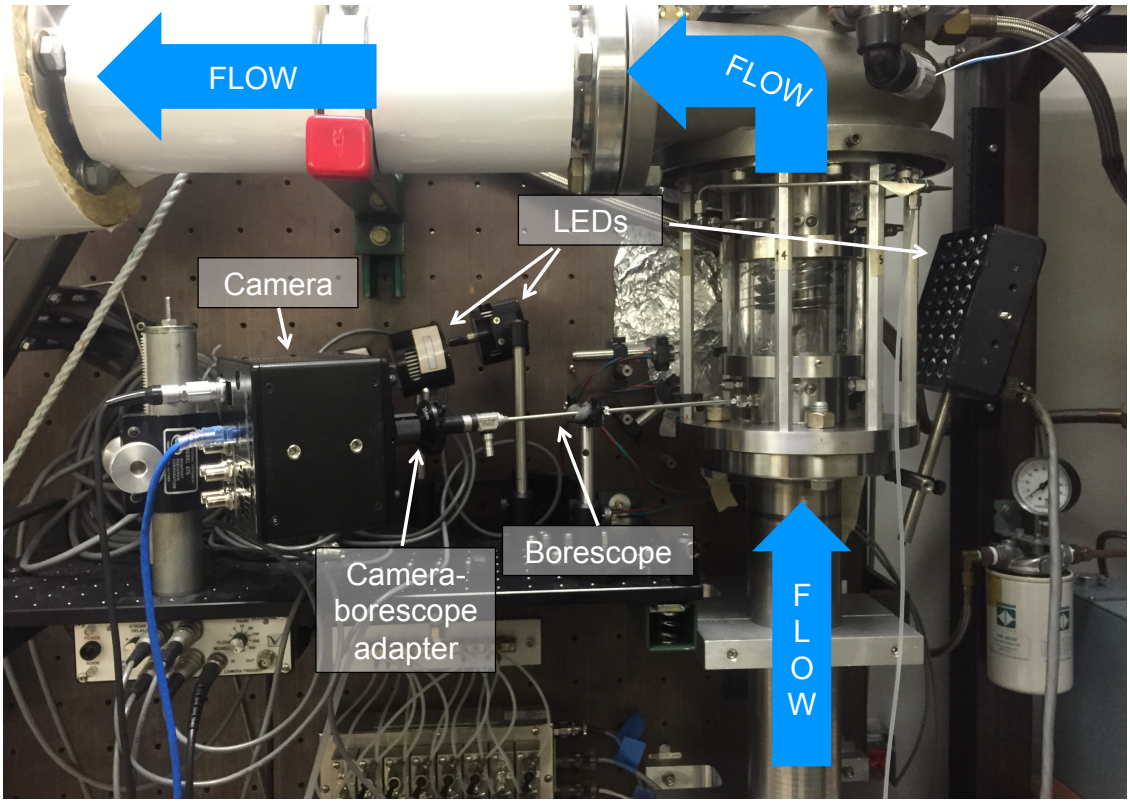


Figure 2-12: Experimental setup for frontal-view borescope videos. Note that the actual lighting setup is not depicted – LEDs were distributed evenly around the optical section.



Figure 2-13: Custom borescope manufactured by Cortek Endoscopy.

section to prevent leaks from increasing the DO within the facility. An external light source was coupled to the borescope, but eventually removed due to the glare off of the metal of inducer causing uneven lighting; a matte black test inducer would alleviate this issue. Videos were grayscale and taken at 3000 frames per second with a 331 microsecond shutter speed at a resolution of 512×512 pixels. The inducer rotated at 4000 RPM, yielding 45 frames per revolution. A number of zoom lenses were tested in an effort to fill the entire sensor with the borescope image, but it was found that the lenses reduced the light entering the camera to an unacceptable degree.

Cavitation numbers targeting tip vortex cavitation, alternate blade cavitation, and rotating cavitation regimes were selected, as well as ramp test transients for image spectral analysis.

2.7.2 Frontal-View Traveling Wave Energy Analysis

To adapt video for TWE analysis, a data reduction scheme was conducted, outlined in Figure 2-14. For each video frame:

1. Calibrate borescope video, identifying inducer center, inner radius, and outer radius.

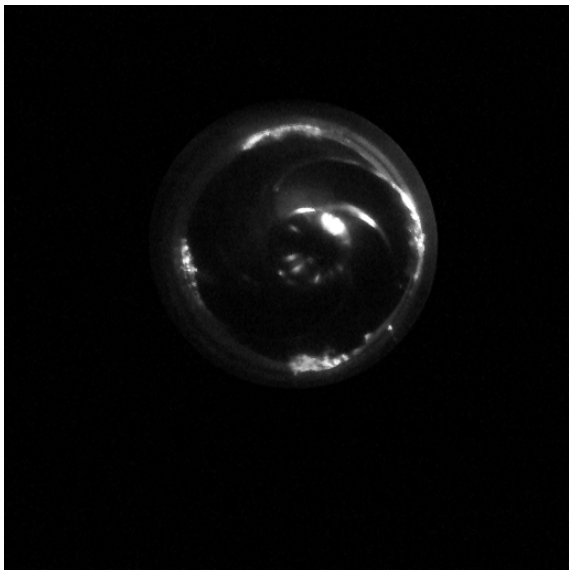
2. Unwrap circular video – transform from polar to Cartesian coordinate system for simpler spatial fast Fourier transform.

3. Radially average across cavitation region, obtaining average grayscale intensity as a function of angular location.

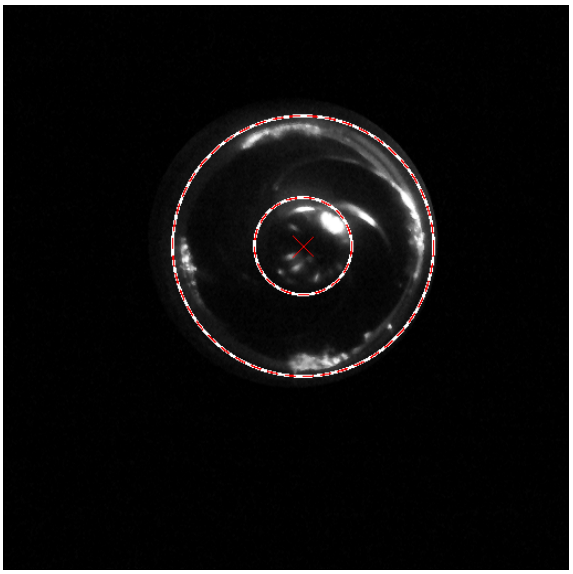
The result is time varying data of grayscale intensity, where each "sensor" is each angular location's average intensity.

To investigate the impact of averaging extent, a parametric study was completed. The averaging extent was radially varied in increments of 5% from 5% span to 60% span, all referenced from the tip. TWE analysis was conducted for each of the twelve cases and the frequency content was examined. It was found that there was less than 2% change in frequency content when comparing across all tested cases. Magnitudes scaled across each spectrogram depending on averaging extent, showing strongest signatures when averaging across 30% to 40% span. The conclusion was that averaging extent had very little impact on the TWE results, and a 35% span was selected for the baseline averaging extent. Furthermore, this suggests that circumferential length scales are dominant in dynamic cavitation behavior.

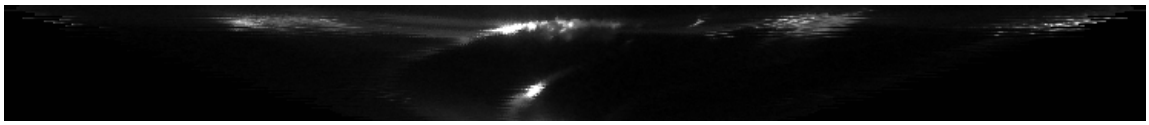
In the case of a discrete number of pressure transducers, as in Section 2.5, for resolution of the n-th spatial harmonic, $2n$ pressure transducers must be used. However, in the case of the borescope video after data reduction (Figure 2-14d), the pixels offer



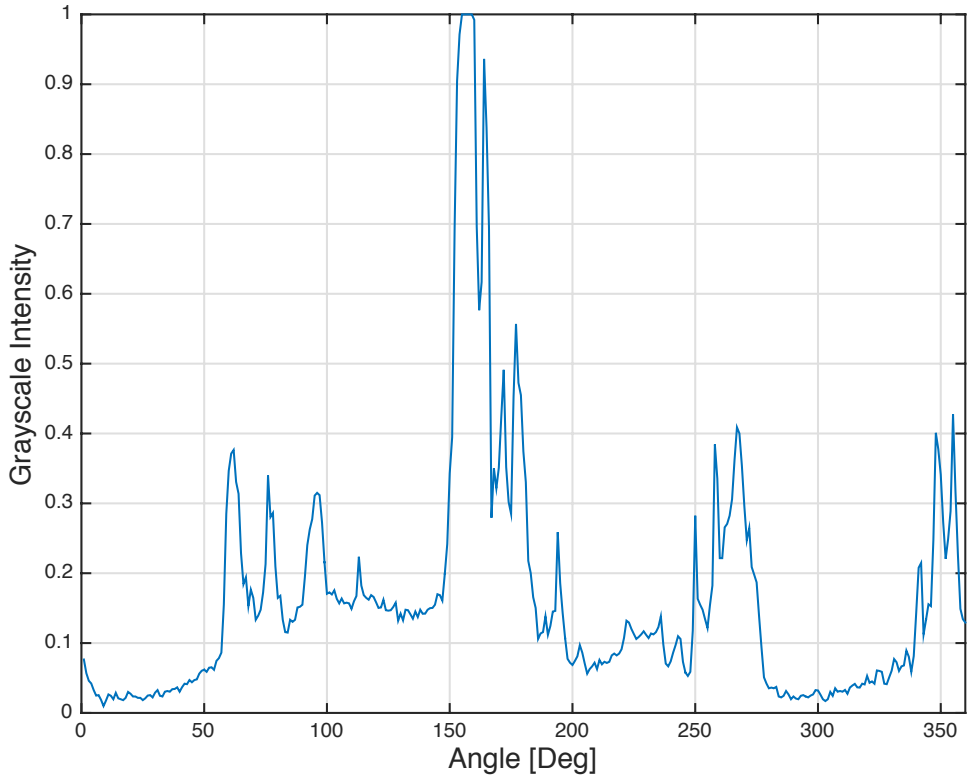
(a) Unprocessed frame



(b) Calibrated frame with inducer center, inner radius, and outer radius identified

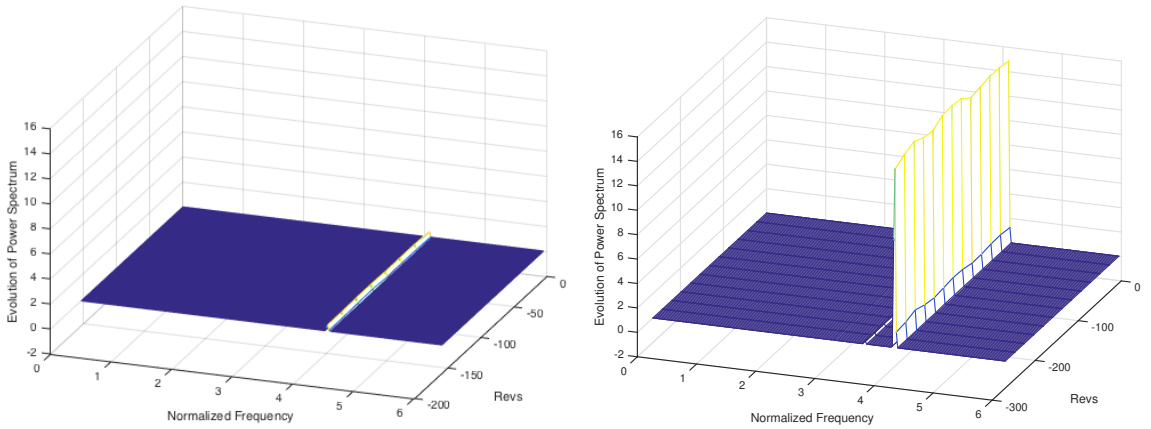


(c) "Unwrapped" frame



(d) Averaged grayscale intensity over cavitation region as a function of circumferential angle

Figure 2-14: Data reduction for video TWE.



(a) Video taken at fully wetted conditions (b) Video taken at $\sigma = 0.1$

Figure 2-15: Validation test case for video TWE showing 4N activity in the fourth spatial harmonic due to cavitating tip vortices.

an "infinite" number of sensors and may be treated as a contiuum. Practically, this implies an inverse fast Fourier transform can be directly used in lieu of Equations 2.6, 2.7, and 2.8, and, furthermore, a higher number of spatial harmonics can be resolved.

Video of the inducer with cavitating tip vortices was selected as a validation test case – a frame of video is used as the example in Figure 2-14. At higher cavitation numbers, only the low pressure cores of the tip vortices are cavitating. In a four bladed inducer with four tip vortices, the expected spectral activity is therefore in the fourth spatial harmonic at four times shaft speed. The video TWE results for the inducer at fully wetted conditions (i.e. no cavitation) and for the inducer at $\sigma = 0.1$ with tip vortex cavitation are compared in Figure 2-15. The cavitating case clearly shows the expected 4N signature while there is almost no activity in the wetted case, indicating the viability of the TWE approach for optical measurements.

Videos of alternate blade cavitation and rotating cavitation, frames of which are shown in Figures 2-16 and 2-17, respectively, were then analyzed using TWE. The results for rotating cavitation are seen in Figure 2-18. Strong 1.6N signatures are seen in the first spatial harmonic, accompanied by little activity in the second spatial harmonic, expected behavior for rotating cavitation. For TWE of alternate blade cavitation video, seen in Figure 2-19, spectral activity is dominated by the 2N signature in the second spatial harmonic, again corroborating with expected behavior.

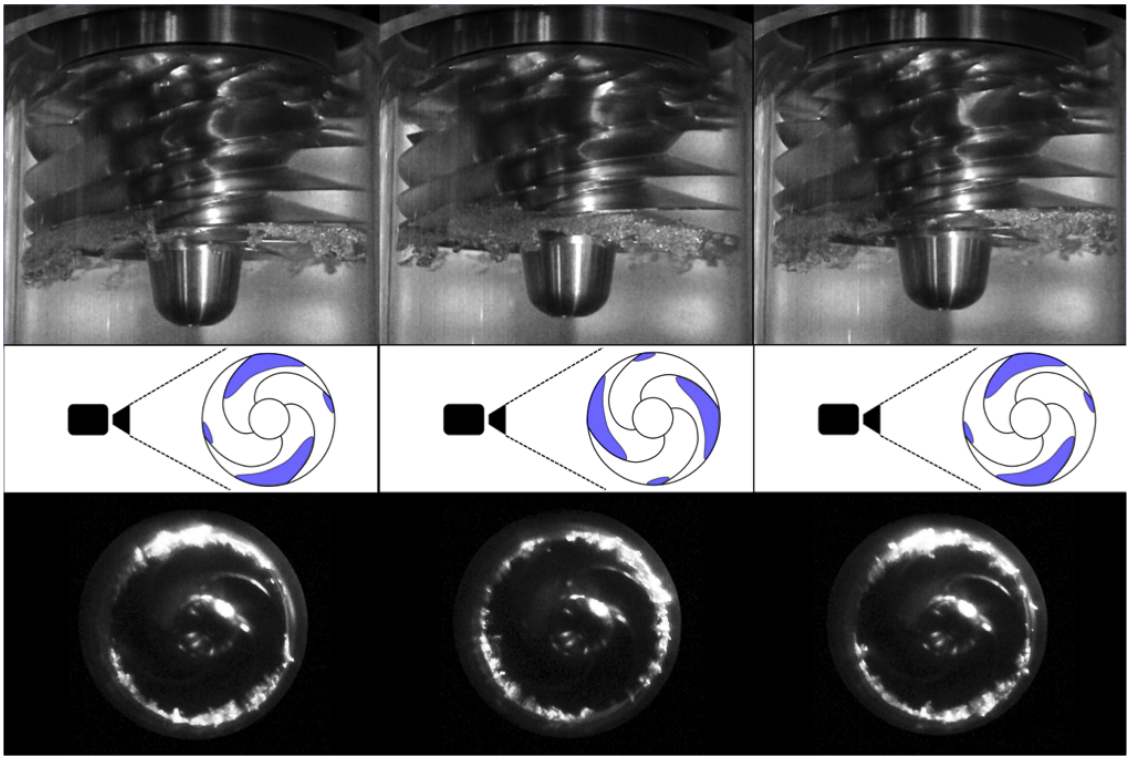


Figure 2-16: Side-view and frontal-view video frames showing alternate blade cavitation at $\phi = 0.082$ [12].

A transient ramp test video was also processed using TWE analysis, the results of which are seen in Figure 2-20. The end of rotating cavitation activity at 1.6N in the first spatial harmonic coincides with the beginning of 2N alternate blade cavity signatures in the second spatial harmonic, reflecting the behavior seen from pressure measurements in Figure 2-11.

2.7.3 Fourier Analysis of Frontal-View Cavitating Inducer Video

As described in Section 1.2.1, little quantitative analysis has been done for cavitating inducer videos. Cervone [24] used image processing algorithms to obtain tip cavity lengths from frontal-view video as a function of time and used Fourier analysis to recover rotating stall frequencies also obtained from pressure data. Based on Cervone's work, a similar method was used to analyze frontal-view video of the MIT inducer. Cavitation area was obtained as a function of time through the Sobel edge detection method [44] and a fast Fourier transform was taken to extract frequency content.

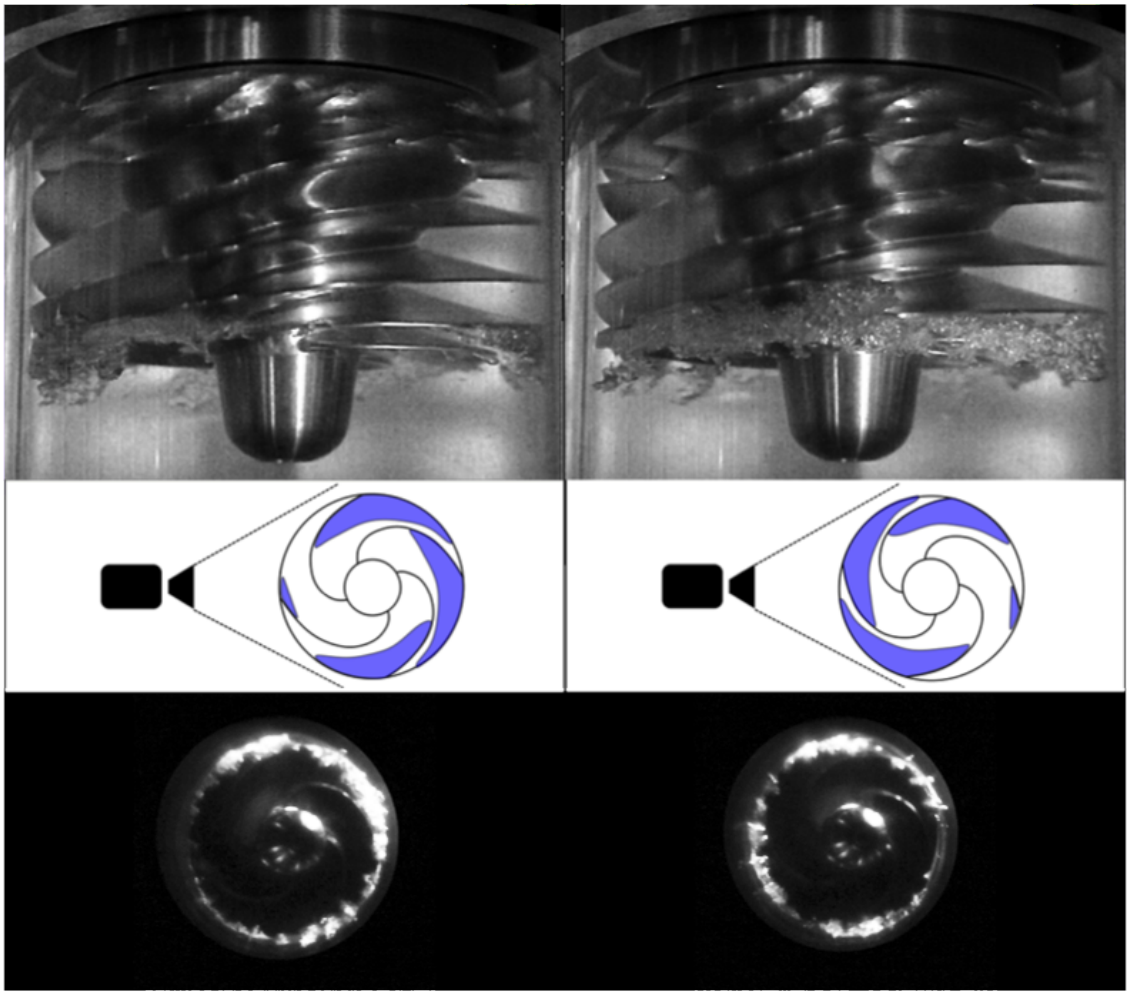


Figure 2-17: Side-view and frontal-view video frames showing rotating cavitation at $\phi = 0.082$ [12].

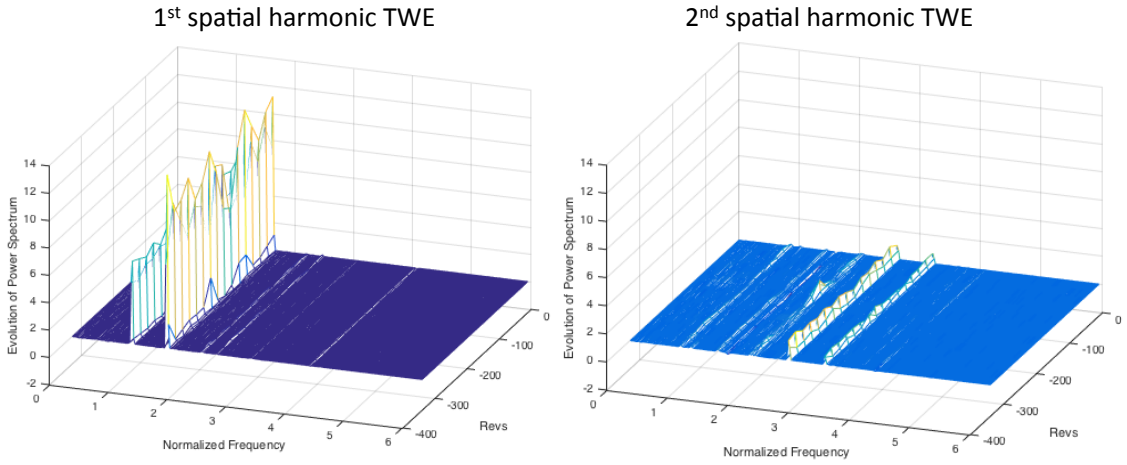


Figure 2-18: TWE results for video of rotating cavitation, showing 1.6N signatures in the first spatial harmonic and low activity in the second spatial harmonic, corresponding with Figure 2-9.

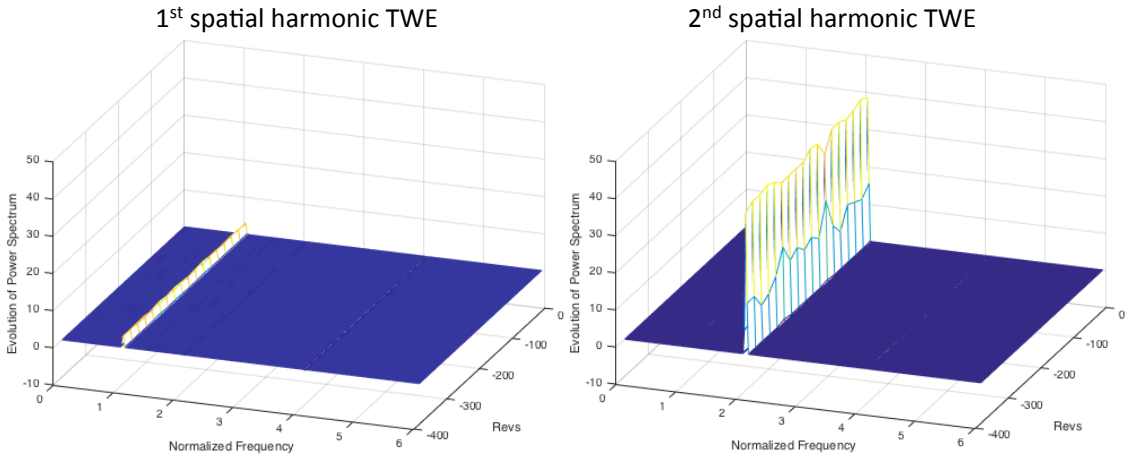


Figure 2-19: TWE results for video of alternate blade cavitation, showing low activity in the first spatial harmonic and strong activity at 2N in the second spatial harmonic, corresponding with Figure 2-10.

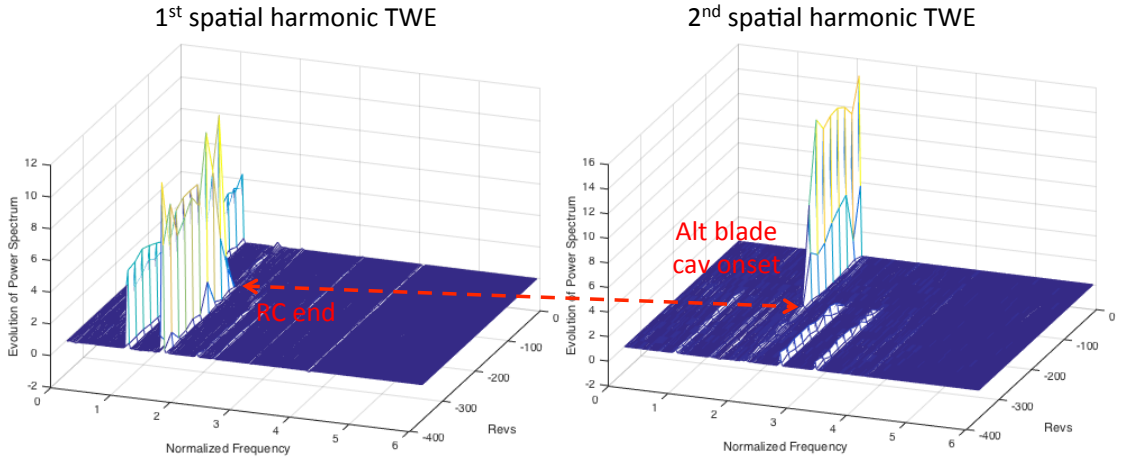


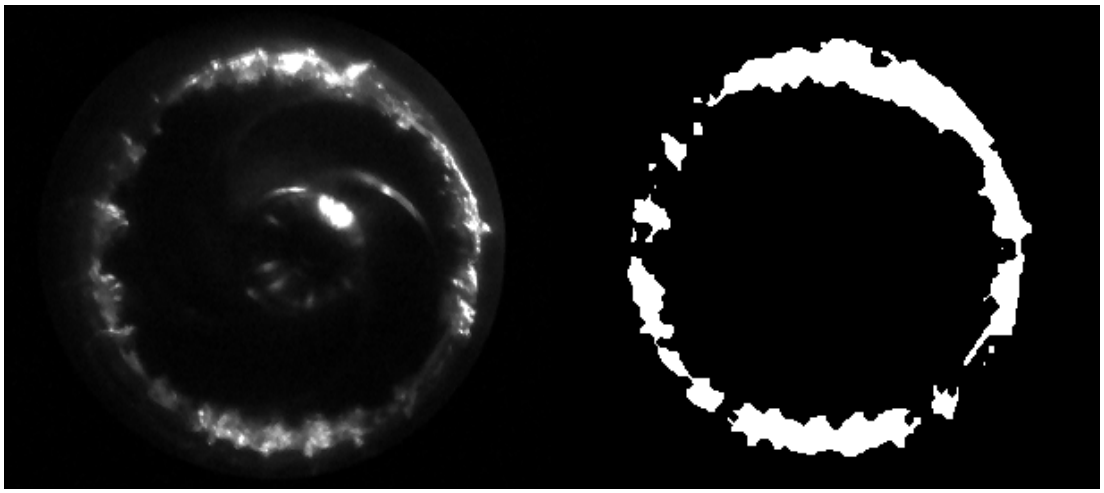
Figure 2-20: TWE results for transient ramp test video, consistent with unsteady pressure measurements (Figure 2-11).

The same rotating cavitation video from Figure 2-18 was used as an example case. A frame from the video is seen in Figure 2-21a alongside the detected cavitation area. After edge detection, the frame becomes a binary image where white represents cavitation and black filters out the rest of the frame. The entire video is processed frame-by-frame, extracting the amount of cavitation area from each frame, resulting in cavitation area as a function of time, seen in Figure 2-21b. An FFT was then taken, resulting in Figure 2-21c. The FFT shows signatures at 1.6N, similar to Figure 2-18. However, spatial data is not captured in the FFT – it is difficult to confirm if the result is indeed rotating cavitation activity without knowledge thereof a priori. Furthermore, the same image processing was conducted for the transient ramp test video processed in Figure 2-20 and the results are seen in Figure 2-22. There is little rotating cavitation or alternate blade cavitation activity seen in the spectrum while TWE is clearly able to capture the change between the two instabilities. TWE is able to extract more information than current quantitative analysis methods for video data of cavitating inducers.

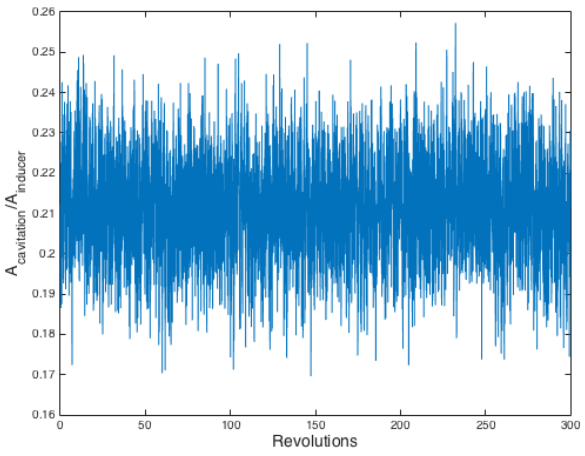
2.7.4 Characterization of Dynamic Cavitation Behavior Regimes Using Video TWE

The recovery of the expected spatial harmonic content and frequencies of cavitation instabilities confirm the validity of the TWE approach for optical data analysis. All steady operating point videos taken were analyzed and the specific cavitation instability present was deduced using TWE. The results are plotted on a head fall-off curve in Figure 2-23, comparing the video TWE results against pressure data results from Sections 2.4 and 2.6 and indicate good qualitative agreement.

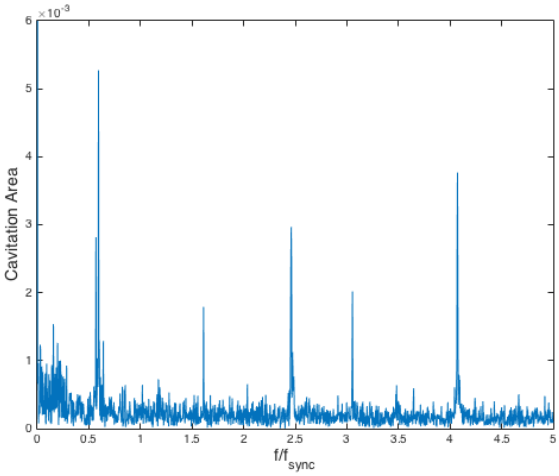
Due to limitations in the experimental setup, the exact cavitation numbers corresponding to each video were not able to be synced. To acquire the low speed performance data and operating conditions attributed to each borescope video, measurements were recorded off of the LabVIEW front panel as the videos were taken, introducing uncertainty. An improvement in the experiment would be to use the



(a) Comparison of original video frame and detected cavitation area; white indicates cavitation



(b) Cavitation area as a function of time



(c) FFT of cavitation area

Figure 2-21: Rotating cavitation video analysis following Cervone's quantitative method [24], showing 1.6N activity, but lacking spatial mode detection.

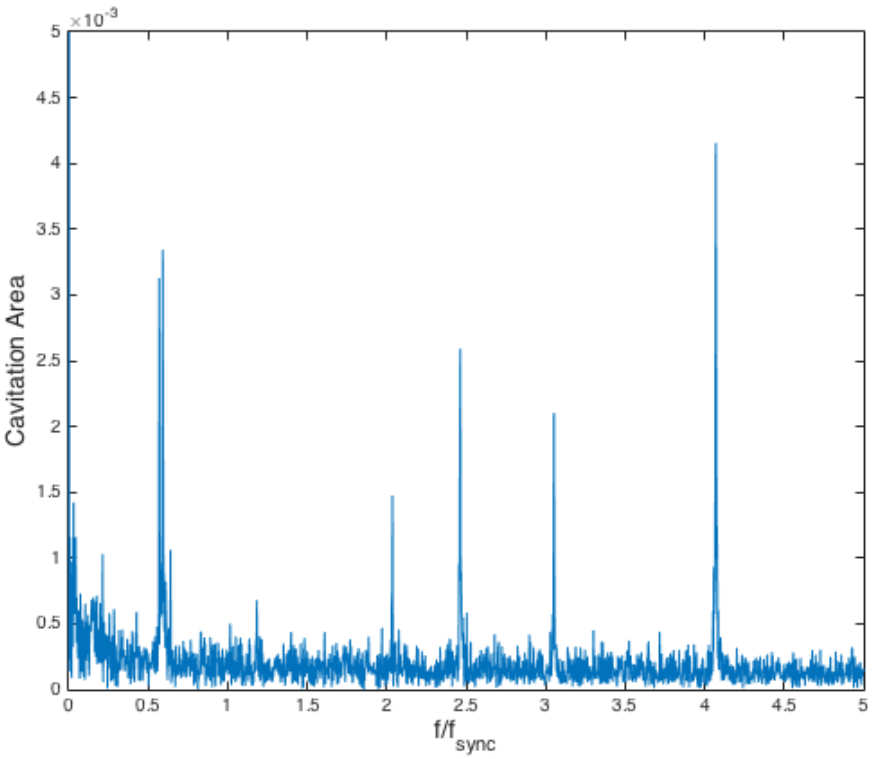


Figure 2-22: FFT of ramp test video – compare with Figure 2-20, note the lack of activity seen in FFT.

trigger capabilities on the Photron camera to sync data recording as video recordings begin and end. Additionally, the optical access section used did not allow simultaneous pressure measurements at the inlet plane. Drilling taps into the optical section and mounting the pressure transducer array would allow direct comparison between video and pressure TWE, removing any uncertainty about video TWE results.

2.8 Summary and Conclusions

Rotating cavitation and alternate blade cavitation were experimentally characterized using the traveling wave energy methodology for the first time. TWE of pressure data indicated a clear cut-on/cut-off behavior between the two cavitation instabilities, supporting the hypothesis from Section 1.1.2. Adaptation of TWE to frontal-view high speed video recovered expected cavitation instability signatures and qualitatively correlated with pressure data results, thereby indicating video TWE as a viable ex-

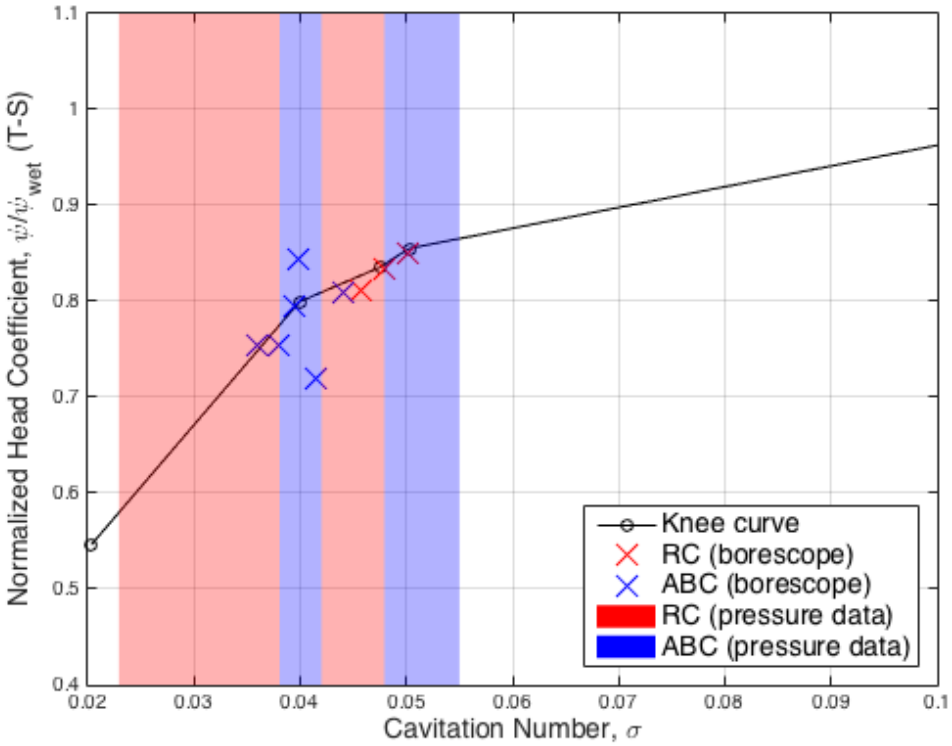


Figure 2-23: Qualitative agreement between pressure and video TWE analysis. Discrepancies likely caused by uncertainty in cavitation number measurement.

perimental analysis tool for cavitation instabilities. Video TWE is also seen to extract more information than current quantitative methods for high speed video analysis.

Notably, the correlation of video and pressure results combined with the results of the parametric study of radial averaging extent suggest that rotating cavitation and alternate blade cavitation are governed by circumferential wave patterns. This again supports the rotating cavitation onset hypothesis – radial activity does not seem to play a role in rotating cavitation inception. Additionally, it also suggests that pressure measurements can be established as the primary detection method for cavitation behavior, thereby significantly simplifying experimental setups. The equipment required for borescope high speed videos is considerably more expensive than dynamic pressure transducers for inlet plane measurements, as well as more difficult to setup and configure, based on experience gained during the three test entries at Aerospace Corporation.

Chapter 3

A Review of Body Force Models for Turbomachinery Applications

An adaptation of the body force modeling methodology is proposed for rotating cavitation modeling to address the current challenges and limitations outlined in Section 1.2.2. However, legacy body force models, successfully used for aeronautics-related problems, applied to the inducer were deemed unviable due to the formation of spurious recirculation regions. Investigations support the hypothesis that narrow rotor loss buckets, which are a consequence of the low flow coefficient design of the inducer, are the root cause of model sensitivity.

3.1 Body Force Modeling of Turbomachinery

Successful uses of body force modeling include the investigation of fan/inlet coupling and distortion transfer in short nacelle inlets [36], compressor stability prediction [34], and assessment of fan shock noise in serpentine inlets with boundary layer ingestion [35]. The concept behind body force modeling, sketched in Figure 3-1, is the representation of the turbomachinery blade rows as body force field distributions that capture the same stagnation pressure rise and flow turning. The model defines the causal link between the desired flow field and the required force distribution without having to consider blade geometry; the elimination of the discrete blades in the simu-

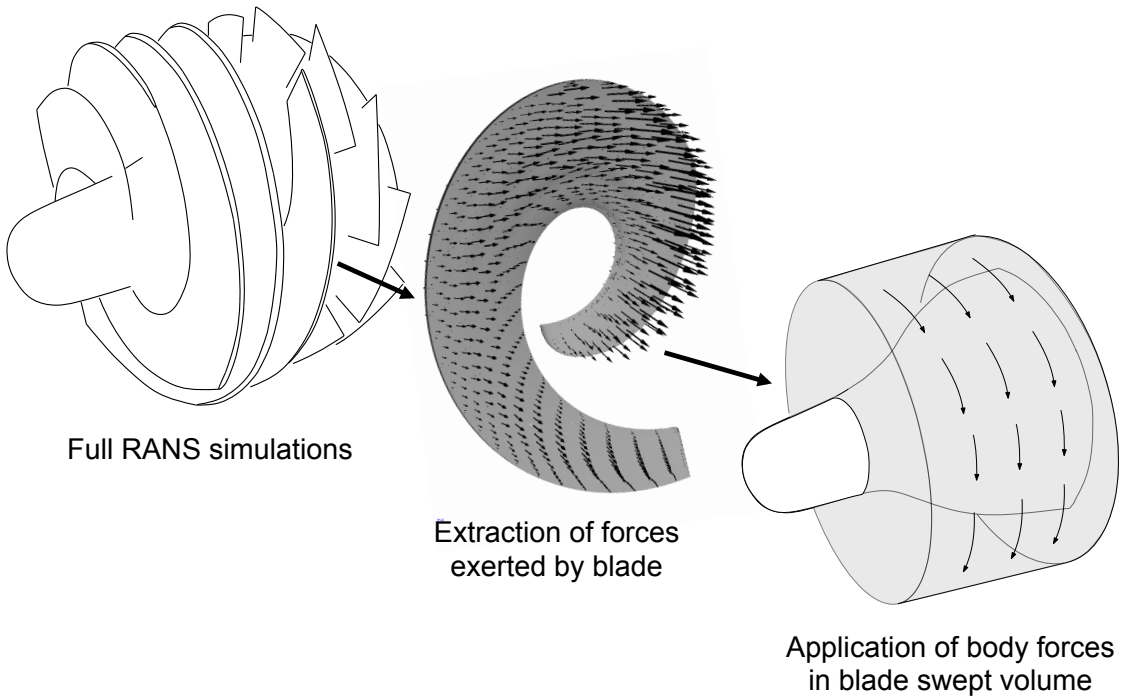


Figure 3-1: Conceptual steps in body force modeling.

lation also considerably simplifies the mesh and reduces the associated computational cost. The potential use of body force modeling in the context of designing inducers is twofold. The impact of specific inducer geometries on cavitation instability behavior could be assessed through adjustment of an empirical correlation within the model. Alternatively, the necessary force field to suppress rotating cavitation could be used to define a preferred inducer geometry and/or casing treatment.

Marble [45] was the first to suggest the body force approach as a throughflow method to model a blade row. The primary assumption is axisymmetric flow, where the flow through the blade row is modeled as an infinite number of infinitely-thin blades within the same swept volume – the flow field is therefore equivalent to the pitchwise average of the full three-dimensional flow. The effects of the blades are captured through body force source terms added to the momentum and energy equations. Marble derived thermodynamic relations connecting the body forces to enthalpy change and entropy generation within the blade row, consisting of two components – the normal force, which represents flow turning, and the parallel force, which represents viscous losses.

A number of approaches to define the link between the forces and local flow field, known as the blade passage model, have been previously formulated. A summary of relevant advancements in body force modeling is presented here – a more complete account may be found in [36] and [46].

Gong [47] developed a blade passage model to investigate compressor rotating stall and inlet fan distortion. Through an empirical term obtained through experiments and correlations that links the model to the geometry, Gong's model is able to respond to flow field perturbations. Peters [36] improved Gong's model by incorporating off-design losses into the parallel force, adding a radial force to account for blade lean, and using RANS calculations to define a distribution of empirical term instead of a single parameter used throughout the blade domain. Peters used his model to explore the design space for short nacelle inlets for low pressure ratio, high-bypass ratio turbofans. Gong and Peters' models offer advantages over actuator disk models, allowing the capture of the dynamic blade row response and flow redistribution in the blade domain. The models are also able to transfer inlet stagnation temperature and pressure distortions through the turbomachine, as well as capture compressible effects, e.g. shocks.

Benneke [34] defined force look-up tables from RANS calculations at different operating points with local flow parameters as inputs. Used to investigate the stability limit of centrifugal compressors, Benneke's model was able to identify stall precursors that qualitatively agreed with experimental unsteady pressure data.

Brand [46] and Kottapalli [48] formulated a blade passage model that improved upon Gong's model by correcting several limitations. The improved blade passage model is able to capture local relative streamline curvature, accounts for blade metal blockage, and offers physical interpretations of the empirical parameters within the model. The model was applied to calculate axial compressor (Brand) and centrifugal compressor (Kottapalli) performance at off-design conditions.

Sorensen [37], using a similar blade passage model as Brand and Kottapalli, for the first time applied the body force modeling methodology to turbopump inducers. To account for the strong radial flows seen in the inducer flow field, a binormal force is

added to the model along with a dependence on pitch angle. In addition, a preliminary two-phase model was formulated to account for blockage from cavitation. However, the model experienced convergence issues for single-phase calculations, resulting in spurious recirculation regions throughout the calculation domain.

The focus of the present work is to investigate the convergence issues seen in the blade passage model by Sorensen. Based on diagnostic tests, it is hypothesized that the stagnation pressure loss in the inducer is sensitive to changes in incidence, stemming from the inducer's low coefficient design, which manifests in the body force model as model sensitivity.

3.2 Model Overview and Assumptions

The key assumption in body force modeling is the representation of a blade row as an infinite number of infinitely thin blades, which implies that the modeled flow field is the pitchwise-average of the flow field through the three-dimensional blade row. The primary objective of body force modeling is therefore to reproduce the same pitchwise-averaged flow turning, enthalpy change, and entropy generation as the full three-dimensional turbomachine by replacing the blade rows with a body force field, as sketched in Figure 3-2. The body forces are applied as source terms to the momentum and energy equations along with a mass source term in the continuity equation to account for blockage caused by the presence of the blades. The reduced order model must be able to capture the response of the pitchwise-averaged flow field to perturbations.

The model consequently consists of two components. The force extraction process calculates the blade forces necessary to capture the pitchwise-averaged flow field. The second element, termed the blade passage model, provides the link between the forces and local flow field, therefore determining how the forces respond to perturbations.

In the case of a liquid oxygen turbopump inducer, the flow is assumed quasi-steady, incompressible, and inviscid, with the viscous effects captured by the body force field. The flow is also assumed to have no heat sources within the domain and

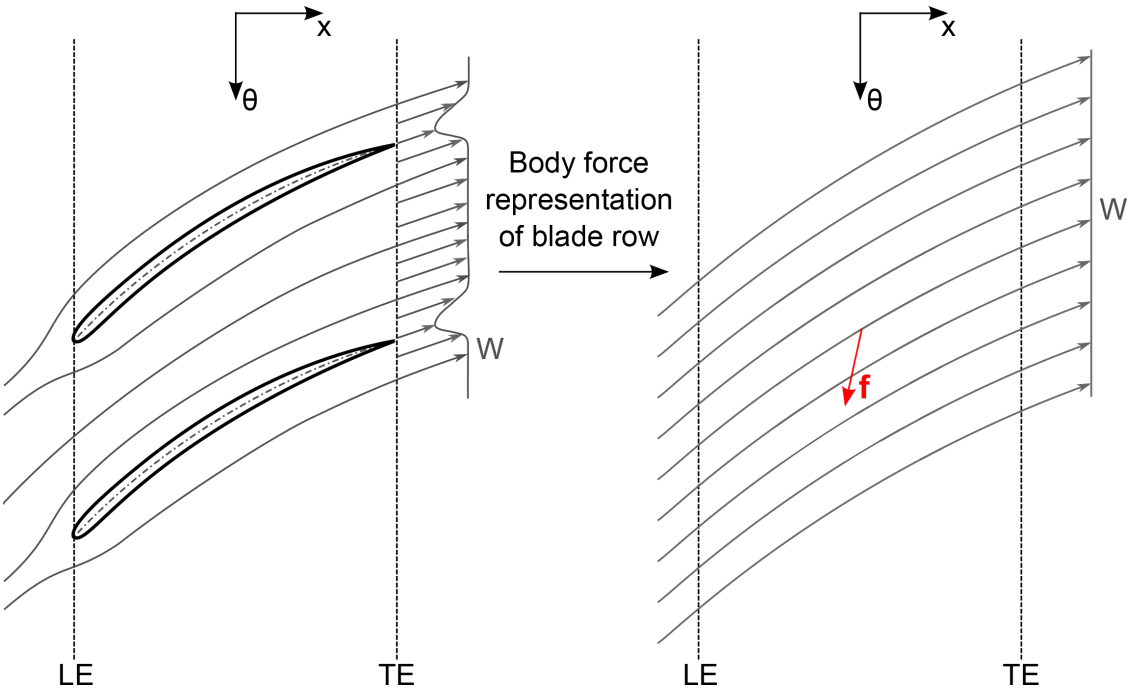


Figure 3-2: Body force modeling infinite blades assumption – "smeared out" representation of blade row [36].

adiabatic boundaries.

3.3 Blade Force Average Force Extraction

A number of methods have been used to calculate the required body force field. One approach extracts and averages the blade surface pressures from single-passage RANS simulations over the blade passages [36, 46, 48]. Another approach conducts control volume analysis for each blade row at different operating points to calculate the forces, also based on single-passage RANS [34]. Sorensen [37] introduced a force extraction method based on the higher order terms from pitchwise averaging the momentum equations; this method, the so-called blade force average, is used in the present work.

The formulation is based in the natural coordinate system, aligned with the streamlines in the rotating frame and consisting of three orthogonal components, l, n, and h. The orientation of the natural coordinate system relative to the stationary frame is seen in Figure 3-3. Two planes are defined, the meridional (axial-radial) plane and a stream surface, which is tangent to the meridional projection of the

streamlines and orthogonal to the meridional plane. On the stream surface, l is in the streamwise direction while n is normal to the streamline. h, termed the binormal direction, is perpendicular to the parallel and normal directions (and therefore normal to the stream surface).

Two angles are defined, the relative flow angle and the pitch angle. The relative flow angle, β, is the angle between the relative streamline and the meridional direction,

$$\beta = \arctan\left(\frac{u_\theta - \Omega r}{\sqrt{u_x^2 + u_r^2}}\right), \tag{3.1}$$

where $\mathbf{u}$ refers to absolute velocities and Ω is the inducer rotational speed. The pitch angle, φ, is the angle between the binormal and axial directions,

$$\varphi = \arctan\left(\frac{u_r}{u_x}\right). \tag{3.2}$$

The Euler equations in the relative frame, accounting for fictitious forces,

$$\nabla \cdot \mathbf{w} = 0 \tag{3.3}$$

$$(\mathbf{w} \cdot \nabla)\,\mathbf{w} = -\frac{1}{\rho}\nabla p - \boldsymbol{\Omega} \times (\boldsymbol{\Omega} \times \mathbf{r}) - 2\,(\boldsymbol{\Omega} \times \mathbf{w})\,, \tag{3.4}$$

where the relative velocity, $\mathbf{w}$, is defined as

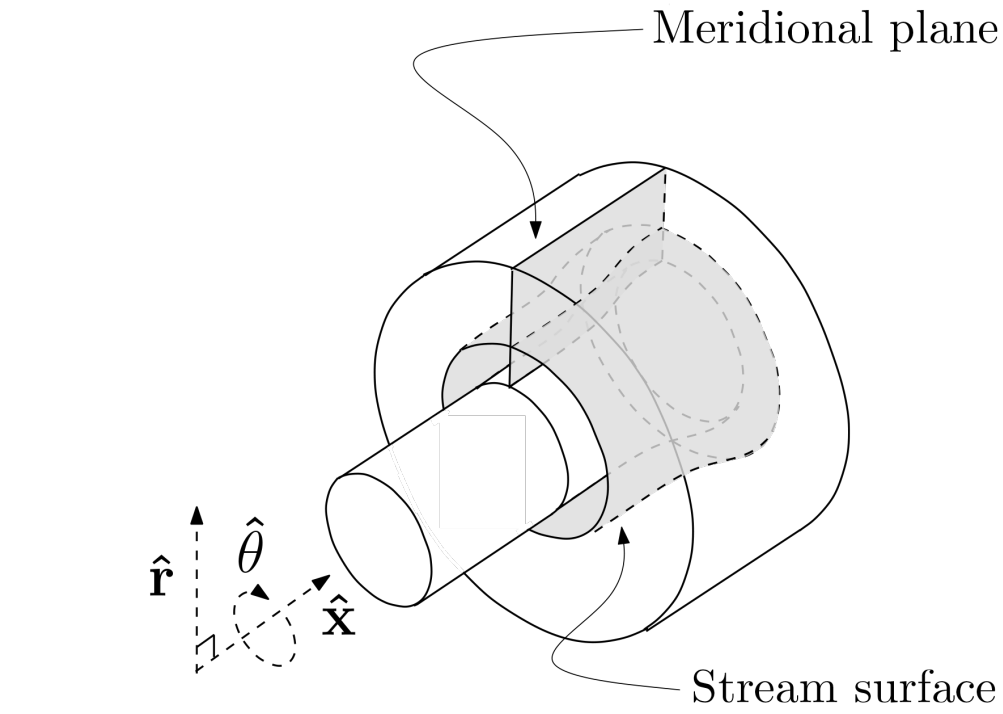
$$\mathbf{u} = \mathbf{w} + (\boldsymbol{\Omega} \times \mathbf{r})\,, \tag{3.5}$$

are used to derive the momentum equation components in the natural coordinate system. The full derivation is documented in [37]; the components are

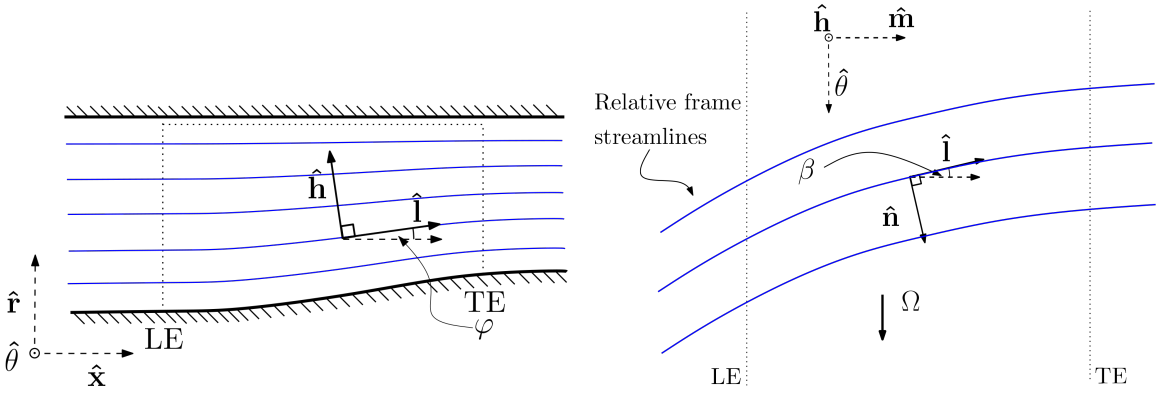
$$\mathbf{n}: \; -w^2\frac{\partial \beta}{\partial l} - \frac{w^2}{r}\sin\varphi\sin\beta = -\frac{1}{\rho}\frac{\partial p}{\partial n} + \Omega^2 r\sin\beta\sin\varphi + 2\Omega w\sin\varphi \tag{3.6}$$

$$\mathbf{l}: w\frac{\partial w}{\partial l} = -\frac{1}{\rho}\frac{\partial p}{\partial l} + \Omega^2 r\sin\varphi\cos\beta \tag{3.7}$$

$$\mathbf{h}: w^2\cos\beta\frac{\partial \varphi}{\partial l} - \frac{w^2}{r}\cos\varphi\sin^2\beta = -\frac{1}{\rho}\frac{\partial p}{\partial h} + \Omega^2 r\cos\varphi + 2\Omega w\cos\varphi\sin\beta. \tag{3.8}$$



(a) Natural coordinate planes



(b) Meridional plane

(c) Stream surface (blade-to-blade)

Figure 3-3: Natural coordinate system [37].

The forces themselves are extracted using the blade force average [49]. The blade force average preserves the three-dimensional forces the blade imparts on the fluid in an axisymmetric sense.

Beginning with the normal component of the momentum equation, Equation 3.6, and taking the pitchwise average,

$$\overline{-w^2\frac{\partial\beta}{\partial l} - \frac{w^2}{r}\sin\varphi\sin\beta + \frac{1}{\rho}\frac{\partial p}{\partial n} - \Omega^2 r\sin\beta\sin\varphi - 2\Omega w\sin\varphi} = 0 \tag{3.9}$$

Since Equation 3.9 is nonlinear, e.g. $\overline{x^2} \neq \bar{x}^2$, higher order terms (H.O.T.) appear in the averaged equation. The terms can be accounted for in bulk,

$$-\bar{w}^2\frac{\partial\bar{\beta}}{\partial\bar{l}} - \frac{\bar{w}^2}{r}\sin\bar{\varphi}\sin\bar{\beta} + \frac{1}{\rho}\frac{\partial\bar{p}}{\partial\bar{n}} - \Omega^2 r\sin\bar{\beta}\sin\bar{\varphi} - 2\Omega\bar{w}\sin\bar{\varphi} + \sum H.O.T. = 0, \tag{3.10}$$

where the overline indicates pitchwise-averaged variables.

The sum of the higher order terms represent the effect of the blades on the axisymmetric flow field and are consequently the forces the blades impart on the fluid, $\sum H.O.T. = -f_n$ (the negative sign maintains consistency with the coordinate system definition). For axisymmetric flow, the higher order terms are zero; if the higher order terms are present, the higher order terms directly account for the flow field's circumferential nonuniformity. Therefore,

$$f_n = -\bar{w}^2\frac{\partial\bar{\beta}}{\partial\bar{l}} - \frac{\bar{w}^2}{r}\sin\bar{\varphi}\sin\bar{\beta} + \frac{1}{\rho}\frac{\partial\bar{p}}{\partial\bar{n}} - \Omega^2 r\sin\bar{\beta}\sin\bar{\varphi} - 2\Omega\bar{w}\sin\bar{\varphi}. \tag{3.11}$$

The same procedure is used to define the parallel and binormal forces,

$$f_l = \bar{w}\frac{\partial\bar{w}}{\partial\bar{l}} + \frac{1}{\rho}\frac{\partial\bar{p}}{\partial\bar{l}} - \Omega^2 r\sin\bar{\varphi}\cos\bar{\beta} \tag{3.12}$$

$$f_h = \bar{w}^2\frac{\partial\bar{\varphi}}{\partial\bar{l}}\cos\beta - \frac{\bar{w}^2}{r}\cos\bar{\varphi}\sin^2\bar{\beta} + \frac{1}{\rho}\frac{\partial\bar{p}}{\partial\bar{h}} - \Omega^2 r\cos\bar{\varphi} - 2\Omega\bar{w}\cos\bar{\varphi}\sin\bar{\beta}. \tag{3.13}$$

The averaged flow variables in Equations 3.11, 3.12, and 3.13 can be extracted from single-passage RANS calculations to solve for the forces. An extraction grid is defined for the inducer geometry, shown in Figure 3-4. An area average is used

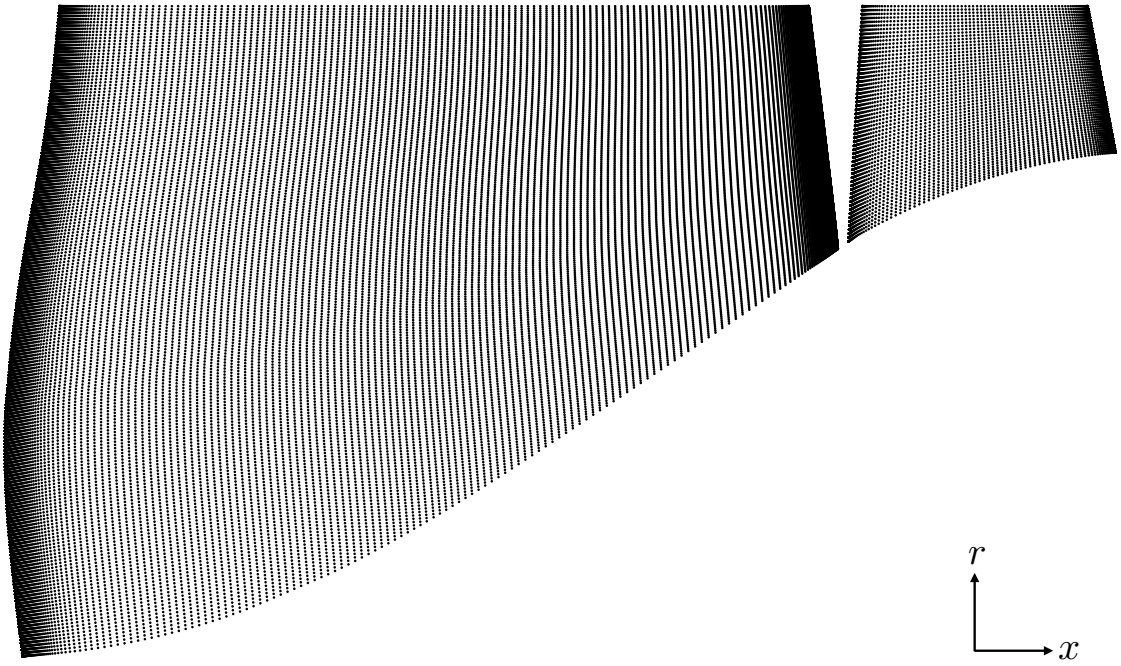


Figure 3-4: Body force extraction grid for the MIT inducer.

to pitchwise-average the flow variables at each grid point and a second order finite difference scheme is used to calculate the required gradients. The forces are extracted for each operating point on the RANS characteristic seen in Figure 2-4.

3.3.1 Force Extraction Process Validation

To assess the extracted forces, the forces were directly applied to the body force model calculation as steady, axisymmetric source terms. The steady, axisymmetric forces are unable to respond to changes in the flow field, as opposed to a "full model" calculation, where the forces are calculated by querying the local flow field. The extracted forces were seen to capture both the flow fields and the global performance of the MIT inducer. A summary of the force extraction assessment results is presented here – a full discussion can be found in [37].

The body force model was implemented in ANSYS CFX. Without the blades, the mesh geometry consists of the hub and shroud lines, composing a 20° wedge of approximately one million elements, refined near the leading edges to help capture the tip leakage flows and high leading edge loading [37], with periodic boundary

conditions. The wedge was chosen over a full wheel mesh to take advantage of the axisymmetric nature of the steady calculations and reduce computational time. The body forces themselves were implemented as "user-defined interpolation functions" – input values of (x, r) and the associated force at each extraction grid point were used by CFX to determine the forces on the body force calculation mesh, with the force directions determined by the pitchwise-averaged RANS flow angles. Due to the CFX source term implementation, a user-defined Fortran function was necessary to transform the forces in the natural coordinate system into the cylindrical coordinate system. In the tip gap, where the blade does not affect the flow, the body forces were set to zero. Similar to the single-passage RANS calculations, a total pressure boundary condition was imposed at the inlet with a mass flow boundary condition at the outlet, setting flow coefficient, and the k-ω SST turbulence model was used. The working fluid was water at 25°C.

Since the goal of the body force model is to reproduce the pitchwise-averaged flow field and performance of the full three-dimensional inducer, the primary metrics used for assessment are the local velocity field and global head rise performance. The extracted forces are able to capture the bulk flow field for all points on the characteristic, with the primary discrepancies in axial backflow extent. A comparison of the steady, axisymmetric forces characteristic with the RANS characteristic is seen in Figure 3-5. The extracted force calculations capture the global head rise within 5%. A comparison of the local flow fields at $\phi = 0.05, 0.07, \text{and } 0.10$ is seen in Figure 3-6, while streamwise plots of axial velocity are compared for design point ($\phi = 0.07$) in Figure 3-7.

The upstream backflow occurs due to the pressure driven tip clearance flows, exacerbated by the leading edge backsweep, which serves to enlarge the effective tip gap at the leading edge. The axial extent of backflow varies depending on flow coefficient; for higher blade loading at lower flow coefficients, the backflow is extensive, nearly two diameters upstream for $\phi = 0.05$, while almost nonexistent at flow coefficients greater than $\phi = 0.09$. While the primary discrepancies in the steady, axisymmetric calculations are in the backflow region near the leading edge tip, as seen in Figure 3-7,

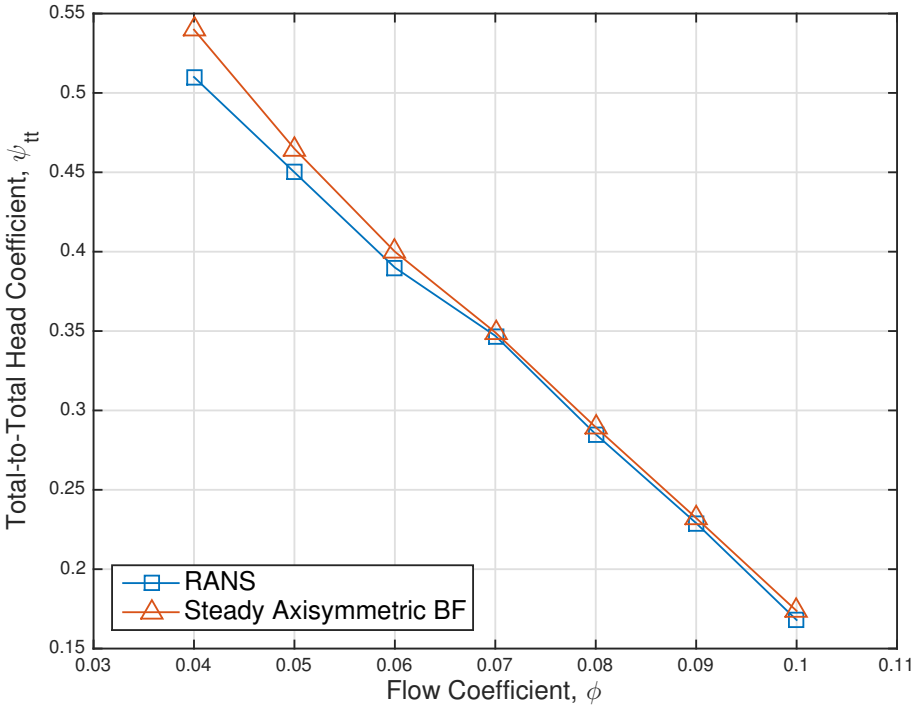


Figure 3-5: MIT inducer RANS and body force characteristics, indicating good agreement while reflecting the body force model's difficulty in capturing the backflow region at lower flow coefficients.

the calculations are able to capture the variation in axial extent, with discrepancies under 20%.

3.4 Previous Blade Passage Models

With the extracted forces validated, the second component of the body force model is considered. Previous versions of the blade passage model, successfully applied to aero-engine turbomachines such as axial/centrifugal compressors and fans, were applied to modeling the MIT inducer. Both models tested were assessed to be unfeasible for the inducer geometry due to model sensitivity; small perturbations in the flow field caused large changes in the calculated body forces, causing spurious recirculation regions and, consequently, convergence issues. The results support the hypothesized root cause of the sensitivity of stagnation pressure loss to changes in incidence (i.e. flow angle) stemming from the inducer's high stagger angles.

The governing equations for the two blade passage models attempted, the Peters

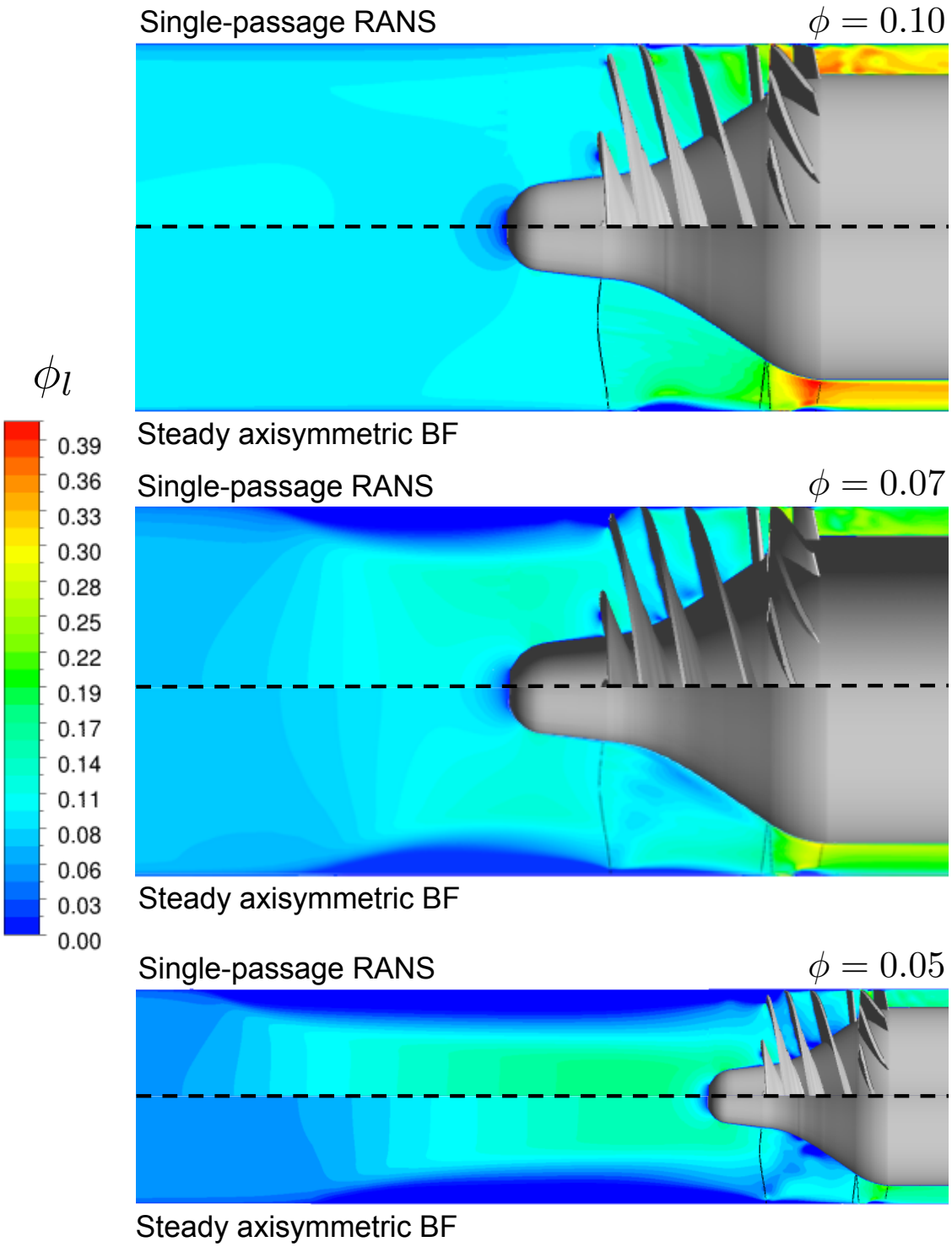
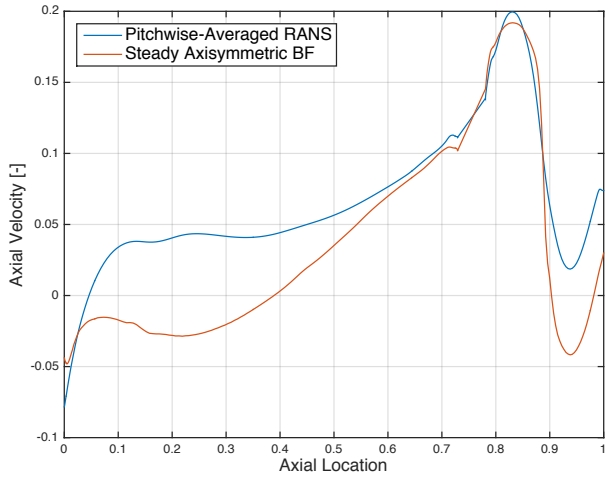
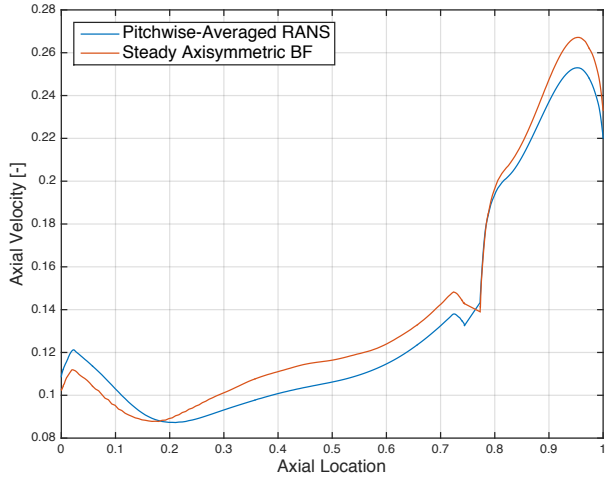


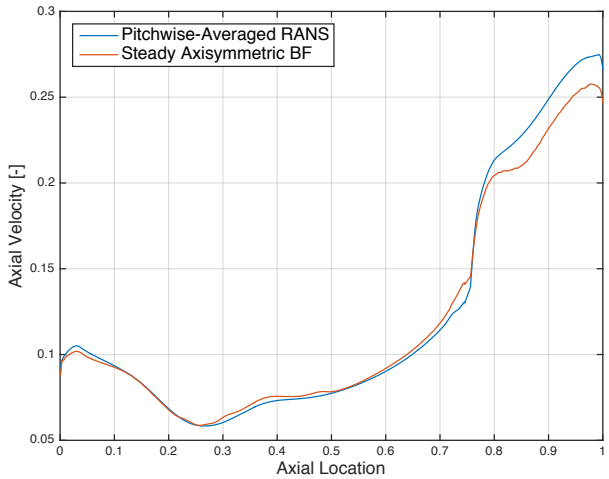
Figure 3-6: Comparison of RANS and body force calculations for a range of flow coefficients. Extracted forces capture the bulk flow field with primary discrepancies in axial extent of backflow. Axial velocity contours nondimensionalized by tip velocity.



(a) Tip



(b) Midspan



(c) Hub

Figure 3-7: Streamwise axial velocity distributions throughout the MIT inducer blade domains. Primary discrepancy near backflow region at the leading edge tip. Axial velocity nondimensionalized by tip velocity.

model and a look-up table, are based on Marble's force derivations [45]. The steady Euler equations with body forces, $\mathbf{f}$, can be combined with the Gibbs equation,

$$Tds = dh - \frac{1}{\rho}dp, \tag{3.14}$$

to become

$$w_m \frac{\partial h_t}{\partial m} - \rho f_\theta \Omega r = T w_m \frac{\partial s}{\partial m} + \rho\, \mathbf{w} \cdot \mathbf{f}, \tag{3.15}$$

where m indicates in the meridional direction and h_t is stagnation enthalpy. The Euler turbine equation,

$$dh_t = \Omega\, d\left(r u_\theta\right), \tag{3.16}$$

can be combined with the circumferential momentum equation to yield

$$\frac{\partial h_t}{\partial m} = \frac{f_\theta \rho \Omega r}{w_m}. \tag{3.17}$$

Equations 3.15 and 3.17 combine to form

$$\frac{\partial s}{\partial m} = -\frac{\rho w}{T w_m} f_l, \tag{3.18}$$

since the parallel body force component is parallel to the relative flow, i.e. $\mathbf{w} \cdot \mathbf{f} = w f_l$.

The derivation yields two key attributes of the body force modeling approach. Equation 3.17 shows that the change in stagnation enthalpy along a meridional streamline is proportional to the rate at which torque applied by the circumferential body force does work on the fluid – the normal force, f_n, can therefore be seen as representative of the blade force and the imparted flow turning. Equation 3.18 implies that the changes in entropy along a meridional streamline are due to the parallel force, which accounts for the viscous shear stress losses. The legacy body force models aim to determine the functional dependence of the two forces, f_n and f_l, on the local flow field.

3.4.1 Blade Passage Model by Peters

The blade passage model by Peters was used to investigate inlet-fan interaction and distortion from short-inlet turbofan nacelles. The approach assumes a staggered blade passage depicted in Figure 3-8a, based on Gong's blade passage model [47]. An overview of the ideas behind the model is presented here – a full derivation is in [36]. h is the staggered spacing, κ is the local blade metal angle, defined as the angle between the local camber line and the axial direction, and δ is the flow deviation from the blade metal angle, i.e.

$$\delta = \beta - \kappa. \tag{3.19}$$

The blade spacing is defined as

$$h = \frac{2\pi r\sqrt{\sigma}\cos\kappa}{N_B}, \tag{3.20}$$

where σ is the solidity and N_B is the number of rotor blades. The model also assumes negligible radial flows, $\frac{w_r}{w} << 1$.

The normal force is decomposed into two components, a blade loading component, $f_{n_{\nabla p}}$, and a deviation component, f_{n_δ},

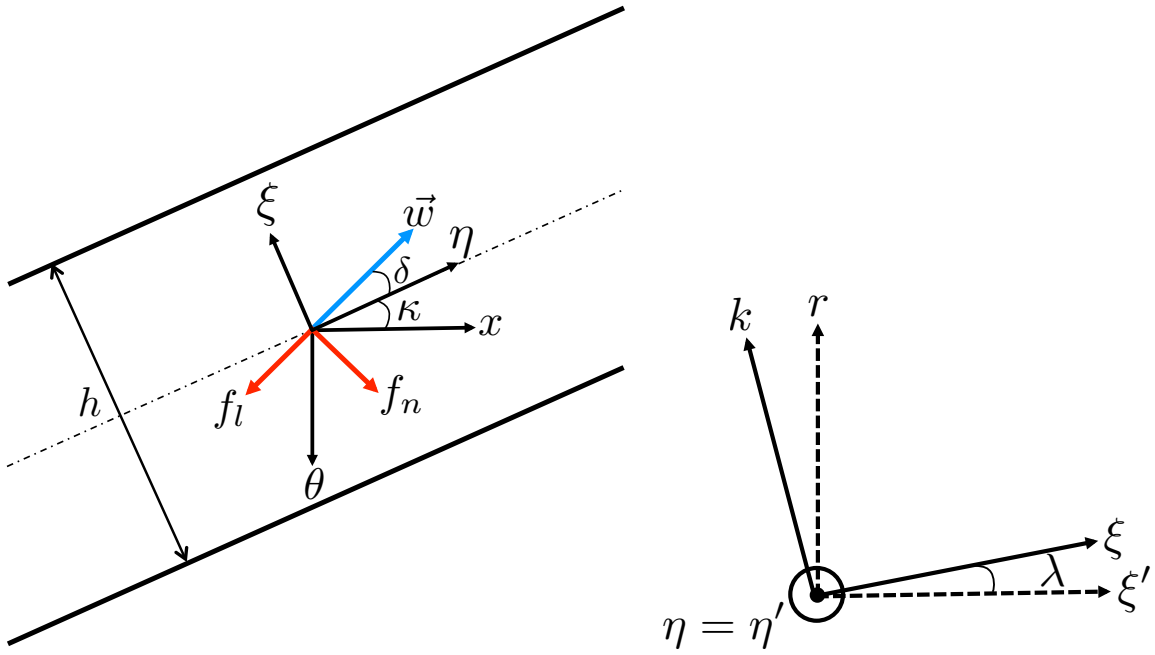
$$f_n = f_{n_{\nabla p}} + f_{n_\delta}. \tag{3.21}$$

Through a force balance across the blade and a cross-passage momentum balance, $f_{n_{\nabla p}}$ and f_{n_δ} were respectively formulated, yielding

$$f_n = \frac{1}{\rho}\frac{\partial p}{\partial x}\frac{\sin\kappa}{\cos^2\kappa} + \frac{K_n}{h}w_\eta w_\xi. \tag{3.22}$$

$K_n(x, r)$, the normal force coefficient, is an empirical parameter determined from pitchwise-averaged RANS calculations linking the force and the flow field, while w_η and w_ξ are the in-passage velocity components.

To account for the radial flows that result from blade lean, Peters rotated the blade passage by the local lean angle, λ, defined as the angle between the blade



(a) Staggered blade passage

(b) Rotation of passage by blade lean angle, λ

Figure 3-8: Blade passage model by Peters [36].

camber surface and the radial axis, as shown in Figure 3-8b. The transformation of the normal force to cylindrical coordinates gives a radial component to the forces.

The parallel force formulation reflects a rotor loss bucket, where there is a quadratic dependence of stagnation pressure loss on relative Mach number, M_{rel}, to better capture off-design loss,

$$f_l = \frac{K_{l_1}}{h}\left(M_{rel}^2 + K_{l_2}\left(M_{rel} - M_{ref}\right)^2\right) w^2, \tag{3.23}$$

where M_{ref} is the averaged relative Mach number at the blade row inlet at design point, and K_{l_1} and K_{l_2} are empirical parameters also calculated from RANS simulations.

For the investigation in the present work, Gong's original parallel force formulation was used. The calculation of K_{l_1} and K_{l_2} requires iteration between comparing body force simulations and RANS calculations while the empirical term in the original force equation can be directly solved for. Moreover, only design point was tested for

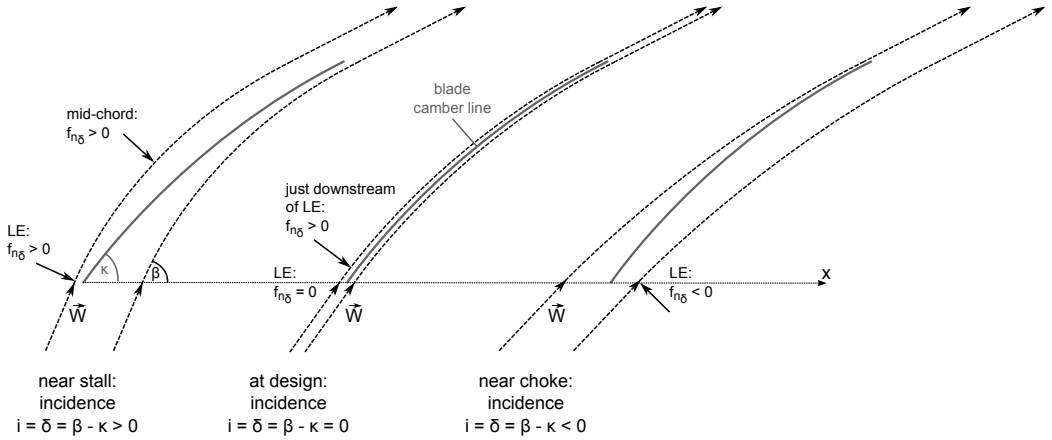


Figure 3-9: Peters model inherent stability – deviation component of normal force turns the flow towards local blade metal angle [36].

the inducer, negating the advantages of Peters' formulation. Gong's parallel force equation is based on a drag force which scales with the dynamic pressure relative to the blade row,

$$f_l = \frac{K_l}{h} w^2, \tag{3.24}$$

where K_l is now the only parallel force empirical coefficient.

A notable attribute of Peters' model is its inherent stability. The normal force equation, Equation 3.22, can be solved in terms of the deviation angle through trigonometry relations,

$$f_n = \frac{1}{\rho} \frac{\partial p}{\partial x} \frac{\sin \kappa}{\cos^2 \kappa} + \frac{1}{2} \frac{K_n}{h} w^2 \sin(2\delta). \tag{3.25}$$

An examination of Equation 3.25 reveals that deviation component of the normal force turns the flow back towards the local blade metal direction whenever the streamline and the camber line do not align, as sketched in Figure 3-9. For a positive deviation angle, f_{n_δ} is positive, while for a negative deviation angle f_{n_δ} is negative; in both cases, the flow is turned back towards the blade metal angle.

To maintain consistency with the forces extracted as described in Section 3.3, both the extracted natural coordinate forces and the blade passage model forces are transformed into the cylindrical coordinate system. A third empirical parameter is

introduced, K_r, for the radial component, and the force components are therefore

$$f_x = f_{n_{\nabla p_x}} + K_n \cdot f_{n_{\delta_x}} + K_l \cdot f_{p_x} \tag{3.26}$$

$$f_\theta = f_{n_{\nabla p_\theta}} + K_n \cdot f_{n_{\delta_\theta}} + K_l \cdot f_{p_\theta} \tag{3.27}$$

$$f_r = K_n \cdot f_{n_{\delta_r}} + K_l \cdot f_{p_r} + K_r \cdot f_r \cdot \frac{u_{tip}^2}{c}, \tag{3.28}$$

where $\frac{u_{tip}^2}{c}$ is a nondimensionalization constant (u_{tip} is the tip speed and c is the axial chord), or, explicitly,

$$\begin{bmatrix} f_x - \frac{1}{\rho}\frac{\partial p}{\partial x}\frac{\sin\kappa}{\cos^2\kappa}\frac{w_\theta}{w} \\ f_\theta + \frac{1}{\rho}\frac{\partial p}{\partial x}\frac{\sin\kappa}{\cos^2\kappa}\frac{w_x}{w} \\ f_r \end{bmatrix} = \begin{bmatrix} \frac{w_\eta w_\xi}{h}\frac{w_\theta}{w} & -\frac{w^2}{h}\frac{w_x}{w} & 0 \\ \frac{-w_\eta w_\xi}{h}\frac{w_x}{w} & -\frac{w^2}{h}\frac{w_\theta}{w} & 0 \\ \frac{w_\eta w_\xi}{h}\frac{w_r}{w} & -\frac{w^2}{h}\frac{w_r}{w} & \frac{u_{tip}^2}{c} \end{bmatrix} \begin{bmatrix} K_n \\ K_l \\ K_r \end{bmatrix}. \tag{3.29}$$

It is important to note that the model formulation is fundamentally unchanged. f_x, f_θ, f_r, and the flow variables are known from the force extraction process, allowing $K_n(x,r)$, $K_l(x,r)$, and $K_r(x,r)$ to be calculated by solving the system of equations presented by Equation 3.29 at every (x,r) grid point.

Assessment of the Blade Passage Model by Peters

The blade passage model by Peters was implemented in CFX. The body forces were allowed to query the flow field directly to solve for the forces at each calculation grid point in a full model calculation. The simulation was initialized using the solution from the steady, axisymmetric force calculation. The steady, axisymmetric body force solution should be the same as the full model solution; the goal of both calculations are the same, namely to recreate the pitchwise-averaged flow field of the MIT inducer.

The selected test operating condition was design point, $\phi = 0.07$. Upon running the simulation, the calculation experienced convergence issues, with flow exiting the inlet and entering the outlet. An investigation into the cause behind the model failure revealed a sensitivity in the model stemming from the normal force coefficient.

To assess the calculation failure, the fan body force model case was compared

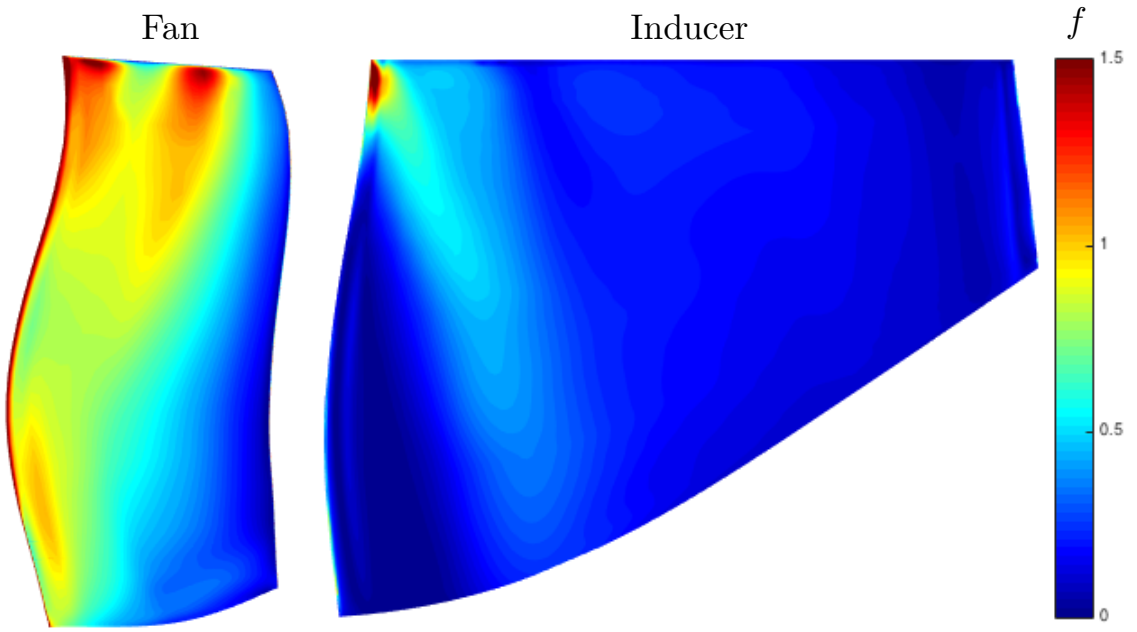


Figure 3-10: Comparable magnitudes of total force for fan and inducer body force cases. Force contours nondimensionalized by inlet dynamic pressure.

with the inducer case. While the body forces themselves are on the same order of magnitude, as seen in Figure 3-10, Figure 3-11 shows the inducer normal force coefficients are two orders of magnitude higher. The normal force coefficient dictates the sensitivity of the model to perturbations in the flow field – a higher K_n indicates higher sensitivity. Correspondingly, the two normal force components, $f_{n_{\nabla p}}$ and f_{n_δ}, scale with the coefficient to sum to the required force, as shown in Figure 3-12. If Equation 3.22 is considered, for a small perturbation in velocity or pressure gradient there is a relatively large change in normal force in the inducer model. Practically, the implication is that as the flow solver iterates towards a solution, even if the solution is initialized with the steady, axisymmetric calculation, there are changes in the flow field with each iteration that cause the forces to deviate far from the expected values. Consequently, the sensitivity of the model causes convergence issues in the solver.

In an attempt to desensitize the model, gains were introduced to the two normal force elements. Shown in Figure 3-13, the gains scale the magnitudes of each of the

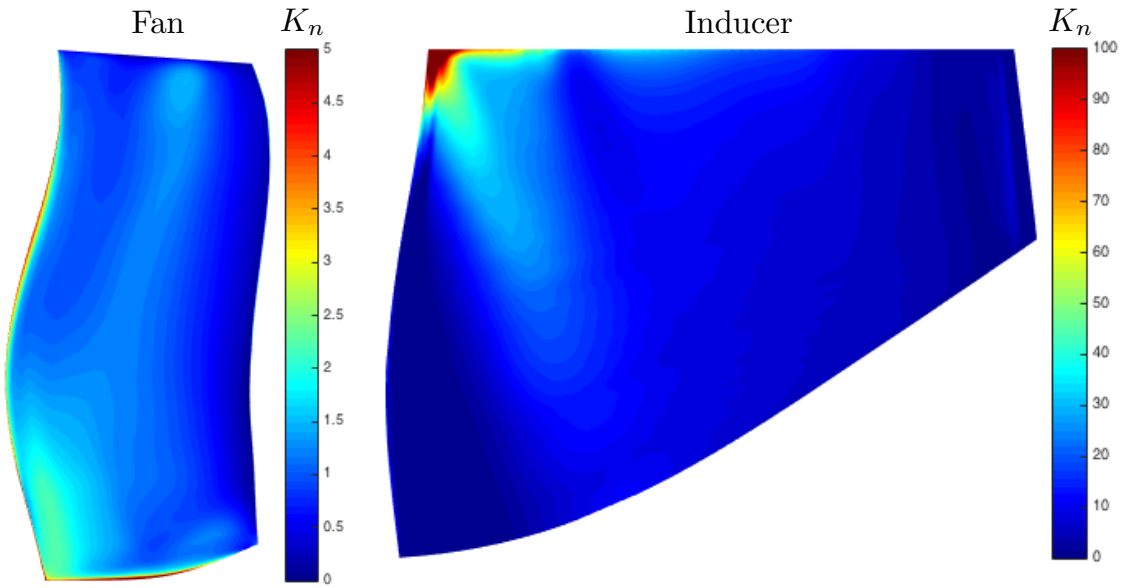


Figure 3-11: Normal force coefficients for inducer case are two orders of magnitude higher than fan case, resulting in model sensitivity.

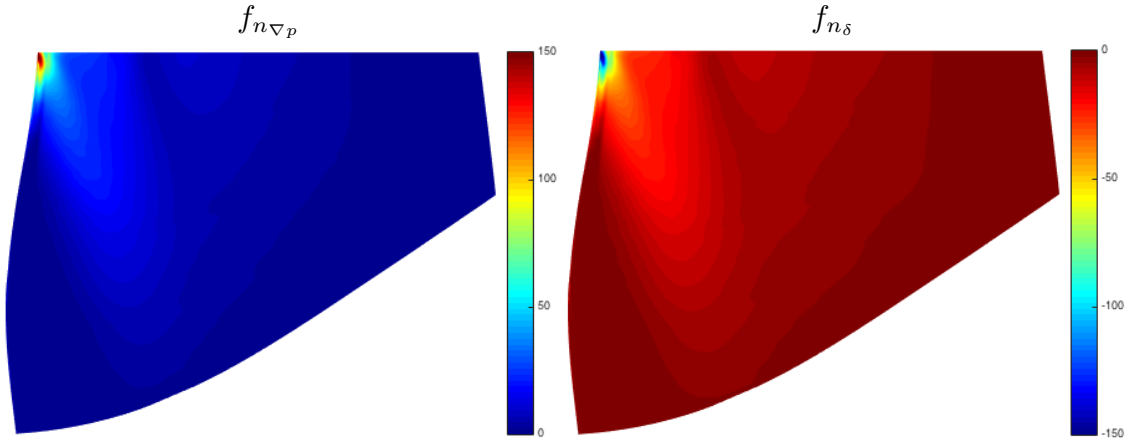


Figure 3-12: Normal force components for the inducer are two orders of magnitude higher than the force itself as a consequence of the normal force coefficients (Figure 3-11).

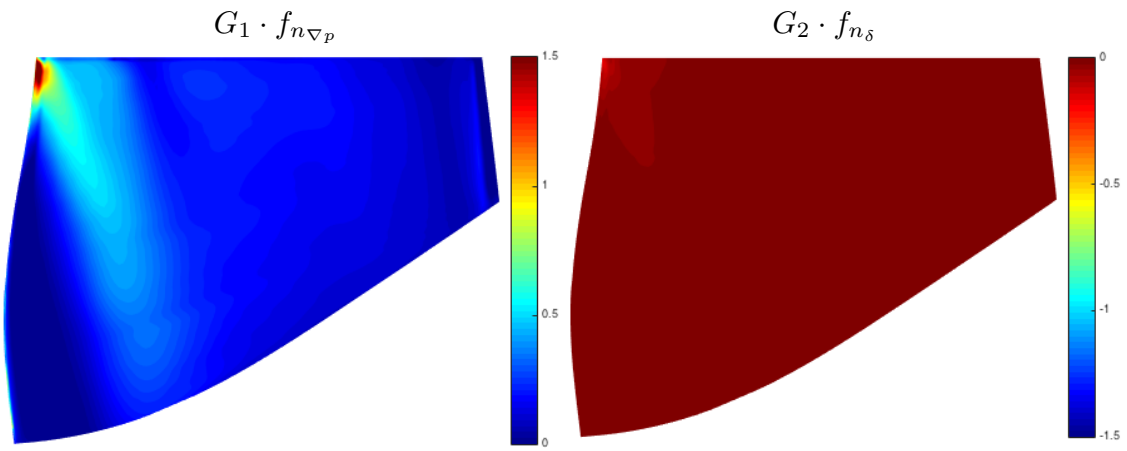


Figure 3-13: Desensitization of normal force terms by introducing gains.

force components while ensuring they sum to the same extracted normal force,

$$f_n = G_1 \cdot f_{n_{\nabla p}} + G_2 \cdot f_{n_\delta}. \tag{3.30}$$

However, even with the desensitization, the full model calculation is unable to converge. The desensitization scales the forces to magnitudes shown to be able to converge in the fan geometry case, implying the model sensitivity issues are inherently caused by the inducer geometry itself. When comparing the fan and inducer geometries, the primary differences are the stagger angles, suggesting the high stagger angles in the inducer are the cause for model sensitivity. From the Peters model alone, the link between model and geometry is unclear; this connection is investigated thoroughly in Chapter 4 using an inducer-specific body force model.

3.4.2 Look-Up Table Approach

An alternate blade passage model is the look-up table approach. Instead of using an analytical model such as the Peters blade passage model, the look-up table approach instead implies the use of a discretized method. The method relies on look-up tables based on local flow field quantities to determine the force response. Look-up tables were successfully used by Benneke [34] to capture stall precursors in centrifugal compressors with vaned diffusers.

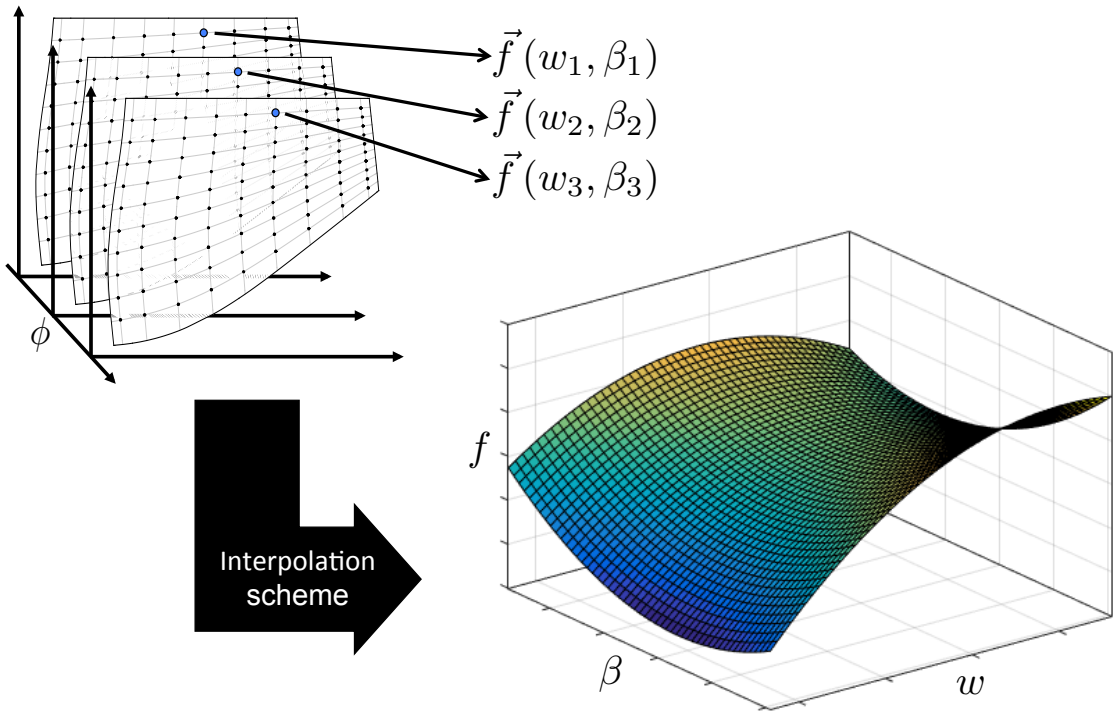
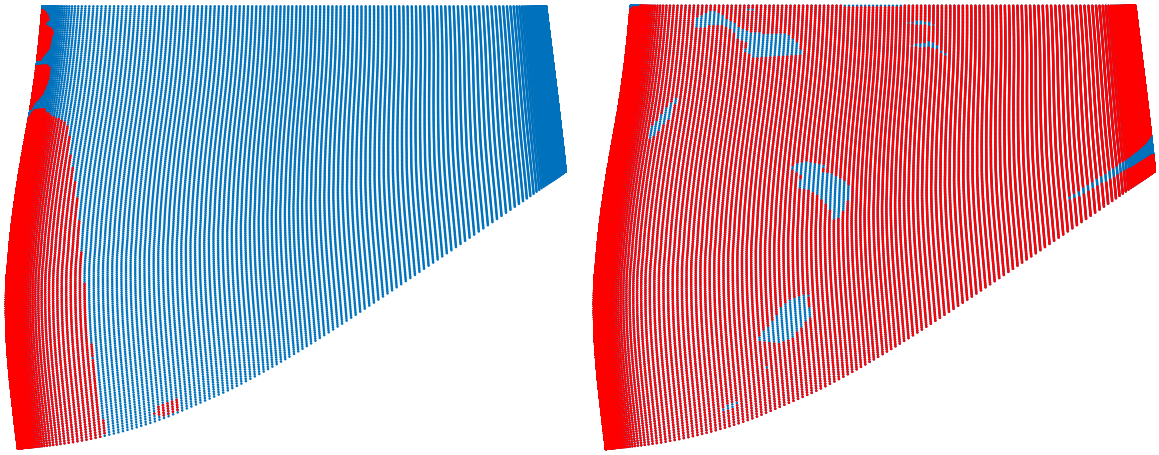


Figure 3-14: Look-up table sketch for single (x, r) point.

The extracted forces, as obtained in Section 3.3, define the force and pitchwise-averaged flow variables along the characteristic at every (x, r) point on the extraction grid. Based on Benneke's work, look-up tables were constructed for every grid point for the three force components, normal, parallel, and binormal, as a function of relative velocity magnitude, w, and relative flow angle, β, as sketched in Figure 3-14.

However, for large regions within the inducer, the look-up tables were double-valued (i.e. non-monotonic) for both independent variables. Figure 3-15 plots the grid points where forces are non-monotonic with flow coefficient for the respective independent variables. Figure 3-16 is a monotonic normal force distribution reflecting the inducer characteristic, extracted at midspan, 25 % chord. Near the leading edge hub, shown in Figure 3-17, the table is multivalued and unable to determine the corresponding force for a given local flow field. A test case was run for the inducer look-up table approach, exhibiting spurious recirculation regions within two iterations. Based on Benneke's issues with multivalued entries and other challenges with the look-up approach, the method was deemed unviable.



(a) Relative velocity magnitude.

(b) Relative flow angle.

Figure 3-15: Double-valued (non-monotonic with flow coefficient) look-up table regions in the inducer, marked in red.

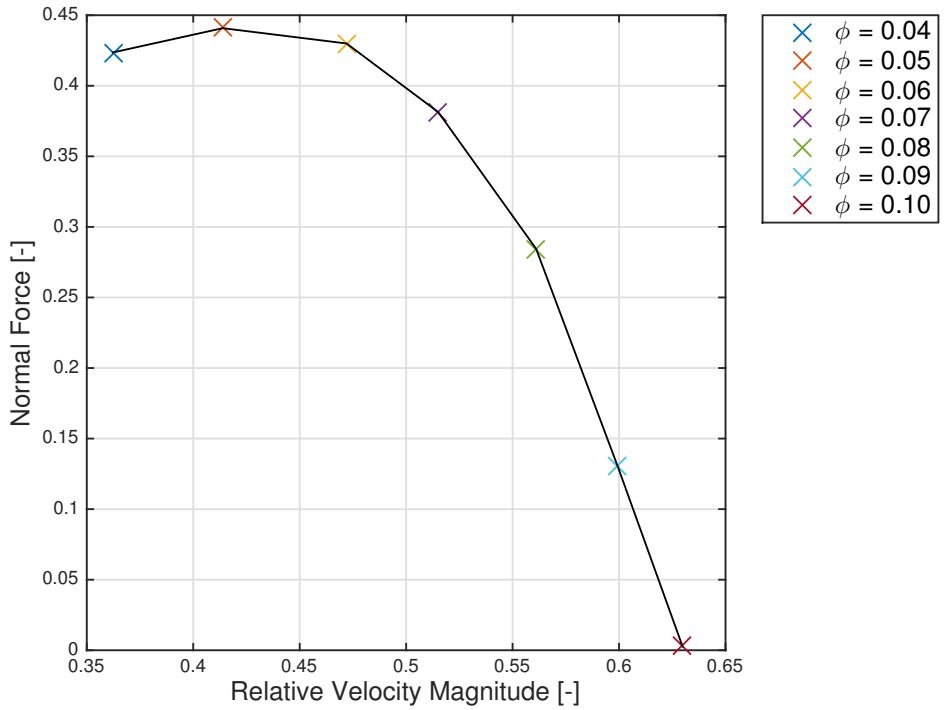


Figure 3-16: Monotonic normal force distribution as a function of relative velocity at midspan and 25% chord.

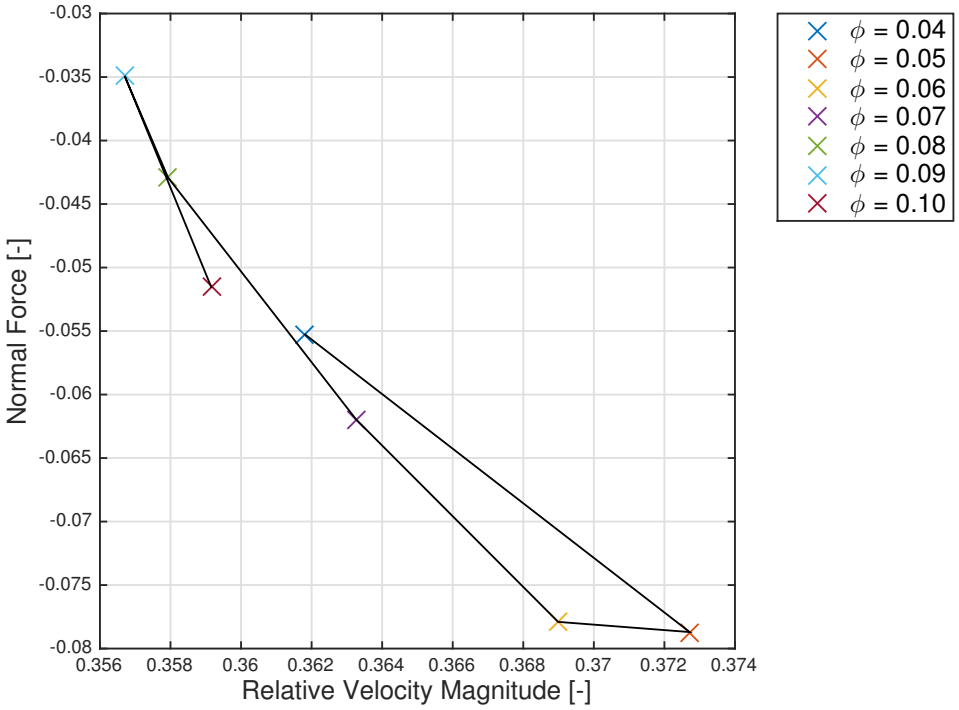


Figure 3-17: Multivalued normal force distribution as a function of relative velocity at the leading edge hub.

Multivalued look-up tables are a consequence of the inducer design. In the case of relative flow angle, an examination of the distribution near the leading edge indicates a narrow range of flow angles along the characteristic, shown at 50% span in Figure 3-18. This is due to the highly tangential flow entering the blade domain, stemming from the inducer's low flow coefficient design – nearly tangential flow imposes the small variation of flow angles along the characteristic. The narrow range of flow angles shown in Figure 3-18 is indicative of the rest of the inducer blade domain; other query points reveal comparable ranges, which causes large portions of the blade domain being double-valued for the flow angle, as seen in Figure 3-15b. The small ranges of flow angle seen in the blade domain support the hypothesis that the inducer geometry itself is not applicable to body force modeling, and, moreover, have critical implications for the model, discussed in depth in Chapter 4.

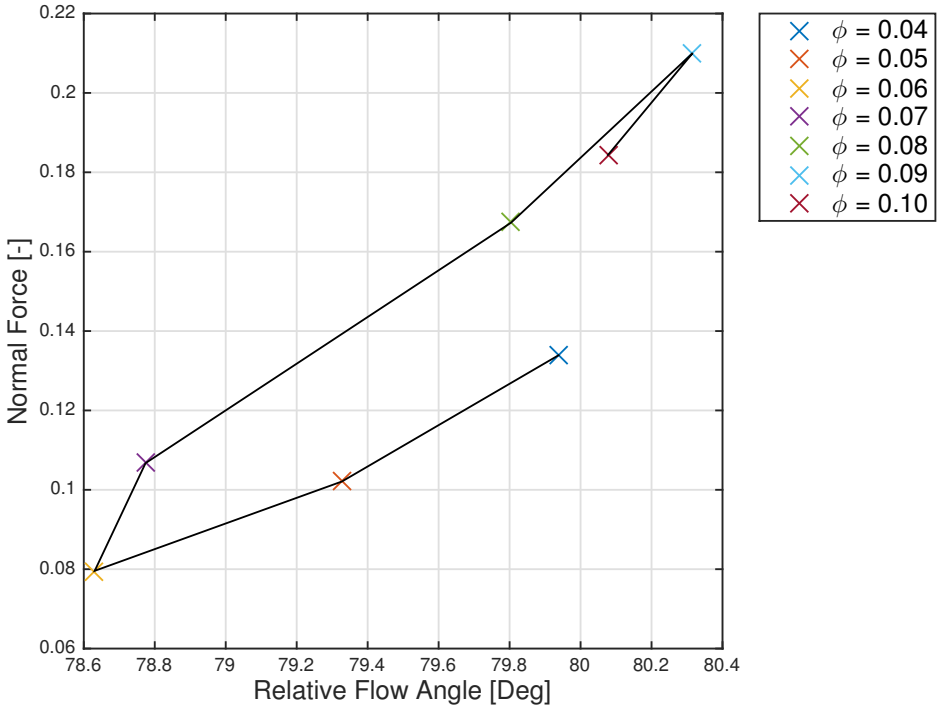


Figure 3-18: Narrow range of relative flow angle at midspan leading edge indicative of narrow range of incidence angles along inducer characteristic.

3.5 Summary

Sorensen demonstrated the force extraction process to reproduce the pitchwise-averaged flow field of the MIT inducer for its entire characteristic. Two previously developed blade passage models, the formulation by Peters and the look-up table approach, were assessed to be unviable for application to inducer geometries. Results from both models suggest the inducer geometry itself is responsible for model sensitivity. Chapter 4 will clarify the link between the inducer geometry and model sensitivity through investigation of rotor loss buckets, where the stagnation pressure loss is sensitive to changes in incidence, manifesting in the model as sensitive empirical term characteristics.

Chapter 4

Inducer Blade Passage Model

A blade passage model was developed by Sorensen [37] to address the challenges of adapting body force modeling to inducer geometries. However, the full model exhibited spurious recirculation regions and convergence issues. The model was investigated using a low speed axial compressor validation case, where it was found to be unable to capture aerodynamic blockage. Once corrected, the model formulation was demonstrated to be sound and able to capture large separated flow near peak pressure rise. The results suggest that the inducer geometry is the root cause of the convergence issues. The nearly tangential flow in the blade passage, a consequence of the inducer's low flow coefficient design and associated high stagger angles, result in comparatively narrow loss buckets, which tracks the effect of incidence angle on stagnation pressure loss. The narrow loss buckets manifest in the model as narrow empirical term characteristics, resulting in model sensitivity and the observed convergence issues. The results indicate the blade passage model by Sorensen is applicable for the higher flow coefficient designs typically found in aero-engine compressors and fans, while steps for desensitization will need to be implemented for inducer geometries.

4.1 Blade Passage Model by Sorensen

The blade passage model consists of normal, parallel, and binormal force components along with a blade metal blockage model. The force formulations are derived from

the momentum equations, with the force extraction governing equations (Equations 3.11, 3.12, and 3.13) as their basis, and include empirical terms to connect the blade forces to the flow field. The inputs into the model, all defined throughout the blade domain, are:

- From geometry:
  - Axial and radial gradients of blade metal angle, $\frac{\partial \kappa}{\partial x}$ and $\frac{\partial \kappa}{\partial r}$
  - Axial and radial gradients of pitch angle of the potential flow streamlines, $\frac{\partial \varphi_{GP}}{\partial x}$ and $\frac{\partial \varphi_{GP}}{\partial r}$
- Empirical terms from pitchwise-averaged RANS:
  - Relative flow angle deviation gradient, $\frac{\partial \delta_\beta}{\partial l}$
  - Meridional entropy gradient, $\frac{\partial s}{\partial m}$
  - Pitch angle deviation gradient, $\frac{\partial \delta_\varphi}{\partial l}$

The model addresses several limitations of Peters' blade passage model, detailed in [36, 46, 48], capturing relative streamline curvature, providing physical interpretation of the model formulation from first principles, and accounting for blade metal blockage.

4.1.1 Normal Force Model

From the pitchwise averaged momentum equation in the normal direction, Equation 3.11, the Sorensen's blade passage model formulation defines the normal body force as

$$f_n = -w^2 \frac{\partial \beta}{\partial l} - \frac{w^2}{r} \sin\varphi \sin\beta + \frac{1}{\rho} \frac{\partial p}{\partial n} - \Omega^2 r \sin\beta \sin\varphi - 2\Omega w \sin\varphi. \tag{4.1}$$

Note that for the extracted forces, the flow variables, $\bar{\beta}$, $\bar{w}$, $\bar{p}$, and $\bar{\varphi}$, are calculated from pitchwise-averaged RANS. For the blade passage model, β, w, p, and φ, are queried from the flow field calculated based on the body forces. A dependence on the geometry is introduced by decomposing the relative flow angle into the blade metal

angle, κ, and the flow's deviation from κ, δ_β, where

$$\beta = \kappa + \delta_\beta. \tag{4.2}$$

Equation 4.1 therefore becomes

$$f_n = -w^2 \left(\frac{\partial \kappa}{\partial l} + \frac{\partial \delta_\beta}{\partial l} \right) - \frac{w^2}{r} \sin\varphi \sin\beta + \frac{1}{\rho} \frac{\partial p}{\partial n} - \Omega^2 r \sin\beta \sin\varphi - 2\Omega w \sin\varphi, \tag{4.3}$$

where $\frac{\partial \delta_\beta}{\partial l}$ is referred to as the relative flow angle deviation gradient. Transforming the blade metal angle gradient into the absolute coordinate system yields

$$\begin{aligned} f_n = &- w^2 \left(\left(\frac{\partial \kappa}{\partial x} \cos\varphi + \frac{\partial \kappa}{\partial r} \sin\varphi \right) + \frac{\partial \delta_\beta}{\partial l} \right) - \frac{w^2}{r} \sin\varphi \sin\beta + \frac{1}{\rho} \frac{\partial p}{\partial n} \\ &- \Omega^2 r \sin\beta \sin\varphi - 2\Omega w \sin\varphi. \end{aligned} \tag{4.4}$$

A numerical instability caused by a positive feedback loop between the pressure gradient and the normal force was identified in Equation 4.4. Using influence coefficients to rewrite the pressure gradient in terms of the velocity field [37], the final normal force equation is

$$\begin{aligned} f_n = &\Bigg[-w^2 \left(\left(\frac{\partial \kappa}{\partial x} \cos\varphi + \frac{\partial \kappa}{\partial r} \sin\varphi \right) + \frac{\partial \delta_\beta}{\partial l} \right) - 2\frac{w^2}{r} \sin\varphi \sin\beta \\ &-2\Omega^2 r \sin\beta \sin\varphi - 2\Omega w \sin\varphi \left(1 + \sin^2\beta\right) - f_l \sin\beta \cos\beta \Bigg] \frac{1}{1 - \sin^2\beta + K_{off}}, \end{aligned} \tag{4.5}$$

where K_{off} is a constant to prevent singularities when the relative flow angle approaches 90°.

The inputs into the normal force equation are therefore the blade metal angle gradients and the relative flow angle deviation gradient. Physically, the relative flow angle deviation gradient represents the rate of change of the deviation of the flow from the blade, capturing the tendency of the flow's displacement from the streamline curvature prescribed by the blade camber line. The gradient is extracted from single-passage RANS calculations, connecting the flow field to the inducer blade forces,

by rearranging Equation 4.5 to solve for $\partial\delta_\beta/\partial l$ in terms of pitchwise-averaged flow variables from RANS and the extracted forces, f_n and f_l for every (x, r) grid point.

4.1.2 Parallel Force Model

Combining the definition of the streamwise force, Equation 3.12, and the Gibbs equation, Equation 3.14, yields

$$f_l = -T\frac{\partial s}{\partial l} - \Omega^2 r \sin\varphi\cos\beta, \tag{4.6}$$

which, by recasting the entropy gradient in the parallel direction in terms of the meridional entropy gradient, can be rewritten as

$$f_l = -T\cos\beta\frac{\partial s}{\partial m} - \Omega^2 r \sin\varphi\cos\beta. \tag{4.7}$$

The meridional entropy gradient, $\partial s/\partial m$ is the empirical term for the parallel force model and is the only input for the parallel force. It captures entropy generation in the flow and is calculated using the single-passage RANS calculations by rearranging Equation 4.7 to solve for $\partial s/\partial m$ everywhere in the blade domain in terms of pitchwise-averaged flow variables from RANS and the extracted parallel force.

4.1.3 Binormal Force Model

Similar to the derivation of the normal force model, the binormal force model is based on the decomposition of the pitch angle,

$$\varphi = \varphi_{GP} + \delta_\varphi, \tag{4.8}$$

where φ_{GP} is the local angle of the potential flow streamlines through the body force blade domain, termed the gas path angle, and δ_φ is the deviation from the gas path

angle. Substituting Equation 4.8 into Equation 3.13 yields

$$\begin{aligned} f_h = & w^2 \cos\beta \left(\left(\frac{\partial \varphi_{GP}}{\partial x} \cos\varphi + \frac{\partial \varphi_{GP}}{\partial r} \sin\varphi \right) \cos\beta + \frac{\partial \delta_\varphi}{\partial l} \right) - \frac{w^2}{r} \cos\varphi \sin^2\beta \\ & + \frac{1}{\rho} \frac{\partial p}{\partial h} - \Omega^2 r \cos\varphi - 2\Omega w \cos\varphi \sin\beta, \end{aligned} \tag{4.9}$$

where $\partial\delta_\varphi/\partial l$ is referred to as the pitch angle deviation gradient and the gas path angle gradient is written in terms of the absolute coordinate system. Analogously to the normal force case, a modification for numerical stability is added for the binormal force model formulation,

$$\begin{aligned} f_h = & w^2 \cos\beta \left(\left(\frac{\partial \varphi_{GP}}{\partial x} \cos\varphi + \frac{\partial \varphi_{GP}}{\partial r} \sin\varphi \right) \cos\beta + \frac{\partial \delta_\varphi}{\partial l} \right) - \frac{w^2}{r} \cos\varphi \left(1 + \sin^2\beta\right) \\ & - 2\Omega^2 r \cos\varphi - 4\Omega w \cos\varphi \sin\beta. \end{aligned} \tag{4.10}$$

The inputs into the binormal force model are the geometric gas path angle gradients and the pitch angle deviation gradient. The pitch angle deviation gradient represents the deviation of the flow from the local gas path angle, primarily caused by the pressure driven radial flows in the blade passage stemming from the tip clearance flows. Similarly to the normal and parallel force empirical terms, the pitch angle deviation gradient is obtained throughout the blade domain using pitchwise-averaged RANS calculations by solving Equation 4.10 for $\partial\delta_\varphi/\partial l$.

4.1.4 Blade Metal Blockage Model

The blade metal blockage model captures the change in cross sectional area due to the presence of the blades. The model is based on the ratio between the circumferential blade gap and the blade pitch, termed the passage free area ratio, B,

$$B(x,r) = 1 - \frac{t(x,r)}{\cos\kappa(x,r)} \frac{N_B}{2\pi r}, \tag{4.11}$$

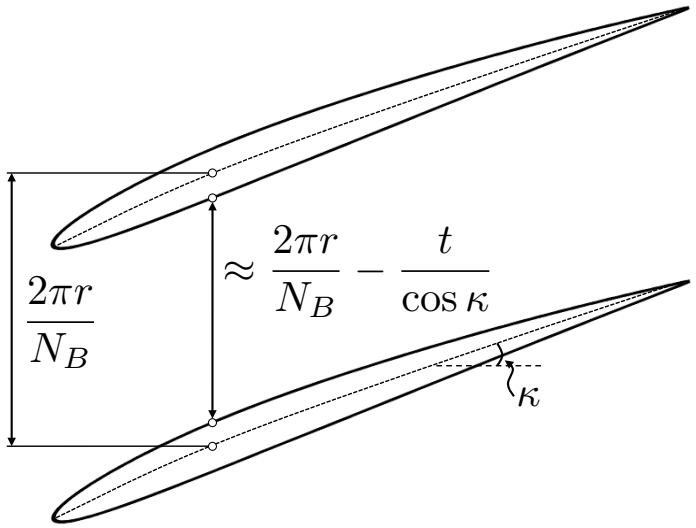


Figure 4-1: Circumferential blade gap and blade pitch, defining passage free area ratio, B, adapted from [37].

where t is the blade thickness normal to the blade's centerline and N_B is the number of blades. The passage free area ratio is diagrammed in Figure 4-1. The model is implemented as a source term in the continuity equation, which adds mass to the flow to account for the area change,

$$S_m = -\rho \frac{1}{B} \left(w_x \frac{\partial B}{\partial x} + w_r \frac{\partial B}{\partial r} \right). \tag{4.12}$$

4.1.5 Analytical Representation of Empirical Terms

To allow the forces to respond to the local flow field, the empirical terms of the force formulations are analytically represented. For every (x, r) grid point, the three empirical terms, $\partial\delta_\beta/\partial l$, $\partial s/\partial m$, and $\partial\delta_\varphi/\partial l$, are calculated along the characteristic. A second order fit is calculated as a function of the local relative flow velocity magnitude, as sketched in Figure 4-2. For example, the relative flow angle deviation gradient at a point (x, r) is represented as

$$\frac{\partial\delta_\beta}{\partial l} = C_1 w^2 + C_2 w + C_3, \tag{4.13}$$

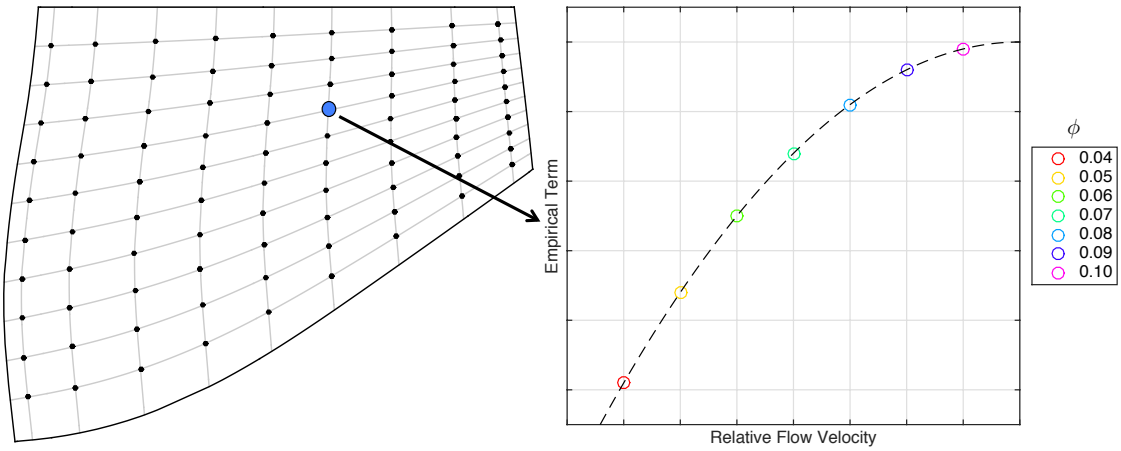


Figure 4-2: Analytical representation of an empirical term for a single (x, r) grid point.

where C are the polynomial coefficients calculated for that grid point from the fitted curve for the deviation gradients throughout the characteristic.

4.1.6 Model Convergence Issues

The model was implemented within the same framework as the steady, axisymmetric cases outlined in Section 3.3.1. The same mesh and boundary conditions were used. The force formulations were implemented using CFX's built-in user-defined functions, termed the CFX Expression Language (CEL). The inputs into the force equations, namely the empirical term fits and the geometry terms, were implemented using CFX's user-defined interpolation functions on the body force extraction grid. The calculated natural coordinate forces feed into the Fortran functions that transform the forces into the cylindrical coordinate system to be input as momentum source terms. The blockage model mass source term is input using CEL. The working fluid was water at 25°C. The full model is initialized with the steady, axisymmetric solution for the given operating point.

Upon implementation of the full blade passage model, convergence issues were encountered. Figure 4-3 shows an iteration-by-iteration view of spurious recirculation regions developing in the flow field for $\phi = 0.07$. The calculation eventually stops at iteration 30 with flow exiting the inlet and entering the outlet.

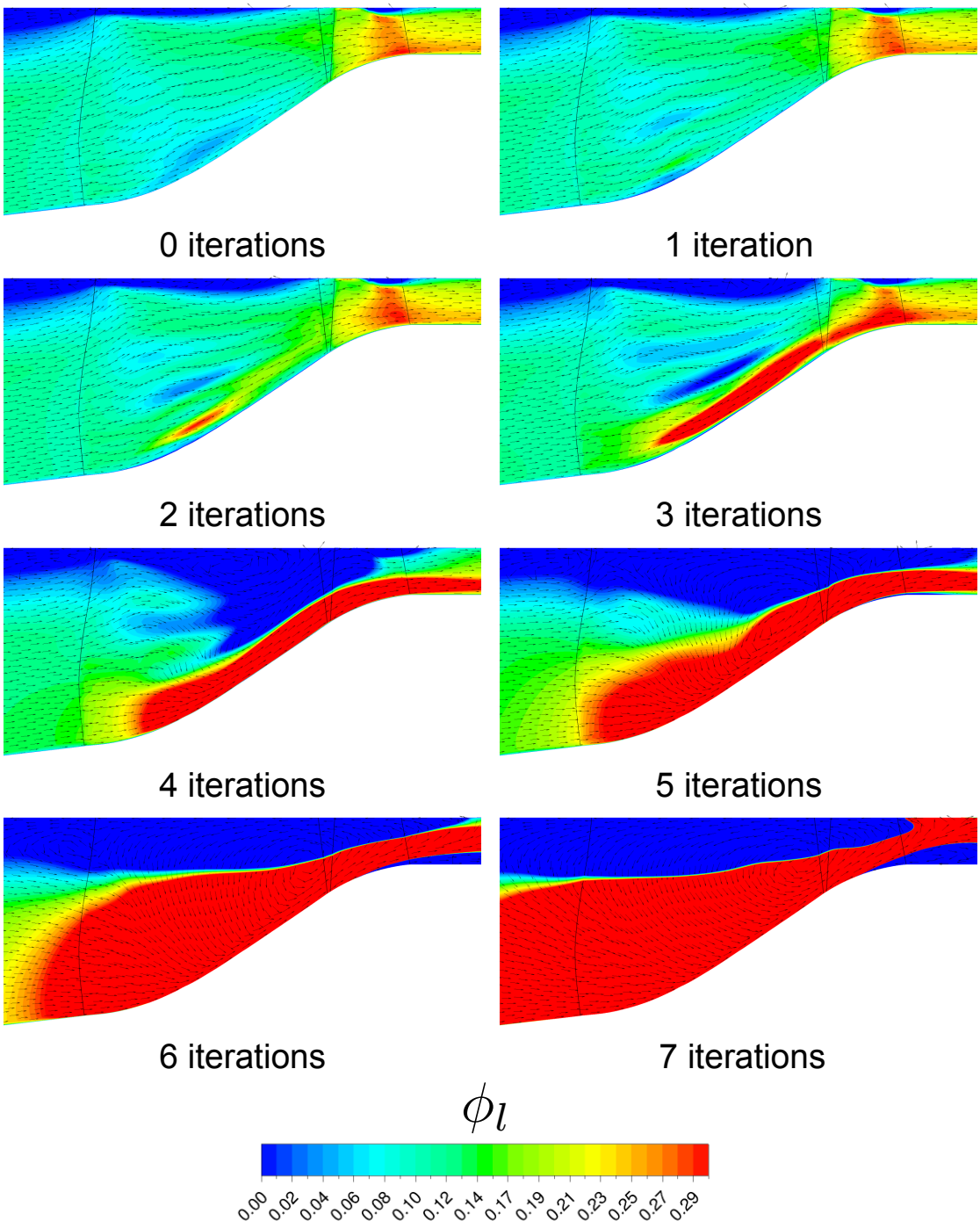


Figure 4-3: Formation of spurious recirculation regions in inducer body force model for $\phi = 0.07$. Contours of axial velocity nondimensionalized by tip speed.

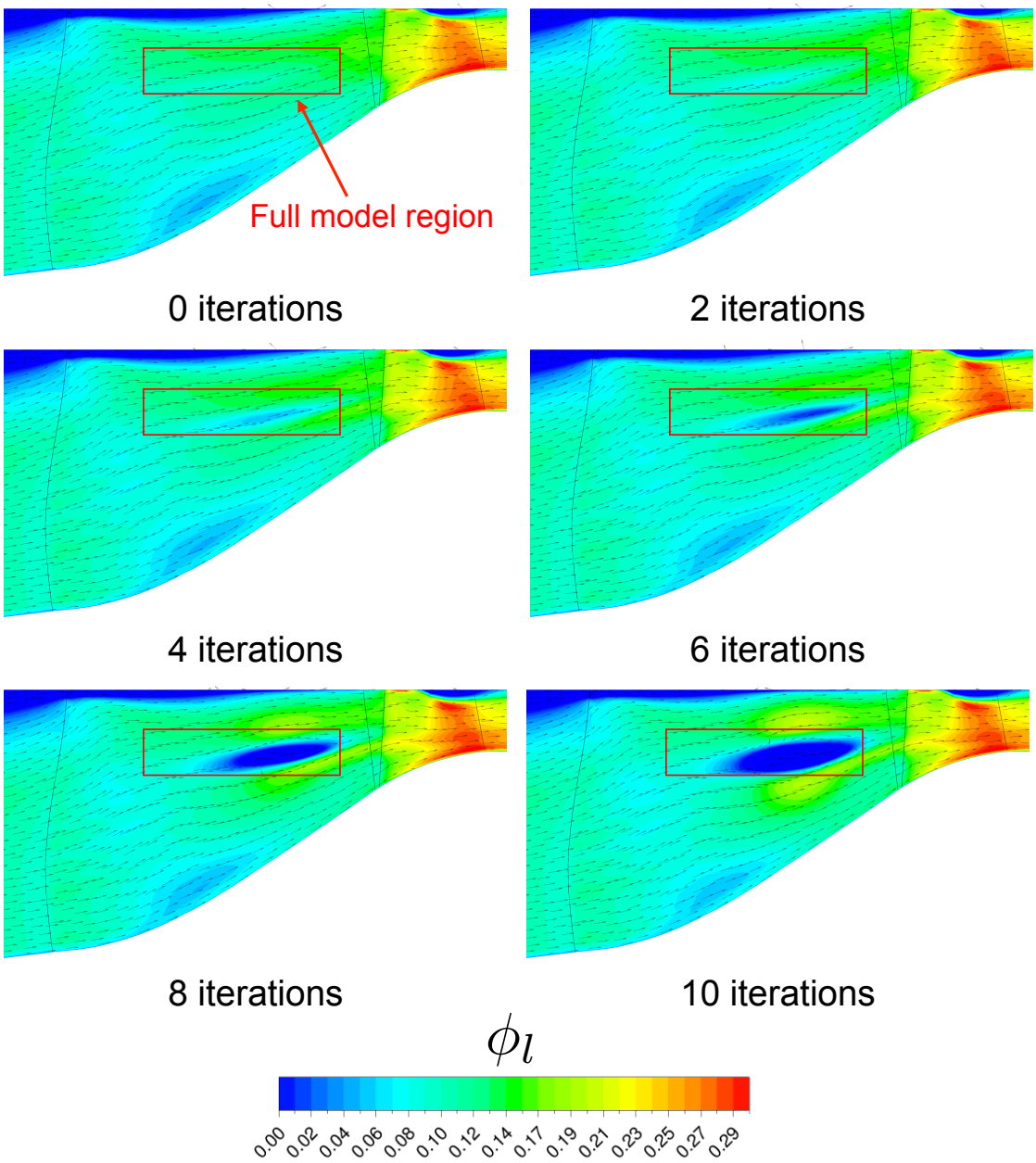


Figure 4-4: Development of spurious recirculation region only within full model region (outlined in red) for diagnostic test case at $\phi = 0.07$. Contours of axial velocity nondimensionalized by tip speed.

A diagnostic test case was run at $\phi = 0.07$ to isolate the model from tip leakage and endwall effects. A region within the middle of the inducer blade passage was allowed to run with the full model, while the pitchwise-averaged RANS extracted forces was directly input (i.e. axisymmetric, time-invariant, and unable to respond to changes in the flow field) for the rest of the blade domain, including the kicker.

As seen in Figure 4-4, the spurious recirculation regions formed only within the full model window, outlined in red. Given the solution is initialized with the steady, axisymmetric solution and the full model region is isolated away from tip leakage flows, endwalls, and the leading and trailing edges, the diagnostic results suggest the forces are sensitive to small perturbations in the flow field as the calculation iterates, i.e. the model is sensitive.

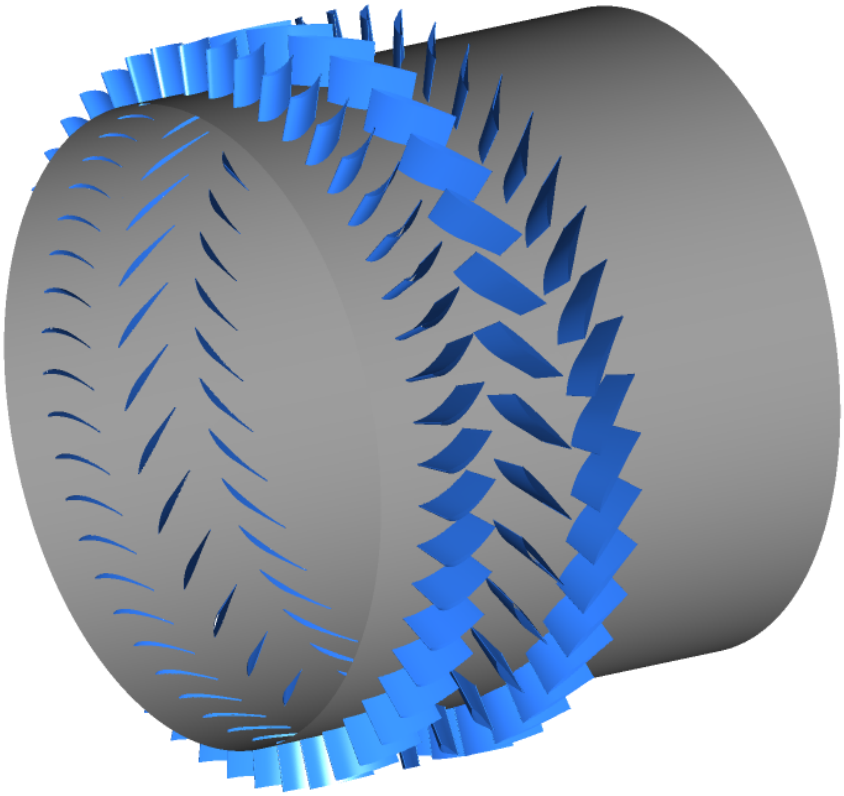
4.2 Low Speed Axial Compressor Model Validation Case

Sorensen's blade passage model was implemented in a low speed axial compressor (LSAC) to validate model assumptions, formulation, and implementation. The LSAC test case revealed a discrepancy in the blockage model, which was remedied with a blockage correction parameter. The corrected model was able to capture stalled conditions in the LSAC, testifying to the model's robustness. The successful LSAC case shows Sorensen's model formulation itself is sound and confirms the root cause of the convergence issues is the inducer geometry itself.

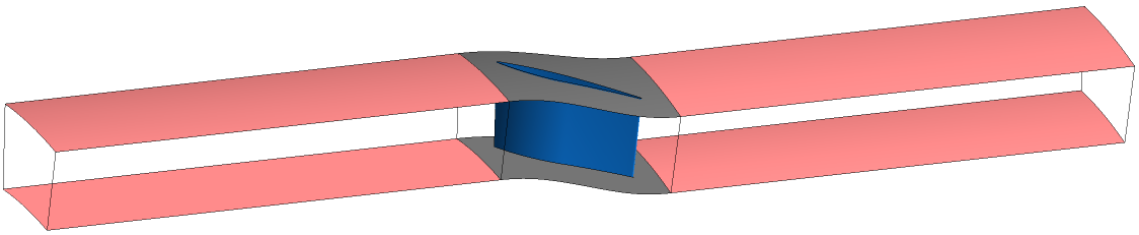
4.2.1 Low Speed Axial Compressor Geometry

A single stage compressor with an inlet guide vane (IGV), shown in Figure 4-5a, was used as the validation test case. For the purposes of the body force calculation, the rotor was isolated, shown in Figure 4-5b, with design details shown in Table 4.1. The representative compressor geometry has no leading edge backsweep, no blade cant, low stagger angles, and no tip gap (i.e. a shrouded rotor). The LSAC geometry is reflective of previous applications of the body force model, where negligible radial flows was a common assumption [36, 46, 47].

Similar to the MIT inducer CFD calculations, the LSAC steady CFD simulations were single-passage RANS calculations run using ANSYS CFX and its k-ω SST turbulence model. The LSAC mesh is approximately 400,000 elements, made using ANSYS



(a) Low speed single stage axial compressor with inlet guide vane.



(b) Isolated single-passage rotor. No-slip boundary conditions are used in the blade domain, while free-slip walls are used for the inlet and outlet hub and shroud, marked in red. The inlet boundary condition imparts inlet swirl matching the outlet of the IGV.

Figure 4-5: Low speed axial compressor geometry used for validation test case.

Table 4.1: Low speed axial compressor rotor design data.

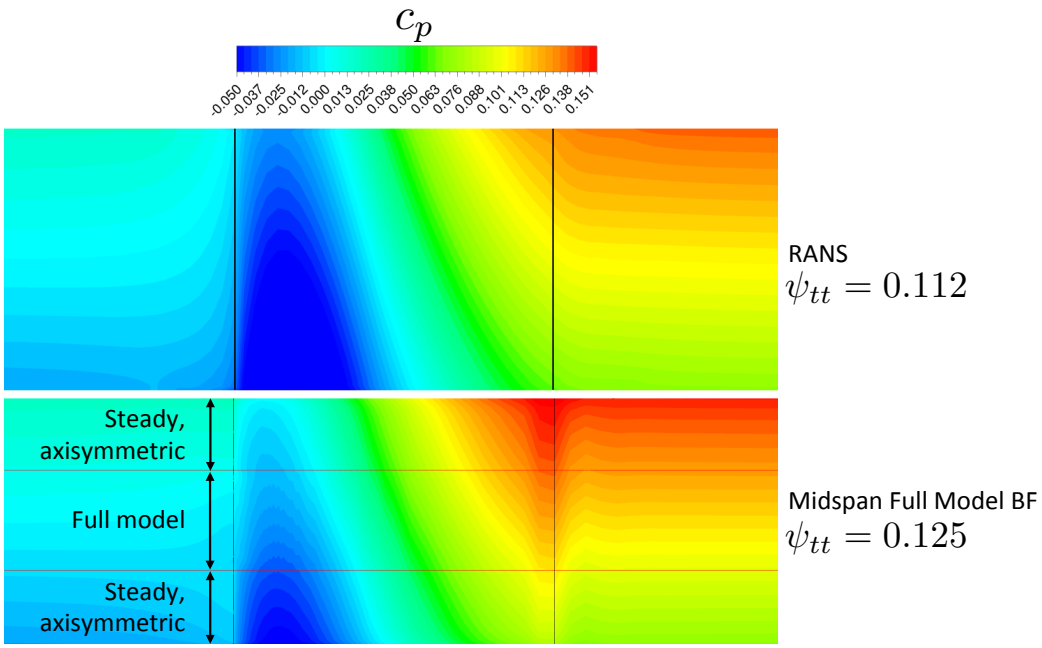
Design flow coefficient	0.385
Design total-to-total head coefficient	0.112
Number of rotor blades	32
Inlet hub-to-tip ratio	0.87
Outlet hub-to-tip ratio	0.87
Inlet blade angle at tip	55.6°
Outlet blade angle at tip	45.2°
Leading edge backsweep	0°
Inlet tip gap relative to span	0

Turbogrid. The inlet was placed a half-diameter upstream of the rotor leading edge with a total pressure boundary condition and a prescribed inlet flow angle matching the outlet flow angle of the IGV. The outlet was placed a half-diameter downstream of the rotor trailing edge with a normal velocity boundary condition, setting the flow coefficient. No-slip wall boundary conditions were used for the blades, hub, and shroud in the blade domain. In the inlet and outlet domains, free-slip walls were used for the hub and shroud to match the flow entering the rotor from the IGV and exiting into the stator. The working fluid was constant density air.

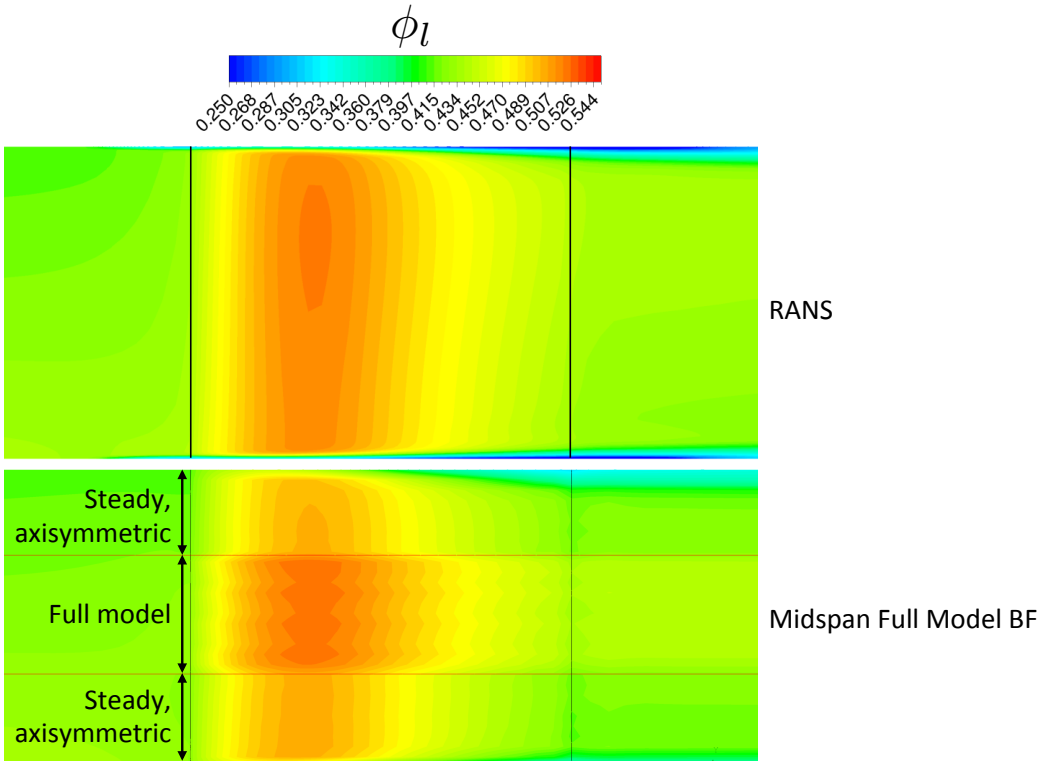
The LSAC body force model was also implemented in ANSYS CFX. Consistent with the MIT inducer body force mesh, the LSAC body force mesh geometry consists of the hub and shroud lines forming a 20° wedge of 600,000 elements with periodic boundary conditions. The inlet and outlet placement as well as their respective boundary conditions were the same as in the single-passage calculations. The body force model was implemented using the same CFX functionality as described in Sections 3.3.1 and 4.1.6 for the steady, axisymmetric forces calculation and full model calculations, respectively.

4.2.2 Aerodynamic Blockage Correction

The full model implementation of Sorensen's blade passage model for the axial compressor rotor resulted in spurious recirculation and convergence issues, qualitatively similar to those observed in the inducer body force model. A diagnostic test case



(a) Pressure coefficient



(b) Axial velocity, nondimensionalized by tip speed

Figure 4-6: Offset of velocities in midspan full model region in body force model at design point, $\phi = 0.385$, suggesting blockage model does not capture aerodynamic blockage.

was likewise conducted at design point, $\phi = 0.385$, where a midspan region of the LSAC was ran full model while areas near the hub and shroud were left axisymmetric and time-invariant. The diagnostic test case converged, with results shown in Figure 4-6. Notably, the results indicate an offset of flow velocities within the full model region from the expected pitchwise-averaged RANS velocities, which results in the calculated body forces being correspondingly offset from their expected values and an overprediction of pressure rise. Similar diagnostic cases where instead the hub and/or shroud were run full model exhibited convergence issues.

Based on the diagnostic results, it was hypothesized that the blockage model does not capture aerodynamic blockage from flow features such as boundary layer displacement and separation, leading to an offset for the full model velocities seen in Figure 4-6. The midspan full model calculation was able to converge while the hub and shroud test cases failed due to the larger aerodynamic blockage effects from boundary layers near endwalls. Based on Brand's work [46], a blockage correction to the Sorensen blockage model was implemented to account for aerodynamic blockage. The correction is calculated for all grid points within the blade domain,

$$\Delta w = w_{RANS} - w_{BF}, \tag{4.14}$$

where w_{RANS} is the pitchwise-averaged RANS relative velocity magnitude and w_{BF} is the relative velocity magnitude from the steady, axisymmetric calculation, both taken at design point. The original (uncorrected) blockage model is implemented in the steady, axisymmetric calculations and as a result the aerodynamic blockage is not captured – however, since the forces are not calculated from querying the flow field, the impact on the results of not capturing aerodynamic blockage is negligible. Figure 4-7 shows the difference between the pitchwise-averaged RANS and uncorrected body force model relative velocities. As expected, the highest discrepancies are near the endwalls where boundary layer effects cause aerodynamic blockage.

The same blockage correction distribution is implemented in the body force calculation for all operating points by adding onto the relative flow velocity input into

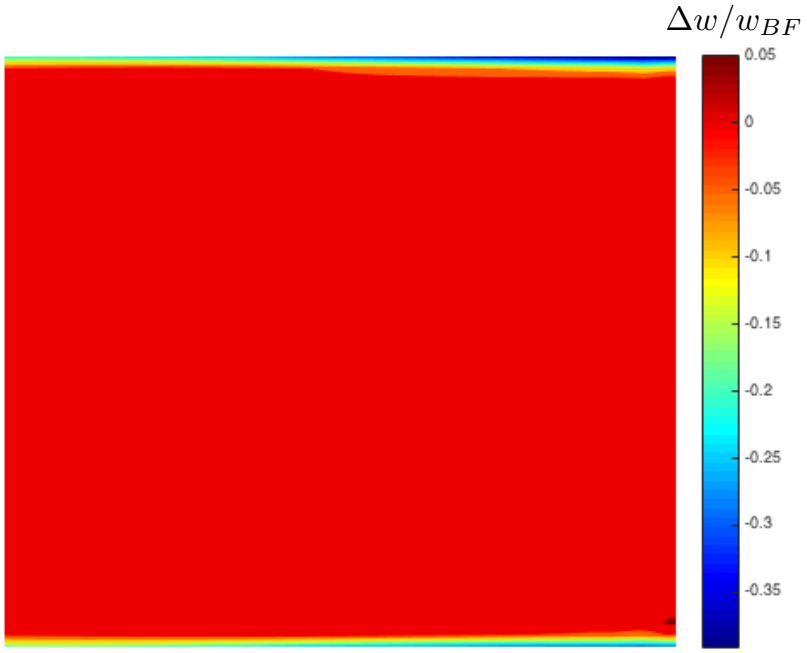


Figure 4-7: Largest difference between pitchwise-averaged RANS and body force model relative velocities are near the endwalls, where boundary layer effects cause aerodynamic blockage.

the forces,

$$\mathbf{f} = f(w + \Delta w, \beta, \varphi, \text{geometry}, \text{empirical term fits}). \tag{4.15}$$

Note that the original blockage model is still implemented – the blockage correction is added, thereby "correcting" the blockage model to the pitchwise-averaged RANS relative velocities to be input into the force equations.

4.2.3 Application of Aerodynamic Blockage to Axial Compressor Rotor Case

With the blockage correction, the LSAC full model calculation is able to converge, successfully capturing the pitchwise-averaged RANS flow field and performance across the characteristic. A comparison of head coefficient between single-passage RANS, axisymmetric time-invariant calculations, and the full model calculations is shown in Figure 4-8, with a 7% maximum difference between the body force calculations and RANS. Notably, the body force calculations are able to converge at near stall

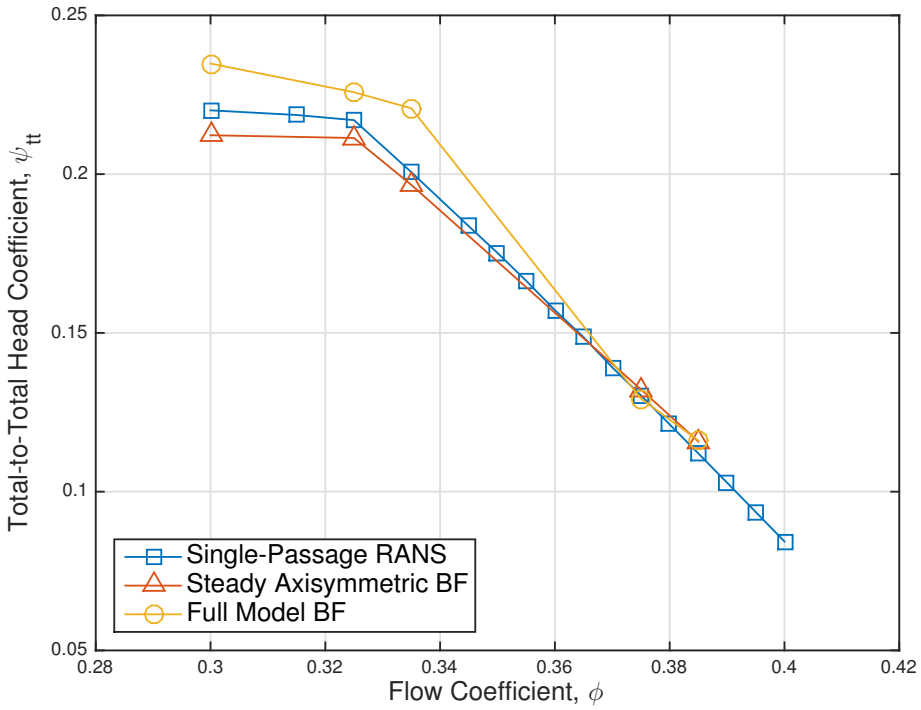
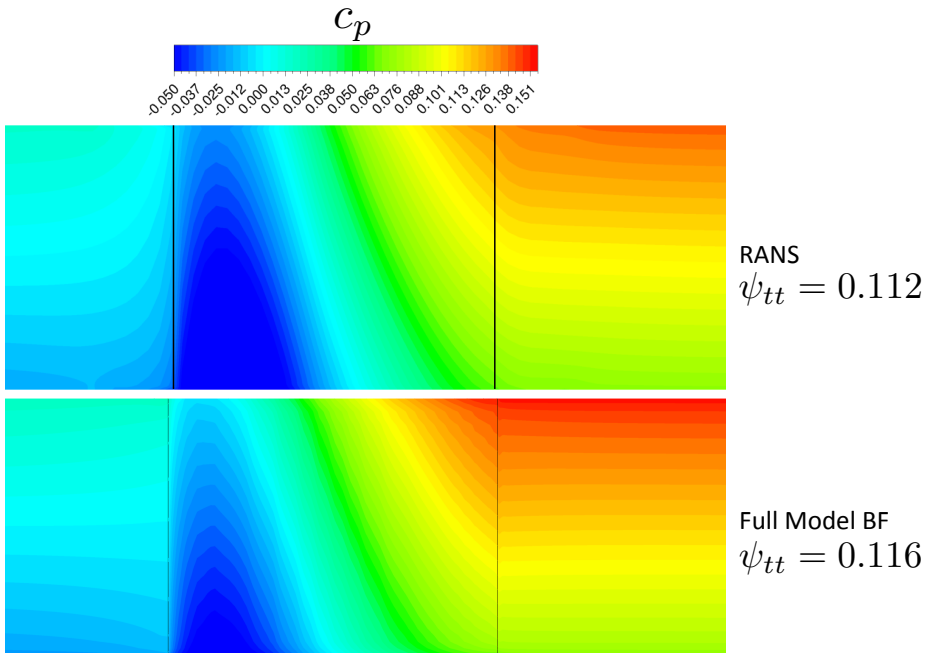


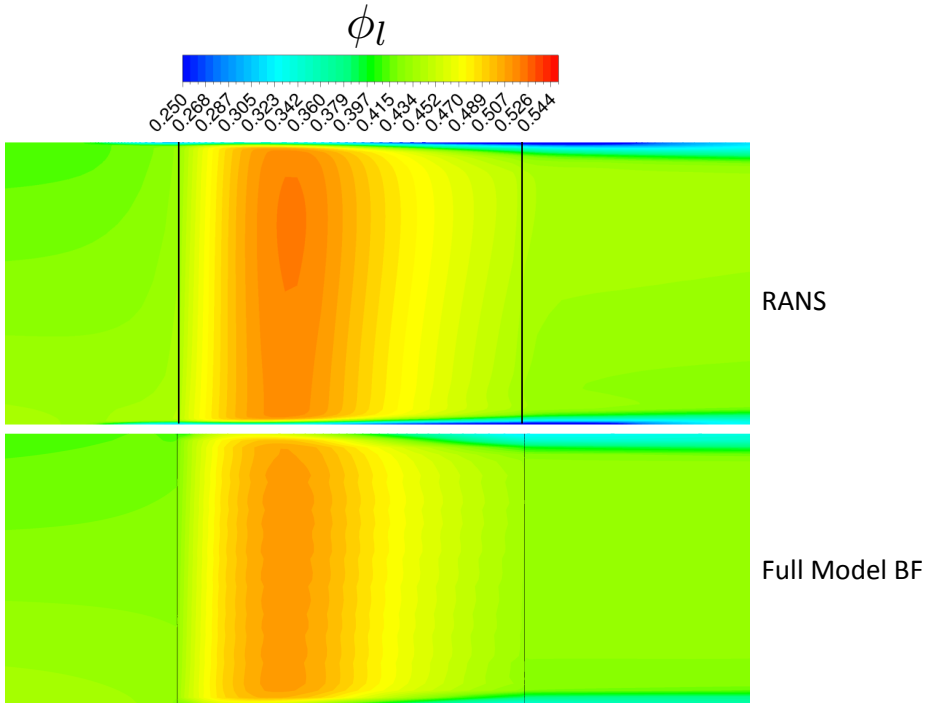
Figure 4-8: LSAC RANS and body force characteristics.

conditions, where there is substantial amounts of separation and the slope of the characteristic is close to zero.

A comparison of the flow field and pressure field at design, $\phi = 0.385$, between RANS and the full model body force calculation is seen in Figures 4-9 and 4-10, indicating good agreement between RANS, axisymmetric time-invariant forces, and full model body forces. The full model captures the axisymmetric time-invariant flow field with a slight offset from RANS, reflecting the presence of the blockage correction – note that while the velocity input into the force formulations have the blockage correction, the actual flow field in the blade domain, as plotted in Figure 4-10, does not see the corrected velocities. The forces are therefore the extracted forces, but the flow field will always be slightly offset from RANS. Indicatively, the discrepancy between the steady, axisymmetric forces and the full model are highest at the tip and hub, near the endwalls, where blockage correction plays the largest role.

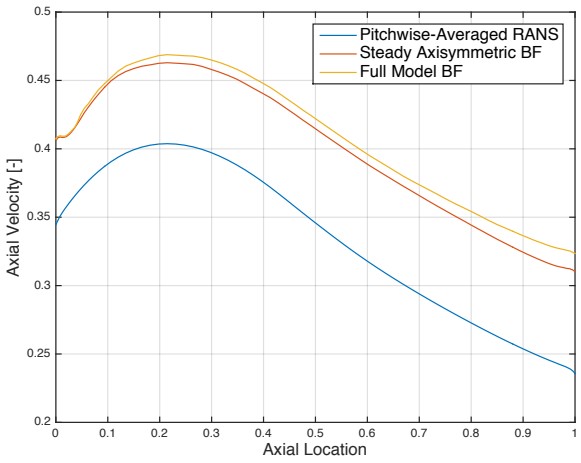


(a) Pressure coefficient

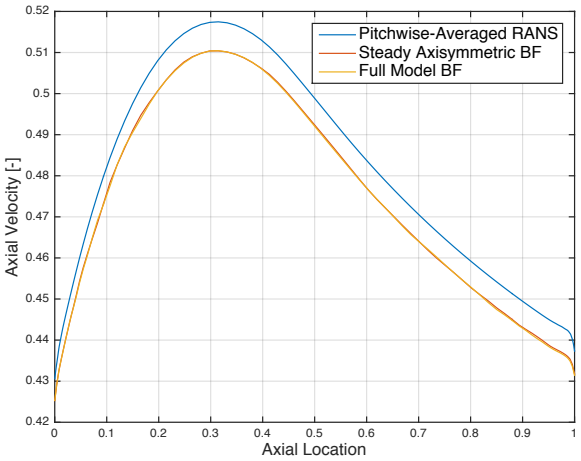


(b) Axial velocity, nondimensionalized by tip speed

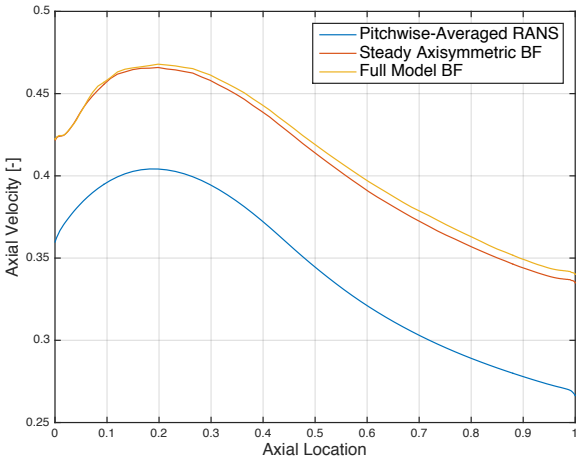
Figure 4-9: LSAC full model (with blockage correction) results compared with pitchwise-averaged RANS at design point, $\phi = 0.385$.



(a) Tip

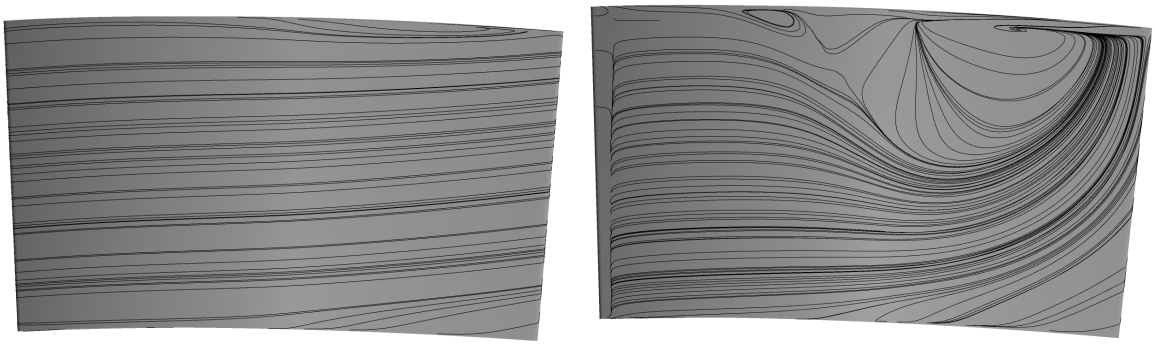


(b) Midspan



(c) Hub

Figure 4-10: Streamwise axial velocity distributions throughout the LSAC blade domain at design point, $\phi = 0.385$. Offset of the body force calculations from RANS is a consequence of the blockage correction. Velocity is nondimensionalized by tip speed.



(a) $\phi = 0.385$, design point (b) $\phi = 0.300$

Figure 4-11: LSAC suction side limiting streamlines indicating substantial separation at $\phi = 0.300$.

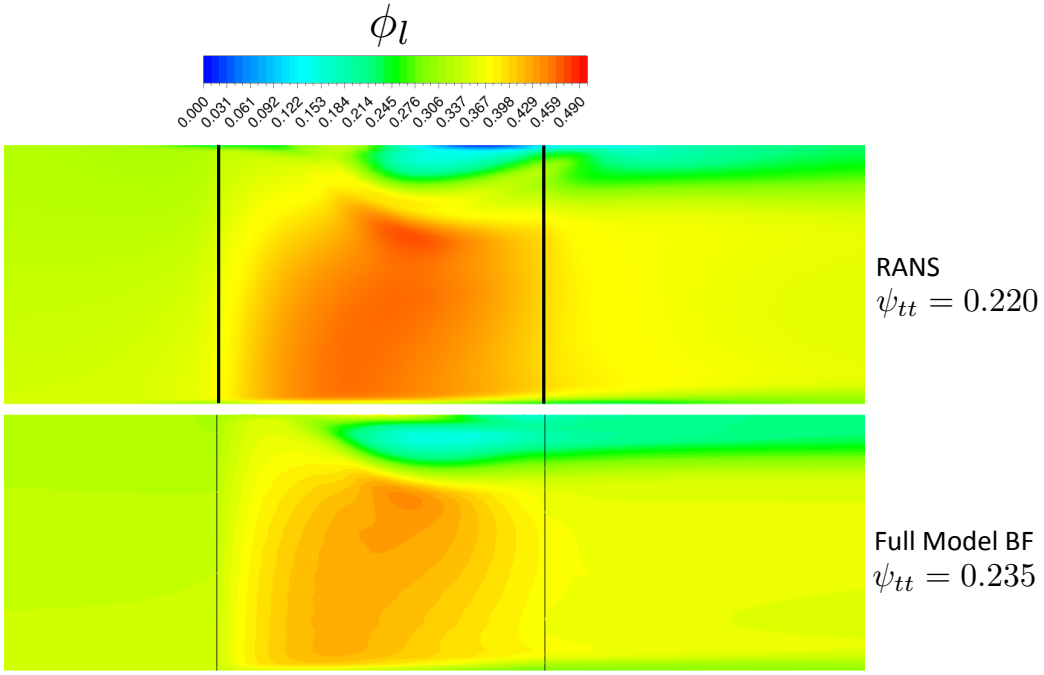
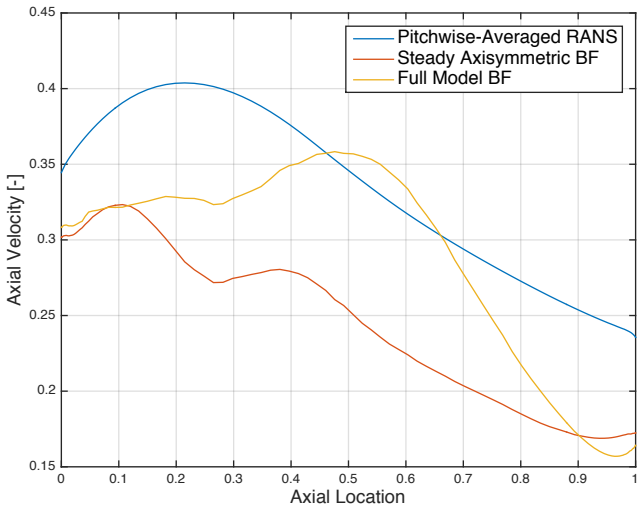
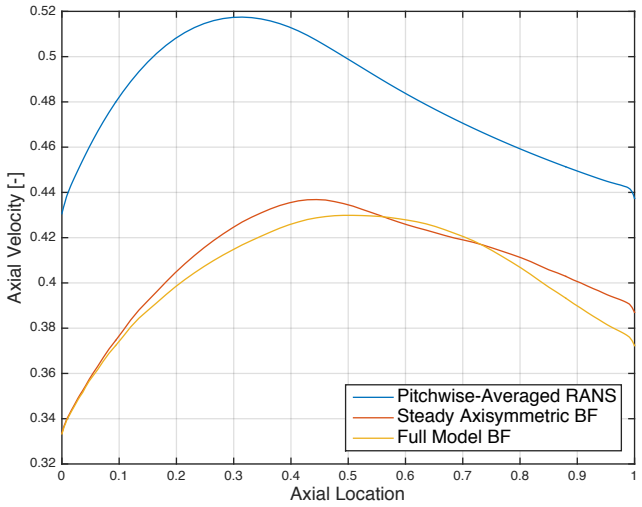


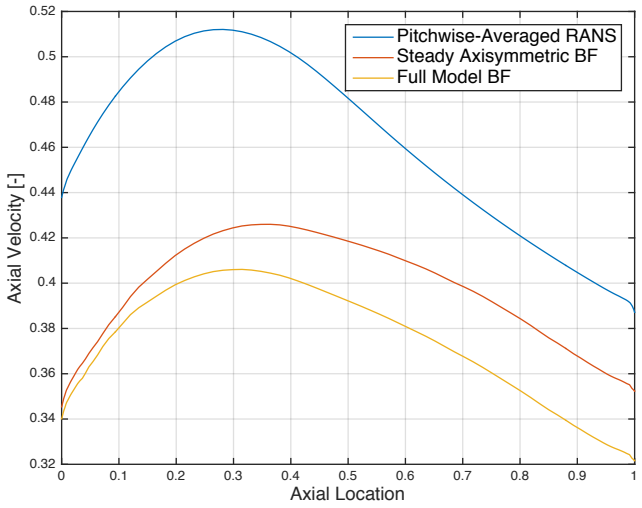
Figure 4-12: The body force model is able to capture the separated flow field at near stall conditions, $\phi = 0.300$. Contours of axial velocity nondimensionalized by tip speed.



(a) Tip

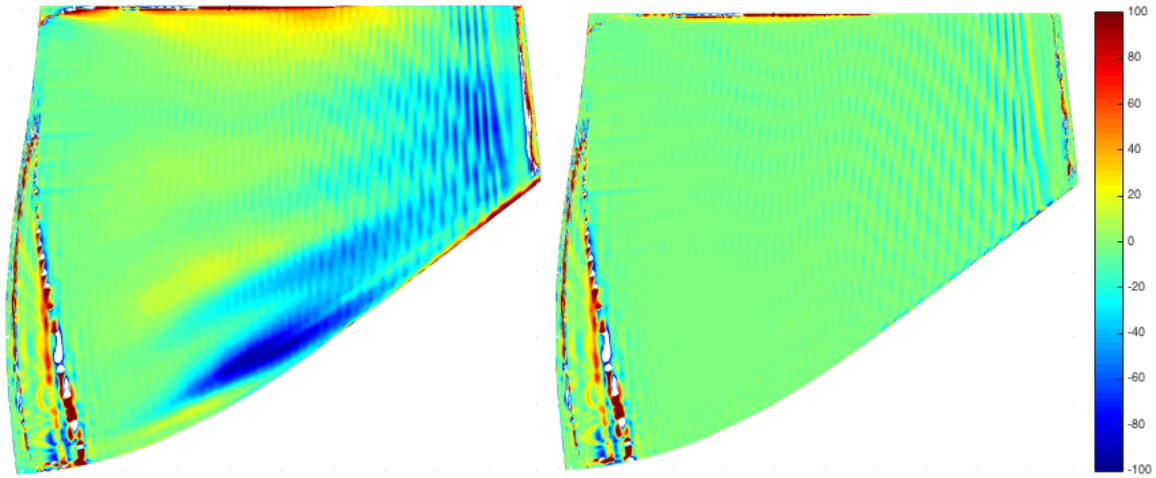


(b) Midspan



(c) Hub

Figure 4-13: Streamwise axial velocity distributions throughout the LSAC blade domain at stalled conditions, $\phi = 0.300$.



(a) Without blockage correction (b) With blockage correction

Figure 4-14: Blockage correction reduces difference (in percent) of calculated forces from pitchwise-averaged RANS extracted forces, but inducer model still experiences convergence issues.

To investigate the robustness of the correct blade passage model by Sorensen, an operating point in stalled conditions, $\phi = 0.300$, was tested. The suction side limiting streamlines are compared between design point and $\phi = 0.300$ in Figure 4-11, indicating substantial tip separation at the lower flow coefficient as well as hub separation. The body force results are compared with the pitchwise-averaged RANS results in Figures 4-12 and 4-13. The body force model is able to qualitatively capture the flow field, including the separation region, as well as capture the global performance within 7%.

Sorensen's blade passage model formulation is able to converge and capture the flow field of the LSAC across its characteristic, a geometry reflective of previously successful body force modeling applications. It is also able to capture the large separated flow field at near stall conditions, suggesting the model is robust.

4.3 Body Force Modeling Challenges for Inducer Geometries

The implementation of the blockage correction in the MIT inducer body force model did not remedy the convergence issues despite the correction greatly reducing errors in the calculated force throughout the inducer domain, as seen in Figure 4-14. Figure 4-14 was calculated using the steady, axisymmetric calculation flow field with and without the blockage correction to calculate and compare the forces. The success and demonstrated robustness of the Sorensen body force model in the low speed axial compressor geometry suggests the convergence issues are a consequence of the inducer geometry itself. The hypothesized cause of model sensitivity, the sensitivity of stagnation pressure loss to incidence, is verified by comparing the performance and geometry characteristics of the inducer against the compressor.

4.3.1 MIT Inducer vs. LSAC: Performance and Geometry Comparison

Performance of turbomachines is typically characterized by its characteristic (as shown previously) as well as the loss through the turbomachine. The lost work (i.e. inefficiency) is calculated using the stagnation pressure loss coefficient, ω, which captures total pressure loss from leading edge to trailing edge,

$$\omega = \frac{p_{t,rel_1} - p_{t,rel_2}}{\frac{1}{2}\rho w_1^2}, \tag{4.16}$$

where $p_{t,rel}$ is the mass averaged total pressure in the relative frame. To account for the effects of radius change, such as from that of the MIT inducer hub line, the reduced total pressure is used instead,

$$p_{t_{red}} = p + \frac{1}{2}\rho w^2 - \frac{1}{2}\rho\left(\Omega r\right)^2, \tag{4.17}$$

which bookkeeps the work done by centrifugal forces [50].

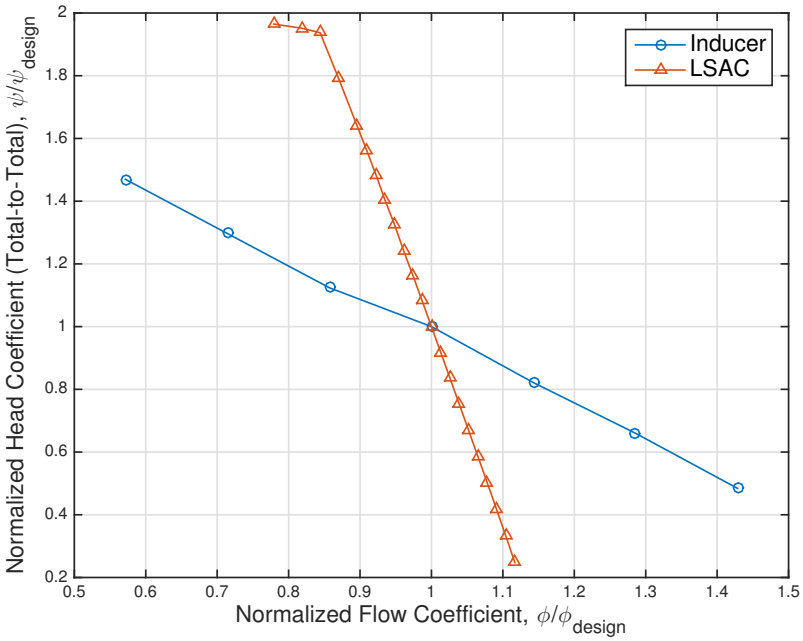


Figure 4-15: Comparison of MIT inducer and LSAC characteristics.

A comparison between the performance characteristics of the MIT inducer and LSAC, shown in Figure 4-15, is not particularly noteworthy, and likewise when comparing the stagnation pressure loss as a function of flow coefficient, shown in Figure 4-16. In both cases, the inducer and compressor both follow the expected trends.

However, comparing loss coefficient as a function of the incidence itself is more revealing. Incidence is the relevant independent variable, as evidenced by the variation of the loss bucket at different spanwise locations, seen in Figure 4-17. For the midspan and hub sections, the inducer loss buckets are markedly narrower due to the smaller variation in incidence across an approximately equal global flow coefficient range. To find the cause behind the difference in loss buckets, the design differences between the two geometries are compared side-by-side by reproducing Tables 2.1 and 4.1 in Table 4.2. The tip gap, leading edge backsweep (which serves to increase the effective tip gap for the inducer), and stagger angles are the primary differences. The similarity seen in Figure 4-17c between the inducer and the LSAC suggests that in the context of loss buckets, the tip geometry differences are relatively inconsequential. However, the midspan and hub loss buckets indicate the differences in stagger angle are significant.

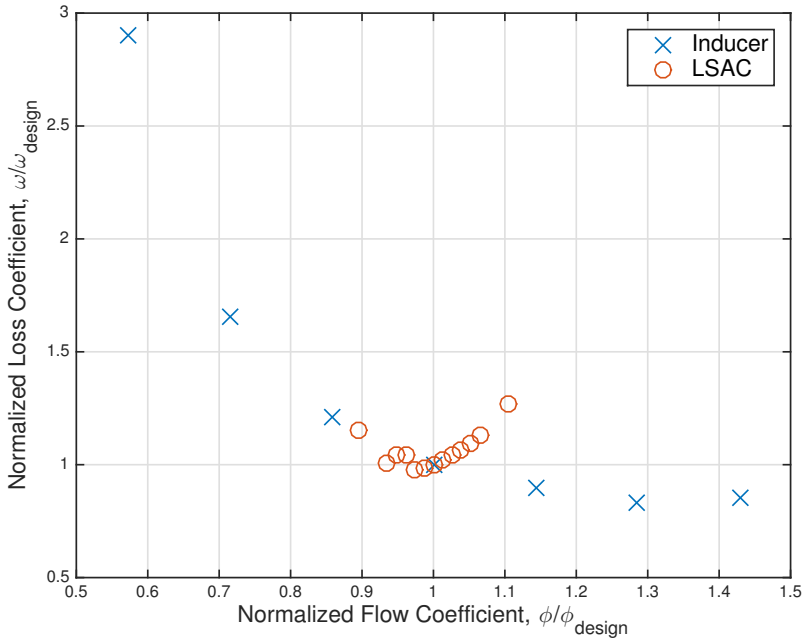
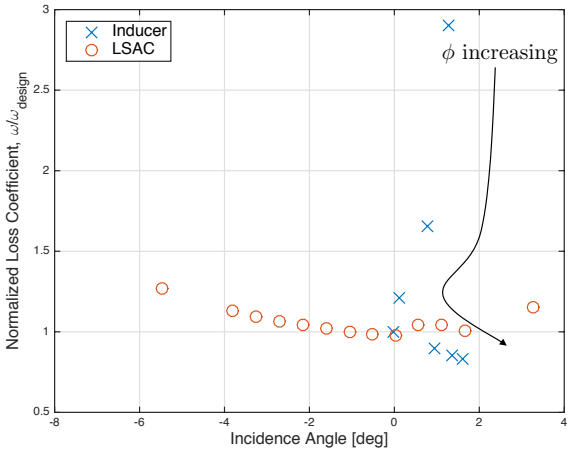


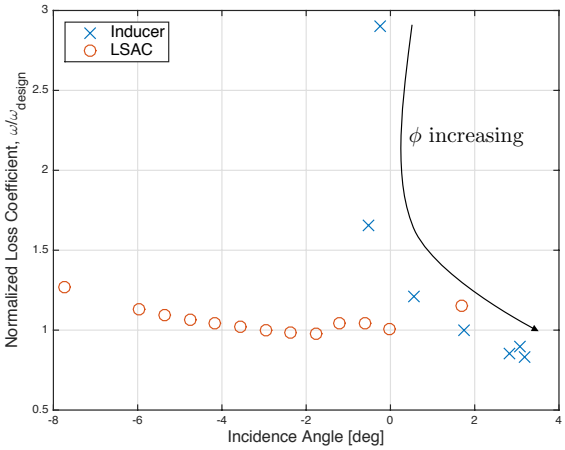
Figure 4-16: Comparison of MIT inducer and LSAC loss as a function of flow coefficient, suggesting the inducer follows expected trends.

Table 4.2: Comparison of inducer against LSAC geometry.

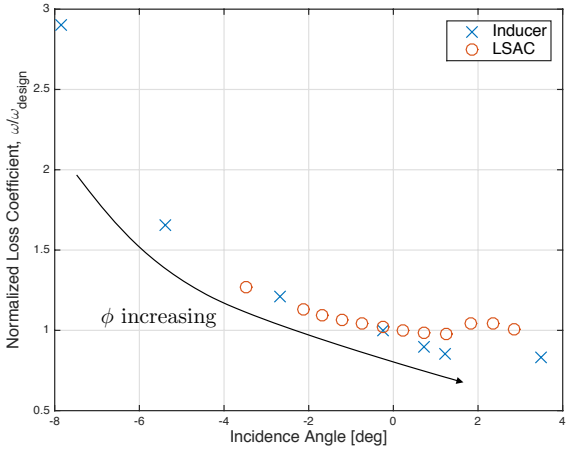
	MIT Inducer	LSAC Rotor
Design flow coefficient	0.07	0.385
Design total-to-total head coefficient	0.35	0.112
Number of rotor blades	4	32
Inlet hub-to-tip ratio	0.29	0.87
Outlet hub-to-tip ratio	0.72	0.87
Inlet blade angle at tip	82.7°	55.6°
Outlet blade angle at tip	74°	45.2°
Leading edge backsweep	120°	0°
Inlet tip gap relative to span	0.01	0



(a) Midspan

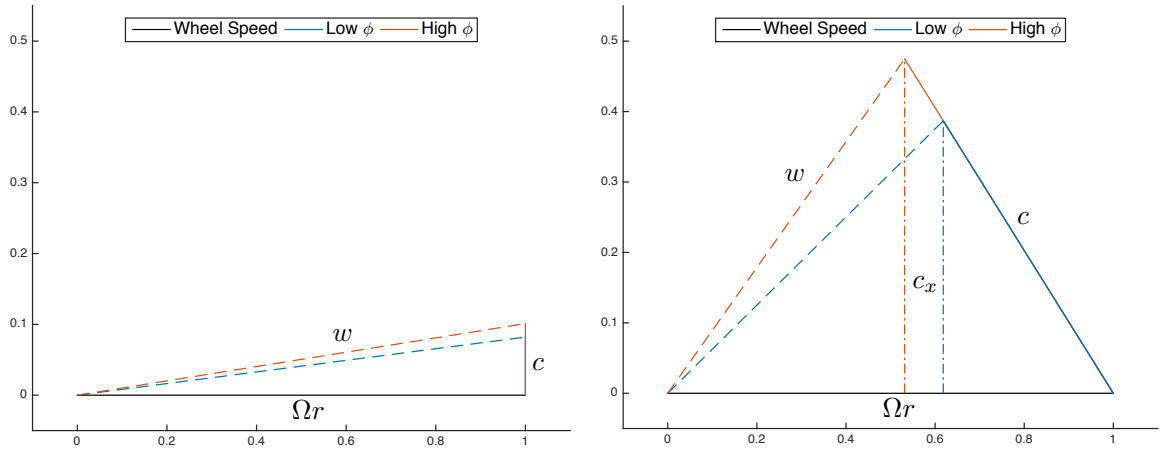


(b) Hub



(c) Tip

Figure 4-17: Comparison of loss buckets at different spanwise locations of the MIT inducer and LSAC.



(a) Inducer (b) LSAC

Figure 4-18: Changes in nondimensional inlet midspan velocity triangle for the same change in flow coefficient. The change is markedly smaller for the inducer due to the highly tangential flow. c denotes absolute velocity.

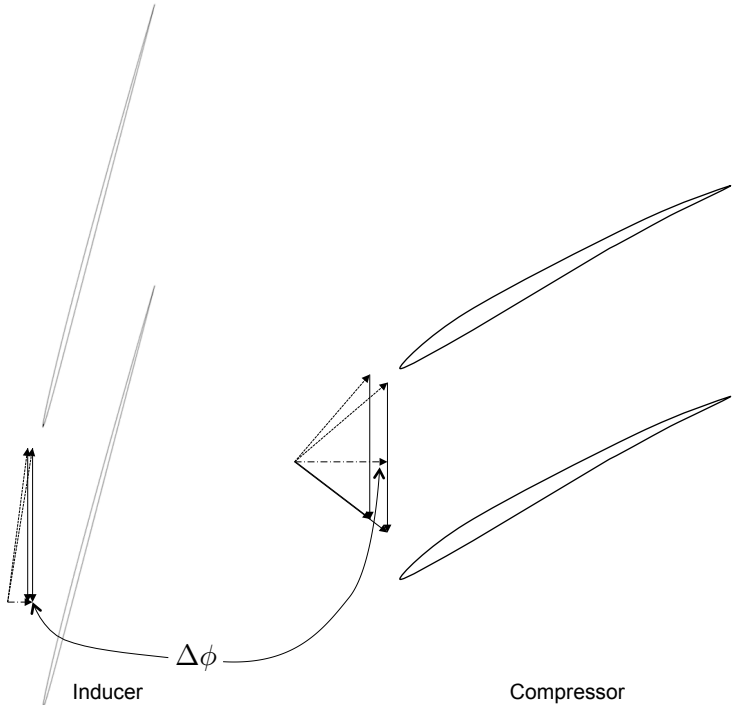


Figure 4-19: High stagger angles cause narrow loss buckets due to nearly tangential flow imposed in inducer blade domain. The same absolute change in flow coefficient causes a much smaller change in incidence for the inducer than the compressor.

The low flow coefficient design and the associated high stagger angles of the inducer are the drivers behind the sensitivity of stagnation pressure loss to incidence. Inlet velocity triangles are compared between the inducer and compressor in Figure

4-18 – due to the nearly tangential flow entering the inducer blade domain, for the same change in flow coefficient, the change in incidence is distinctly smaller for the inducer than the compressor, leading to a narrow range of incidence angles, sketched in Figure 4-19.

4.3.2 Radial Flow Redistribution Effects on Incidence Trends

Notably, while the small ranges of incidence are explained by the nearly tangential flow, the trend of incidence with loss coefficient is due to radial flow redistribution. Competing effects from the radial flows generated by tip clearance flow, hub separation, and area contraction cause the loss to be non-monotonic with incidence, as seen at the midspan and hub.

The tip vortex trajectory, previously hypothesized to play a role in rotating cavitation onset, increases blockage as it turns tangential with increasing flow coefficient. The incoming flow is forced radially downwards and decreases incidence near the hub, until the tip vortex trajectory enters the blade passage, alleviating this incidence change. The trend is sketched in Figure 4-20, while experimental evidence from side-view video of the tip vortex trajectory trend is in Figure 4-21.

However, flow separation near the hub increases as the flow coefficient is reduced. Shown in Figure 4-22 in a meridional view, the incoming flow is forced radially upward, which increases local incidence near the tip. The effects of the tip vortex blockage and separation blockage compete, forming the trend seen in the stagnation pressure loss with incidence. The effects diminish in the spanwise direction – at the tip, the flow is primarily determined by the pressure-driven tip clearance flows, whose strength is a monotonic function of the flow coefficient, as indicated by Figure 3-6.

4.3.3 Implication of Stagnation Pressure Loss Sensitivity with Incidence

The small flow angle ranges seen in the narrow loss buckets manifest in the body force model as narrow empirical term characteristics. As a consequence of separation

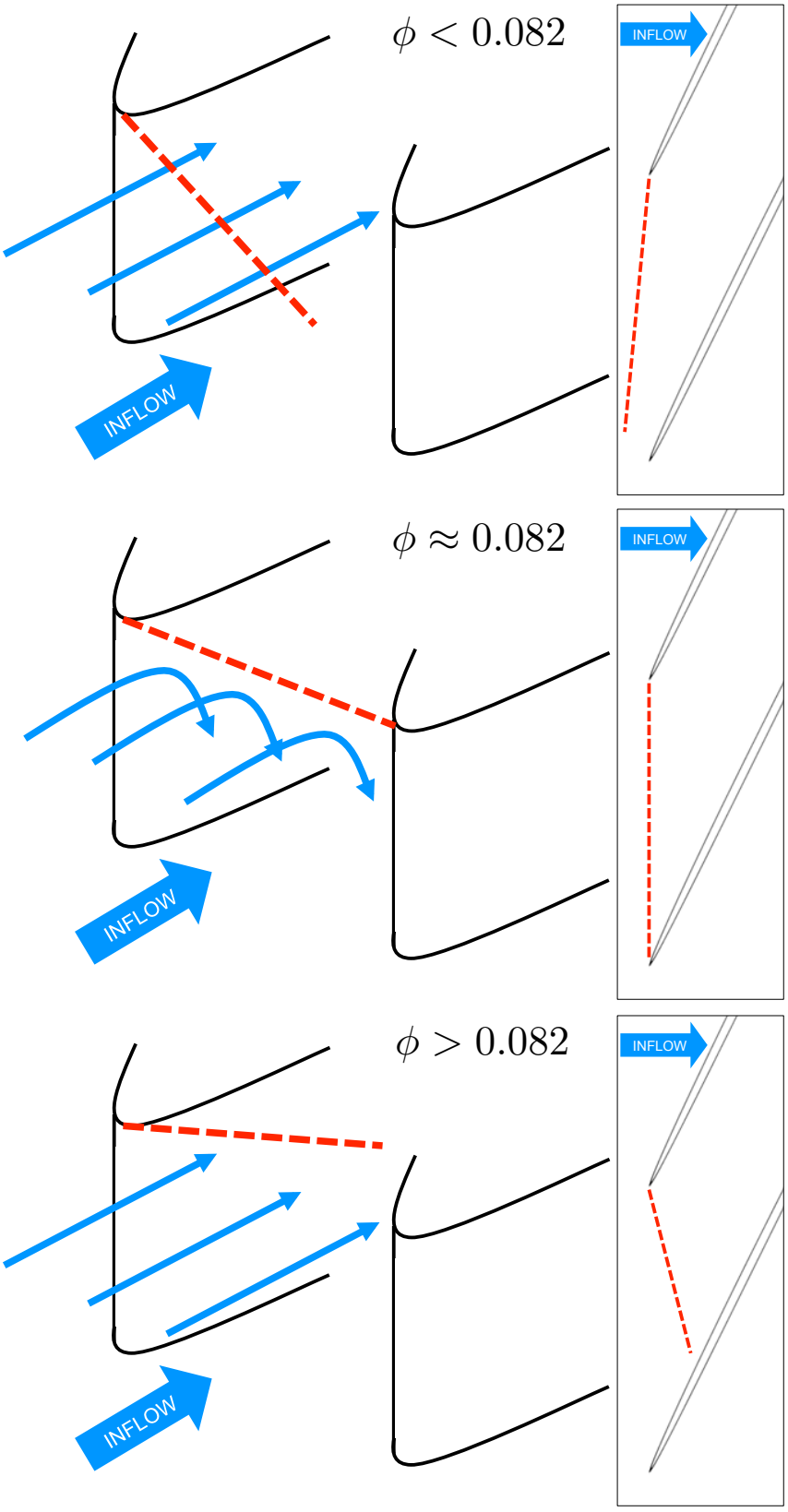


Figure 4-20: Sketch of tip vortex trajectories (in red) and associated radial flow redistribution for varying flow coefficients.

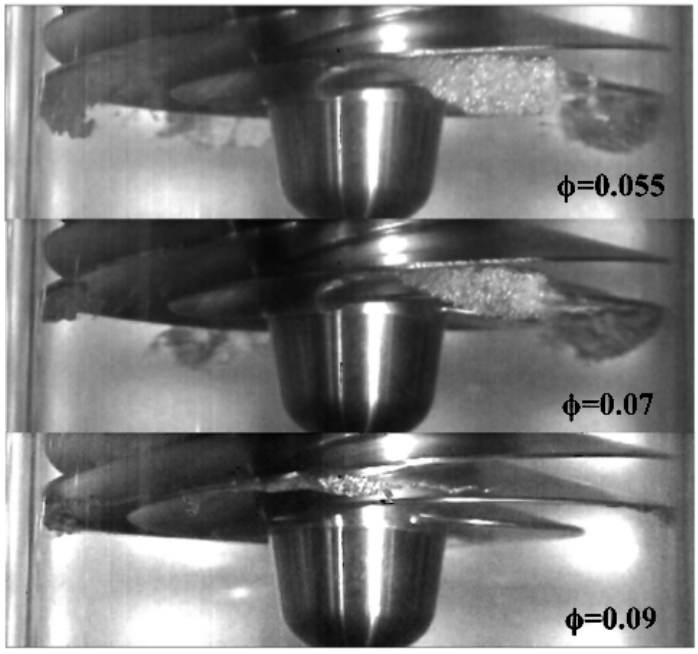


Figure 4-21: Side-view video data of tip vortex trajectories as indicated by their cavitation behavior at $\sigma = 0.1$ reflecting Figure 4-20 [12].

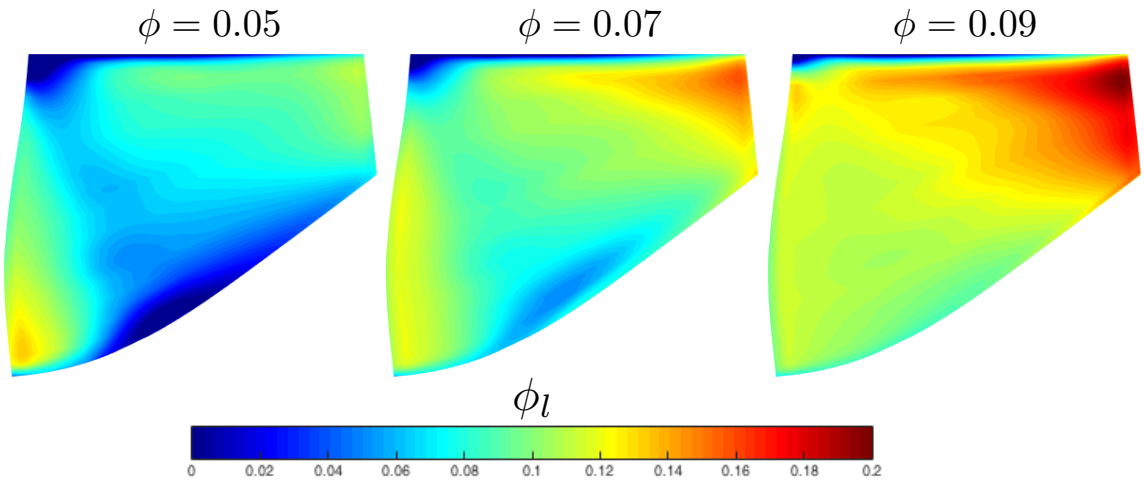
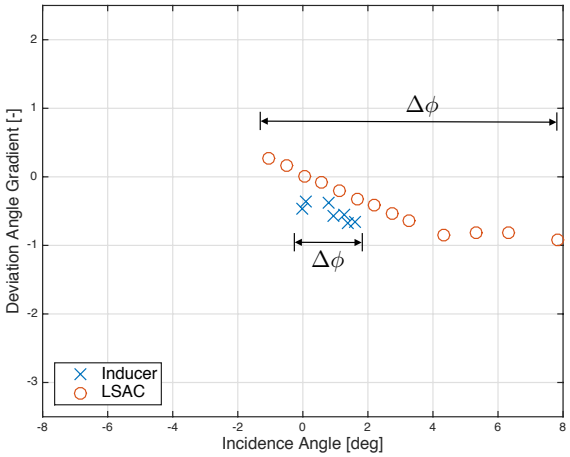
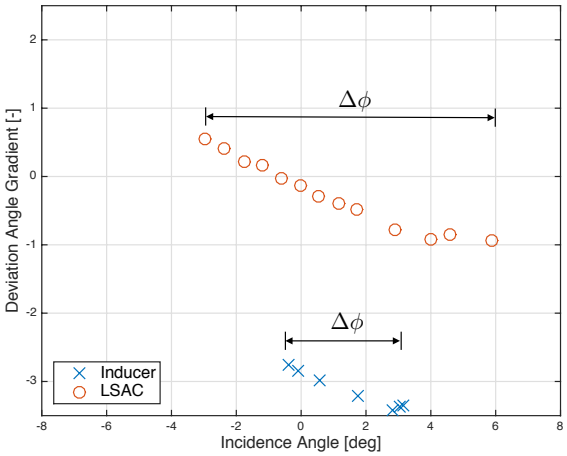


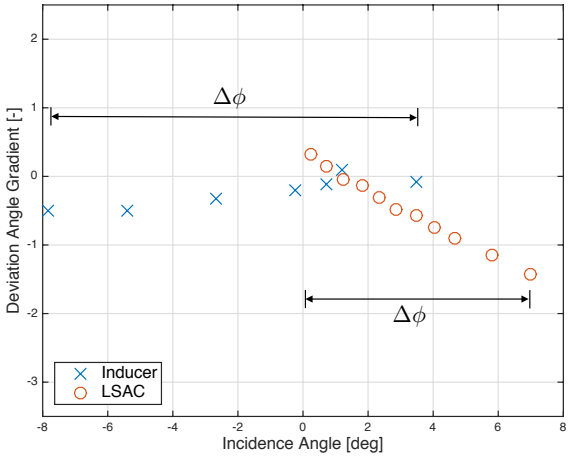
Figure 4-22: Pitchwise-averaged contours of axial velocity, nondimensionalized by tip speed, showing separation at the hub at lower flow coefficients.



(a) Midspan



(b) Hub

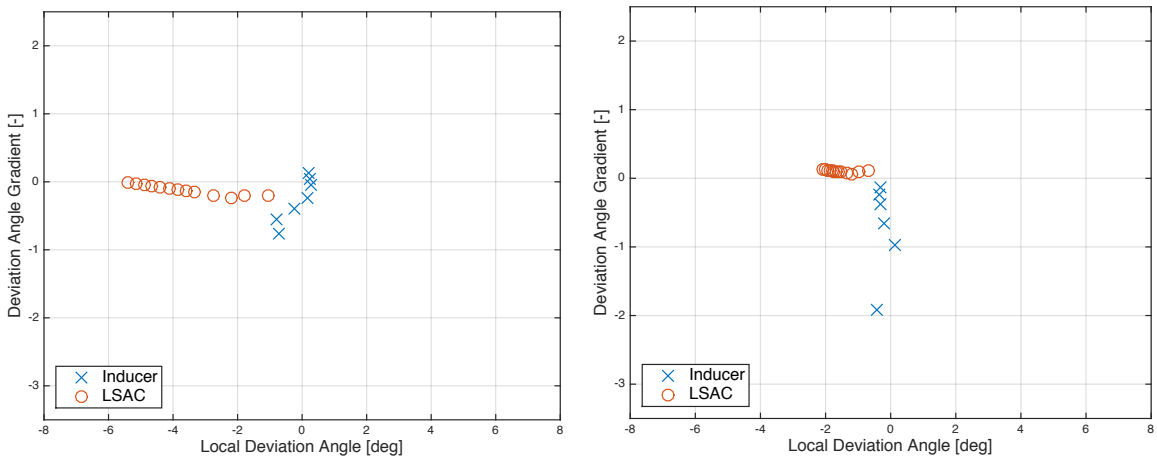


(c) Tip

Figure 4-23: Comparison of empirical term characteristics at different spanwise locations of the MIT inducer and LSAC.

within the blade passage, the inducer's deviation angle gradients are relatively large. Physically, this implies that small perturbations in deviation (i.e. flow angle) yield large changes in the force, leading to sensitivity in the model. Convergence issues therefore occur as the flow field changes iteration to iteration.

Analogous to Figure 4-17, the deviation angle gradient is plotted at the same spanwise locations in Figures 4-23; for each location plotted, the deviation angle gradient is extracted along the characteristic. The same representative trends are seen – for a comparable change in flow coefficient, there is a much narrower range of flow angle for the inducer than the LSAC at midspan and hub, while the ranges are similar at the tip.



(a) 37% chord, 25% span

(b) 50% chord, 25% span

Figure 4-24: Large deviation gradients due to separation in the blade passage, resulting in force sensitivity. At 37% chord, separation is present only for lower flow coefficients, while downstream at 50% chord, separation becomes more severe, as seen in Figure 4-25.

The trends continue in the blade passage, plotted in Figure 4-24, where deviation angle (defined by Equation 4.2) is analogous to incidence. As suggested in Section 3.4.2, small ranges of deviation are likewise prevalent throughout the inducer blade domain. Additionally, separation in the blade passage increases as flow coefficient is reduced, shown in a blade-to-blade view in Figure 4-25 and also noted in the pitchwise-averaged plots in Figure 4-22. The range of deviation angle gradient is much higher for the inducer, which is a consequence of the separation, as sketched in Figure 4-26 – with separation, the tendency of the flow to deviate from the local blade metal angle is higher. Figure 4-27a compares the ranges (i.e. difference between maximum and minimum across the characteristic at each grid point) of deviation angle gradients between the two geometries. The separation regions, as expected, are the locations of highest range.

In conjunction with the small ranges of flow angle, the large deviation angle gradients give rise to the force sensitivities – the empirical term dictates the force response to changes in the flow field. Notably, in the LSAC, the higher ranges of flow angles help the body force model negotiate the separation regions, where the deviation angle gradient ranges are higher relative to the rest of the blade domain. Figure 4-27b scales

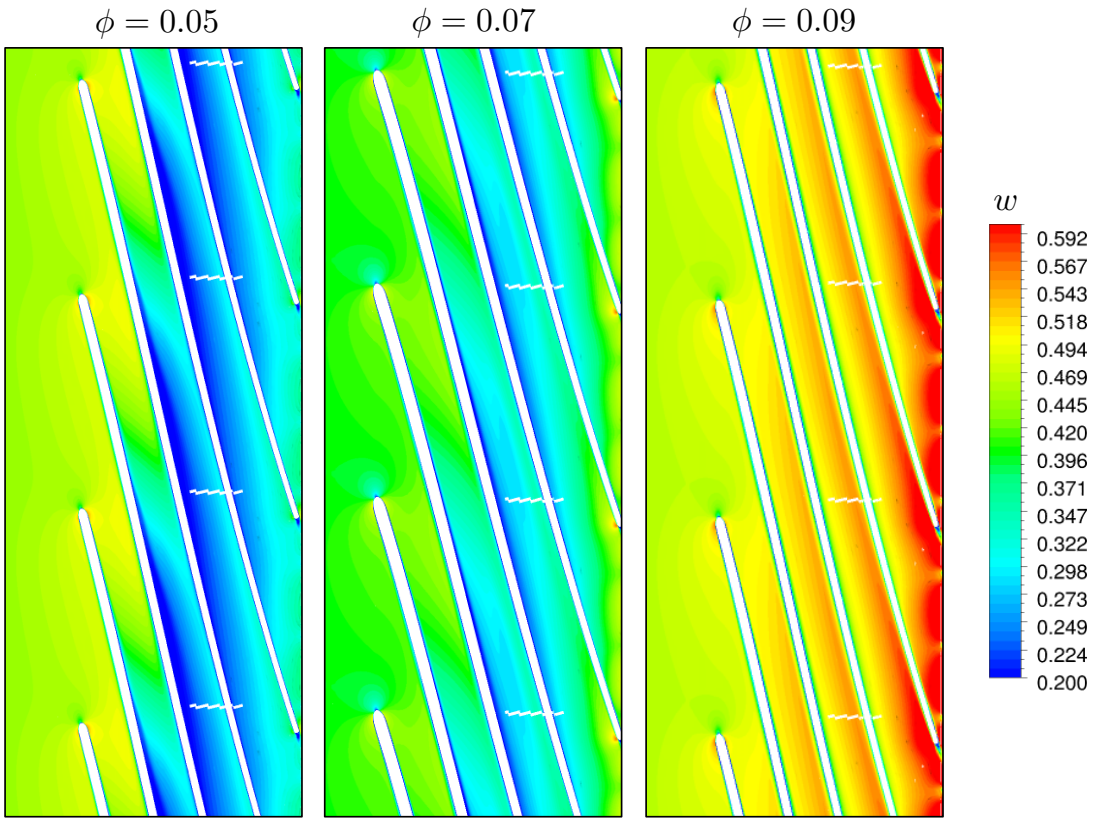


Figure 4-25: Blade-to-blade view of the MIT inducer at 25% span – contours of relative velocity magnitude are nondimensionalized by tip speed. Separation along the blade increases as flow coefficient is reduced. Horizontal white artifacts in each passage are due to the calculations being single-passage; the passage is repeated for the blade-to-blade view postprocessing.

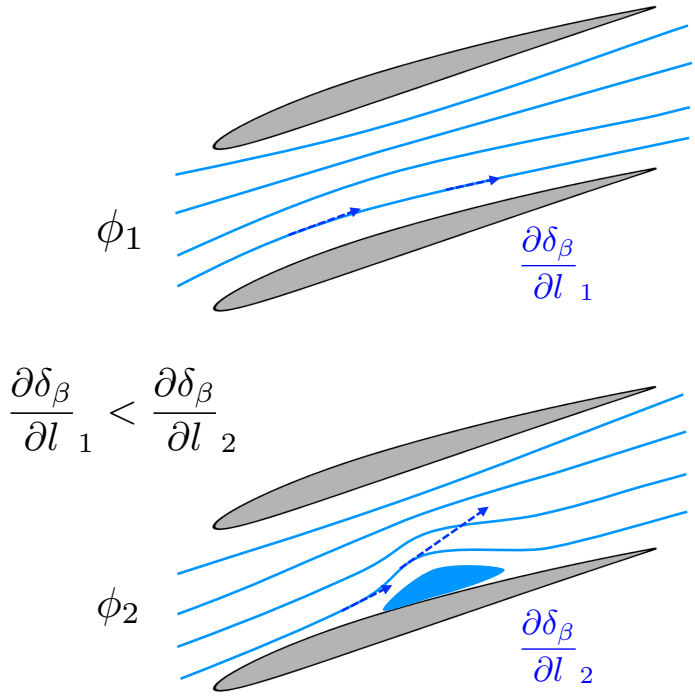
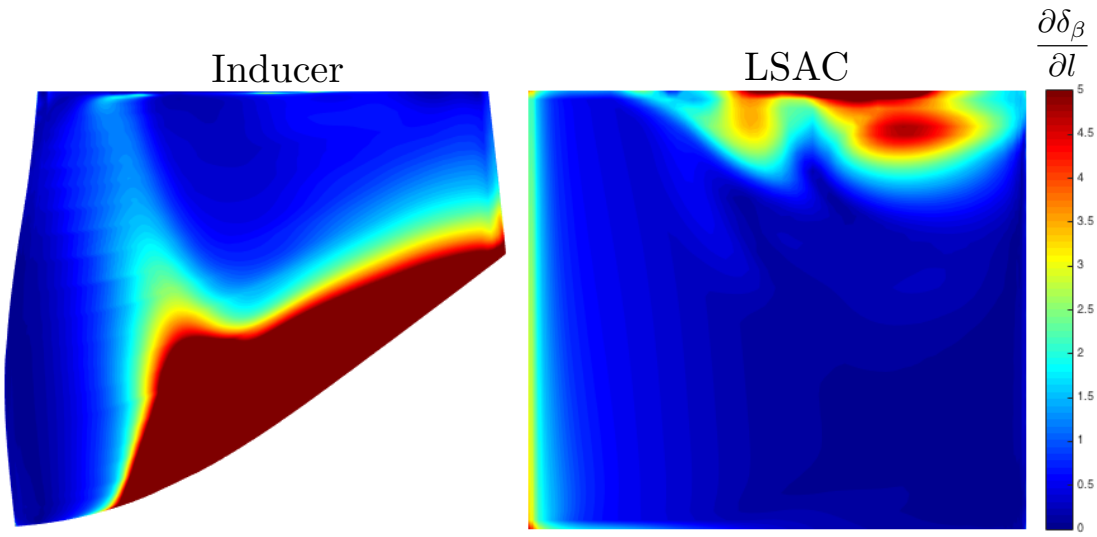


Figure 4-26: The deviation angle gradient captures tendency of the flow to deviate from local blade metal angle – the deviation angle gradients are higher in the presence of separation.

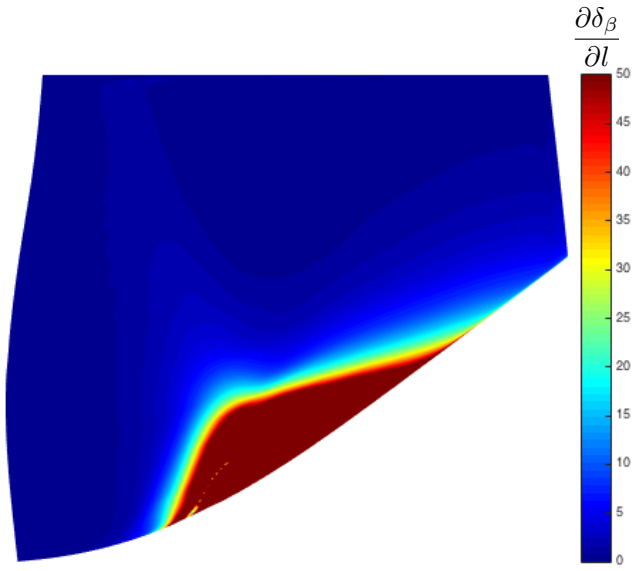
the contours for the inducer, indicating regions of empirical terms that are more than an order of magnitude higher than that found in the LSAC, which suggests an order of magnitude higher change in force for flow perturbations in the inducer. The combination of low flow angle range and the high force sensitivities results in a sensitive body force model in the case of the inducer geometry. The swings in calculated force as the flow field changes from iteration to iteration causes spurious recirculation, as seen in Figure 4-3 and, consequently convergence issues.

4.4 Major Findings

The investigations demonstrate that the blade passage model by Sorensen is able to successfully capture the performance characteristic of an axial compressor, even at near-stall conditions, indicating the model is valid and robust. The diagnostic results suggest that the convergence issues seen in the inducer case are therefore a



(a) Highest ranges seen in regions of separation (see Figures 4-22 and 4-25)



(b) Inducer ranges are over an order of magnitude higher than LSAC, suggesting an order of magnitude higher force response for the same flow perturbation

Figure 4-27: Ranges of deviation angle gradients across characteristic for each grid point.

consequence of the inducer geometry itself. The inducer's unique low flow coefficient design leads to nearly tangential flow in the blade domain and the associated high stagger angle geometry.

Compared with the axial compressor test case, the inducer loss buckets are narrow. The sensitivity of stagnation pressure loss to changes in incidence angle is due to the narrow range of incidences imposed throughout the characteristic by the inducer's highly tangential flow. The behavior of loss buckets is analogous to the empirical term characteristics in the body force model. Along with the highly tangential flow imposing small ranges of flow angle, the separation in the inducer throughout the operating range causes large changes in deviation angle gradient. The combined effect results in sensitivity in the empirical term, which dictates the force response. As the solver iterates, the flow angle perturbations cause large changes in the calculated body forces. This results in the inducer model's spurious recirculation regions, and ultimately, convergence issues.

The limitations of the applicability of body force modeling are therefore tied to the turbomachinery geometry itself. The inducer's low flow coefficient design and associated high stagger angles, combined with flow separation throughout most of the operating range, not typically seen in the previously studied aero-engine compressors and fans, gives rise to model sensitivity and convergence issues. A reduction of separation in the inducer could desensitize the body force empirical term and allow the calculation to converge. With the inducer design as-is, to desensitize the model, a force limiter could be implemented – the forces would be held to certain threshold values as the solver iterates to reduce the large swings in calculated force. Further investigation could involve a parametric study where rotor stagger angles are varied to define a limiting case geometry for which the current body force formulation is no longer valid.

Chapter 5

Conclusions

5.1 Summary

The overarching goal of this thesis was to characterize rotating cavitation instabilities in rocket engine turbopump inducers. Lettieri et al. [10–12] hypothesized the mechanism behind rotating cavitation onset is tip vortex interaction between adjacent blades leading to alternate blade cavitation breakdown. The present work aimed to assess this hypothesis through experimental analysis and a modeling approach.

An experimental campaign consisted of unsteady pressure measurements, side-view video, and frontal-view video of a test inducer. The data was analyzed using the Traveling Wave Energy methodology, yielding the temporal evolution of both the frequency content and mode shapes. Standard spectral analysis does not resolve spatial harmonic content, and given the spatial and temporal nature of TWE analysis, it is advantageous over the Hannover diagrams currently in use for determining cavity propagation direction. TWE was applied for the first time to unsteady pressure measurements of a cavitating inducer, leading to the identification of distinct cut-off/cut-on behavior for alternate blade cavitation and rotating cavitation, confirming the link between the two phenomena.

Additionally, the first-of-its-kind application of TWE to frontal-view video data allowed the extraction of cavitation instability signatures from optical measurements. The signatures qualitatively correlated with results from unsteady pressure data, indi-

cating TWE's viability as a new tool for experimental characterization of cavitation instabilities, and it was demonstrated that video TWE extracts more information than current quantitative methods for optical measurement analysis. The results suggest that rotating cavitation and alternate blade cavitation are dominated by circumferential wave patterns, indicating pressure measurements can be established as the primary detection method for unsteady cavitation behavior over high speed video, thereby significantly simplifying experimental setups.

The limitations of the applicability of the body force modeling approach were identified. A previously developed inducer-specific body force model exhibited spurious recirculation regions and convergence issues. Through a successful low speed axial compressor test case, the body force model formulation itself was found to be valid and robust, able to capture stalled conditions in the compressor. The results indicate that the inducer geometry itself is the root cause behind the model issues. The highly tangential flow in the inducer blade domain, a consequence of the inducer's low flow coefficient design and associated high stagger angles, is linked to the sensitivity of stagnation pressure loss to incidence angle. The loss sensitivity manifests in the model as sensitivity of the empirical term to local deviation angle, stemming from flow separation throughout the operating range of the inducer. Consequently, the model is sensitive to perturbations in the flow field, resulting in convergence issues as the solver iterates. The results suggest that the investigated body force model formulation is valid for aero-engine compressors and fans or inducers with little flow separation, while steps for desensitization of the model will need to be implemented for application to the MIT inducer.

In summary, the present work makes the following contributions:

- The successful demonstration of TWE for analysis of cavitation instabilities, addressing several limitations in the current experimental methods.
- An experimental confirmation of the link between alternate blade cavitation and rotating cavitation, as hypothesized by Lettieri et al. [10–12].
- A successful adaption of TWE to interrogate frequency content and spatial mode

shapes of frontal-view optical measurements of a cavitating inducer, yielding a new tool for the characterization of cavitation instabilities.

- Video TWE results suggest that radial variation of instability signatures is negligible, thereby indicating that pressure measurements can be established as the primary detection method for cavitation behavior over high speed video.

- The inducer-specific body force model formulation by Sorensen, corrected to capture aerodynamic blockage, is demonstrated to be valid and robust using a low speed axial compressor diagnostic test case.

- Diagnostic tests indicate the low flow coefficient design of the inducer, the associated high blade stagger angles, and flow separation throughout the characteristic as the limiting factors in body force modeling applicability. The results therefore suggest that the blade passage model by Sorensen is a viable body force modeling approach for conventional aero-engine turbomachines, such as fans and compressors, typified by their higher flow coefficient designs and lower stagger angle geometries, or inducers with little separation.

5.2 Recommendations for Future Work

The following recommendations are made for the continued experimental characterization of cavitation instabilities as well as the continued development of the inducer-specific body force model:

5.2.1 Experimental Characterization of Cavitation Instabilities

- For definitive correlation between the TWE results from inlet pressure data and optical measurements, simultaneous pressure measurements and video are necessary. Performance data should also be synced to the camera shutter such that the operating point of each video taken is known precisely.

- Lighting issues seen with the borescope videos can be alleviated by utilizing the light source capabilities in most borescopes, which direct an external light in the same direction as the borescope view. It is recommended that the inducer be painted a matte black to prevent reflection and glare from the borescope light. Additionally, more light would allow a zoom lens to be used with the borescope, allowing more resolution of cavitation behavior and therefore improved data quality.

- Filtering of the frontal-view video such that only cavitation is visible (e.g. removal of the leading edges, evening the lighting in each frame, etc.) could reduce noise and spurious signatures from the TWE results. Filtering would also allow the radial extent of cavitation region to be definitively determined (instead of doing a parametric study as in the present work).

5.2.2 Inducer-Specific Body Force Model

- The blockage correction for relative velocity magnitude in Sorensen's blade passage model is currently only calculated for design point; the implication is that body force calculations at different operating points will be slightly skewed. Calculating the correction at different operating points and implementing a scheme to match the corresponding correction with the operating point would improve the accuracy of the model.

- The sensitivity in the empirical term is linked to the flow separation prevalent throughout the MIT inducer characteristic. The application of Sorensen's blade passage model to an inducer design with less separation could result in a converged body force model.

- The observed convergence issues may be alleviated by implementing a force limiter. The forces would be held to certain threshold values as the solver iterates, reducing the large swings in force that lead to spurious recirculation regions

- While the presented results indicate the high stagger angles typically seen in low flow coefficient turbopump inducers are the root cause behind the body force model sensitivity and it was demonstrated that the model is valid for a representative compressor geometry, the limiting case for body force modeling has not yet been explored. A parametric study of a rotor with variable stagger angle would identify the limiting case geometry for which the body force model experiences convergence issues.

Bibliography

[1] K. Kamijo, H. Yamada, N. Sakazume, and S. Warashina. Development history of liquid oxygen turbopumps for the LE-7 engine. In *36th AIAA/ASME/SAE/ASEE Joint Propulsion Conference*, Huntsville, Alabama, 2000.

[2] R.S. Ryan. A history of aerospace problems, their solutions, their lessons. Technical Report 3653, NASA Marshall Spaceflight Center, 1996.

[3] B. Goirand, A. L. Mertz, F. Joussellin, and C. Rebattet. Experimental investigations of radial loads induced by partial cavitation with the LH2 Vulcain inducer. In *3rd International Conference on Cavitation*, Cambridge, England, 2000.

[4] T. Zoladz. Overview of rotating cavitation and cavitation surge in the Fastrac engine LOX turbopump. In *First International Symposium on Advanced Fluids Information*, Sendai, Japan, 2001.

[5] R. Sekita, A. Watanabe, K. Hirata, and T. Imoto. Lessons learned from H-2 failure and enhancement of H-2A project. *Acta Astronautica*, 2001.

[6] Y. Wu, S. Li, S. Liu, H. Dou, and Z. Qian. *Vibration of Hydraulic Machinery*. Springer, 2013.

[7] Y. Tsujimoto. Cavitation instabilities in inducers. *Design and Analysis of High Speed Pumps*, 2006.

[8] C. Brennen. *Hydrodynamics of Pumps*. Cambridge University Press, 2011.

[9] Y. Tsujimoto, K. Kamijo, and C. Brennen. Unified treatment of flow instabilities of turbomachines. *Journal of Propulsion and Power*, 2001.

[10] C. Lettieri and Z. Spakovszky. Origin of rotating cavitation in four bladed turbopump inducers. *Propulsion and Power Research*, 2016. Submitted.

[11] C. Lettieri, Z. Spakovszky, D. Jackson, and J. Schwille. Characterization of the dynamic behavior of a four bladed turbopump inducer. *Propulsion and Power Research*, 2016. Submitted.

[12] C. Lettieri, Z. Spakovszky, D. Jackson, and V. Wang. Characterization of rotating cavitation in a four bladed inducer. In *52nd AIAA/SAE/ASEE Joint Propulsion Conference*, Salt Lake City, Utah, 2016.

[13] N. Tani, N. Yamanishi, and Y. Tsujimoto. Influence of flow coefficient and flow structure on rotational cavitation in inducer. *Journal of Fluids Engineering*, 2012.

[14] Y. Tsujimoto, Y. Yoshida, Y. Maekawa, S. Watanabe, and T. Hashimoto. Observations of oscillating cavitation of an inducer. *Journal of Fluids Engineering*, 1997.

[15] H. Horiguchi, S. Watanabe, Y. Tsujimoto, and M. Aoki. A theoretical analysis of alternate blade cavitation in inducers. *Journal of Fluids Engineering*, 1999.

[16] S. Watanabe, K. Sato, and Y. Tsujimoto. Analysis of rotating cavitation in a finite pitch cascade using a closed cavity model and a singularity method. *Journal of Fluids Engineering*, 1999.

[17] Y. Tsujimoto. Simple rules for cavitation instabilities in turbomachinery. In *4th International Symposium on Cavitation*, Pasadena, California, 2001.

[18] E.M Greitzer. The stability of pumping systems – the 1980 Freeman Scholar lecture. *Journal of Fluids Engineering*, 1981.

[19] T. Kimura, Y. Yoshida, T. Hashimoto, and M. Shimagaki. Numerical simulation for vortex structure in a turbopump inducer: Close relationship with appearance of cavitation instabilities. *Journal of Fluids Engineering*, 2008.

[20] T. Hashimoto, M. Yoshida, M. Watanabe, K. Kamijo, and Y. Tsujimoto. Experimental study on rotating cavitation of rocket propellant pump inducers. *Journal of Propulsion and Power*, 1997.

[21] A. Cervone, C. Bramanti, L. Torre, D. Fotino, and L. d'Agostino. Setup of a high-speed optical system for the characterization of flow instabilities generated by cavitation. *Journal of Fluids Engineering*, 2007.

[22] A. Cervone, C. Bramanti, E. Rapposelli, L. Torre, and L. d'Agostino. Experimental characterization of cavitation instabilities in a two-bladed axial inducer. *Journal of Propulsion and Power*, 2006.

[23] L. d'Agostino. Turbomachinery developments and cavitation. In *VKI Lecture Series on Fluid Dynamics Associated to Launcher Developments*, Sint-Genesius-Rode, Belgium, 2013.

[24] A. Cervone, L. Torre, D. Fotino, L. d'Agostino, and C. Bramanti. Characterization of cavitation instabilities in axial inducers by means of high-speed movies. In *42nd AIAA/ASME/SAE/ASEE Joint Propulsion Conference*, Sacramento, California, 2006.

[25] C. Brennen and A.J. Acosta. The dynamic transfer function for a cavitating inducer. *Journal of Fluids Engineering*, 1976.

[26] Y. Tsujimoto, K. Kamijo, and Y. Yoshida. A theoretical analysis of rotating cavitation in inducers. *Journal of Fluids Engineering*, 1993.

[27] S. Watanabe, K. Yokota, Y. Tsujimoto, and K. Kamijo. Three-dimensional linear analysis of rotating cavitation in inducers using an annular cascade model. *Journal of Fluids Engineering*, 1999.

[28] S. Otsuka, Y. Tsujimoto, K. Kamijo, and O. Furuya. Frequency dependence of mass flow gain factor and cavitation compliance of cavitating inducers. *Journal of Fluids Engineering*, 1996.

[29] S. Rubin. An interpretation of transfer function data for a cavitating pump. In *40th AIAA/ASME/SAE/ASEE Joint Propulsion Conference*, Fort Lauderdale, Florida, 2004.

[30] A. Cervone, Y. Tsujimoto, and Y. Kawata. Evaluation of the dynamic transfer matrix of cavitating inducers by means of a simplified "lumped-parameter model". *Journal of Fluids Engineering*, 2009.

[31] C. Brennen. A review of the dynamics of cavitating pumps. *Journal of Fluids Engineering*, 2013.

[32] Y. Iga, M. Nohml, A. Goto, and T. Ikohagi. Numerical analysis of cavitation instabilities arising in the three-blade cascade. *Journal of Fluids Engineering*, 2004.

[33] A. Hosangadi, V. Ahuja, and R. Ungewitter. Simulation of cavitation instabilities in inducers. In *7th International Symposium on Cavitation*, Ann Arbor, Michigan, 2009.

[34] B. Benneke. A methodology for centrifugal compressor stability prediction. Master's thesis, Massachusetts Institute of Technology, 2009.

[35] J. Defoe. *Inlet Swirl Distortion Effects on the Generation and Propagation of Fan Rotor Shock Noise*. PhD thesis, Massachusetts Institute of Technology, 2011.

[36] A. Peters. *Ultra-short Nacelles for Low Fan Pressure Ratio Propulsors*. PhD thesis, Massachusetts Institute of Technology, 2014.

[37] W.A. Sorensen. A body force model for cavitating inducers in rocket engine turbopumps. Master's thesis, Massachusetts Institute of Technology, 2014.

[38] D.A. Ehrlich, J.A. Schwille, R.P. Welle, J.W. Mudock, and B.S. Hardy. A water test facility for liquid rocket engine turbopump cavitation testing. In *7th International Symposium on Cavitation*, Ann Arbor, Michigan, 2009.

[39] D. Jackson, J. A. Schwille, J. Davitian, C. Lettieri, V. Wang, and Z. Spakovszky. Cavitation instabilities in an inducer using heated water as a cryogenic stimulant. In *54th AIAA Aerospace Sciences Meeting, AIAA SciTech*, San Diego, California, 2016.

[40] D. Jackson, J. A. Schwille, J. Davitian, C. Lettieri, V. Wang, and Z. Spakovszky. Identifying cavitation instabilities in and inducer using heated water as a cryogenic simulant. In *16th International Symposium on Transport Phenomena and Dynamics of Rotating Machinery*, Honolulu, Hawaii, 2016.

[41] M. Tryfonidis, O. Etchevers, J.D. Paduano, A.H. Epstein, and G.J. Hendricks. Pre-stall behavior of several high-speed compressors. In *ASME 1994 International Gas Turbine and Aeroengine Congress and Exposition*, The Hauge, Netherlands, 1994.

[42] M.M. Bright, H.K. Qammar, H.J. Weigl, and J.D. Paduano. Stall precursor identification in high-speed compressor stages using chaotic time series analysis methods. *Journal of Turbomachinery*, 1997.

[43] Z.S. Spakovszky. *Application of Axial and Radial Compressor Dynamic System Modeling*. PhD thesis, Massachusetts Institute of Technology, 2001.

[44] E.R. Davies. *Computer & Machine Vision*. Academic Press, 2012.

[45] F. Marble. Three-dimensional flow in turbomachines. *High Speed Aerodynamics and Jet Propulsion*, 1964.

[46] M.L. Brand. An improved blade passage model for estimating off-design axial compressor performance. Master's thesis, Massachusetts Institute of Technology, 2011.

[47] Y. Gong. *A Computational Model for Rotating Stall and Inlet Distortions in Multistage Compressors*. PhD thesis, Massachusetts Institute of Technology, 1999.

[48] A.P. Kottapalli. Development of a body force model for centrifugal compressors. Master's thesis, Massachusetts Institute of Technology, 2011.

[49] G. Kiwada. Development of a body force description for compressor stability assessment. Master's thesis, Massachusetts Institute of Technology, 2008.

[50] E.M. Greitzer, C.S. Tan, and M.B. Graf. *Internal Flows: Concepts and Applications*. Cambridge University Press, 2007.